Title
High-Energy Graphene-Alloy Composites for Lithium and Sodium Storage

Author
Tan, Xinyi

Publication Date
2021

Peer reviewed|Thesis/dissertation

UNIVERSITY OF CALIFORNIA

Los Angeles

High-Energy Graphene-Alloy Composites for Lithium and Sodium Storage

A dissertation submitted in partial satisfaction of the

requirements for the degree of Doctor of Philosophy

in Chemical Engineering

by

Xinyi Tan

2021

ABSTRACT OF THE DISSERTATION

High-Energy Graphene-Alloy Composites for Lithium and Sodium Storage

by

Xinyi Tan

Doctor of Philosophy Candidate in Chemical Engineering

University of California, Los Angeles, 2021

Professor Yunfeng Lu, Chair

The massive combustion of fossil fuels and associated environmental problems have placed the significance of the utilization and development of renewable energy. Although renewable energy sources, such as wind, marine, solar, hydro, geothermal and biomass, can be continually replenished by nature, many of them are intermittent in nature, which request efficient energy storage systems for effective utilization. Among the various types of energy storage systems, electrochemical-energy-storage systems stands out due to their high efficiency, excellent adaptability in miscellaneous fields, low cost, and environmental benignity.

As the most extensively investigated energy-storage system, lithium-ion batteries (LIBs) have been commercialized for portable electronics and electrical vehicles, because of the high energy density, long lifespan, and low maintenance cost. The capacity of currently used anode material (graphite), however, has almost achieved its theoretical capacity; developing novel anode materials with higher capacity and a sufficiently low working potential has been emerging as essential and challenging topic.

Metal alloys with high gravimetric capacities and volumetric capacities are regarded as promising anode candidates in lithium-ion batteries. Unfortunately, alloyed materials usually suffer from severe volume expansion (up to 500%) and huge mechanical strain, which may lead to pulverization and drastic capacity decay. To address these issues, graphene has been used to form composites with the alloyed materials. Graphene is an allotrope of graphite with several intriguing properties, such as excellent electrical conductivity, remarkable thermal conductivity, large surface area, and robust mechanical strength. Since graphene can accommodate and buffer the volume change of alloyed materials during the cycling, and to improve the electrical conductivity and rate capability of electrodes, graphene-alloy composites have attracted much attention in recent years.

In this dissertation, we have developed three types of graphene-tin (Sn) composites with designed nanostructures. For the first one, we synthesized the composites of Sn and hierarchical flower-like graphene tubes (denoted as Sn/FGT), which afforded anodes with fast-charging capability. The Sn/DGT exhibits a high reversible capacity of 742 mA h g^{-1}, excellent rate capability (211 mA h g^{-1} at 8 A g^{-1} with 99% capacity retention when the applied current density was switched back from 8 A g^{-1} to 0.2 A g^{-1}) and a long cycle life. The nano-size Sn particles,

were uniformly anchored on hierarchical graphene tubes, which effectively prevented their aggregation. Such flower-like graphene tubes can serve as a highly conductive matrix, enabling efficient transfer of ions and electrons, and improving the rate performance.

Second, we have designed novel composites of Sn nanoparticles confined within graphene tubes that contain a nitrogen-doped graphene inner tube and a hydrophobic graphene outer tube (denoted as Sn/DGT). The nanosized Sn particles effectively alleviated the mechanical stress during the alloying/dealloying process, leading to improved electrical conductivity. The flexible inner void space of the graphene tubes buffered the volume expansion from the Sn nanoparticles, and provided high kinetics for the diffusion of electrons and ions. The composites delivered a high reversible capacity of 918 mA h g^{-1} for 500 cycles, and an extraordinary rate capability with a capacity of 916, 831, 761, 642, 548, and 481 mA h g^{-1} at the current densities of 0.2, 0.5, 1, 2, 5, and 10 A g^{-1}, respectively. Remarkably, Sn/DGT with a tap density around 2.76 g cm^{-3} showed a high volumetric capacity of 2532 mA h cm^{-3} and 1106 mA h cm^{-3} at a current density of 0.2 A g^{-1} and 20 A g^{-1}, respectively.

Second, we have designed novel composites of Sn nanoparticles confined within graphene tubes that contain a nitrogen-doped graphene inner tube and a hydrophobic graphene outer tube (denoted as Sn/DGT). The nanosized Sn particles effectively alleviated the mechanical stress during the alloying/dealloying process, leading to improved electrical conductivity. The flexible inner void space of the graphene tubes buffered the volume expansion from the Sn nanoparticles, and provided high kinetics for the diffusion of electrons and ions. The composites delivered a high reversible capacity of 918 mA h g^{-1} for 500 cycles, and an extraordinary rate capability with a capacity of 916, 831, 761, 642, 548, and 481 mA h g^{-1} at

the current densities of 0.2, 0.5, 1, 2, 5, and 10 A g^{-1}, respectively. Remarkably, Sn/DGT with a tap density around 2.76 g cm^{-3} showed a high volumetric capacity of 2532 mA h cm^{-3} and 1106 mA h cm^{-3} at a current density of 0.2 A g^{-1} and 20 A g^{-1}, respectively.

The work of this dissertation aims at providing possible solutions to tackle with current issues from alloy-based anodes in lithium and sodium storage, and broaden the nanostructure design of composite materials in energy storage. The high-performance anode materials are successfully developed through structural engineering of tin and tin alloy particles with graphene. The confined growth of tin or tin alloy particles within graphene scaffolds can fabricate highly conductive networks to retain the electrical contacts with active materials to enable prolonged cycling life, and facilitate the charge transport to improve the rate performance of the anodes. In addition, tin and tin alloy particles with high volumetric capacities can afford the anodes with high volumetric energy densities for lithium and sodium storage.

The dissertation of Xinyi Tan is approved.

Dante A. Simonetti

Philippe Sautet

Yu Huang

Yunfeng Lu, Committee Chair

University of California, Los Angeles

2021

TO MY FAMILY AND FUTURE OF MYSELF

Contents

LIST OF FIGURES

LIST OF TABLES

Acknowledgements

Time flies, this is my final year in UCLA. During my four-year doctoral journey, I have not only learned how to treat scientific research rigorously, but also enjoyed beautiful sceneries and blended into different kinds of customs. I met many people who might change my life in this campus, and words are powerless to express my gratitude to them.

Firstly, I would like to express my deepest appreciation to my advisor, Professor Yunfeng Lu. Without his patient guidance, continuous inspiration in research, and the encouragement and support in times of adversity, I would not be able to complete my studies so smoothly. As a professor with broad knowledge and endless passion in research, Dr. Lu has not only made remarkable contribution in energy storage, but also obtain breakthrough achievements in the biomedical field. In the past four years, Dr. Lu dedicated a lot to guide my research and provide tremendous supports to help me overcome the challenges I met. I always remembered that Dr. Lu told me the most crucial point in scientific research is to deeply understand the principles and think more about each step, and his persistence of in-depth thinking helped me complete my doctoral journey. I may not be his best students in his decades of teaching, but I will strive to be the one who never let him down.

I would like to thank my doctoral committee members, Professor Philippe Sautet Professor Dante Simonetti and Professor Yu Huang. It's your patient guidance and in-depth advices that helped me get to where I am today. I remembered that Professor. Sautet would write down every formula on the blackboard to explain the derivation process in his advanced thermodynamics course, and whenever I asked a question, he would answer it patiently with

his profound knowledge. I also remembered that Professor. Simonetti gave us many interesting questions that were related to actual industrial productions in the course of advanced chemical reaction engineering, and he told us that the criterion for judging an answer is not strictly right or wrong, but how to apply what you have learned to solve the practical problems. I really appreciated that Professor. Huang gave me a lot of insightful and enlightening suggestions in graphene-based materials for carbon dioxide electrocatalysis, although it was a pity that this research has not made significant progress due to the severe impact of the COVID epidemic.

To my dear Lu group members and friends, it is my honor to meet you all and spend this wonderful research time together. I would like to express my sincerest appreciation to Dr. Runwei Mo, who helped me with patience when I first joined Lu group. He taught me how to assemble a battery cell, and how to analysis basic electrochemical results for the batteries. Without his careful guidance and strong support, I could not adapt to the pace of research so quickly. I would also like to express my gratitude to Dr. Li Shen, who has spent countless days and nights to help me revise the imprecisions in my papers without any complaint. I would like to thank Dr. Ran Tao, Dr. Chen Zhang and Jinhui Xu for the assistance in SEM, TEM, Raman and BET testing for my experiments. I would like to express my appreciation to Dr. Xinru Li, who took me to Chinese supermarket to buy hometown food several times and stayed with me when I was sick, I am so lucky to have such a good friend. I would also like to thank Dr. Gurong Shen, Dr. Fang Liu, Dr. Fan Li, Dr. Wenyue Shi, Dr. Dejia Kong, Dr. Xianyang Li, Dr. Duo Xu, Dr. Xing Lu, Dr. Shengxiang Ma, Dr. Pengcheng Xu, Dr. Zhuang Liu, Dr. Zaiyuan Le, Dr. Di Wu, Dr. Jie Ren, Zheng Cao, Qingyang Yin, Xinheng Guo, Qi Tong, Qian Liu, Shilin Chen,

Alexis Fortini and Roxanne Castillo. Thank you all for the good time in my four-year research life in UCLA.

Finally, I would like to express my special appreciations to my parents. Without their love and strong support, I cannot enjoy my research life in UCLA. My father is an academician of the Chinese Academy of Engineering, and he taught me a lot with his knock-on spark of inspiration and rigorous attitude towards the scientific research. Whenever I encounter bottlenecks in my research, he is always happy to share his experiences of overcoming the difficulties and provide me possible solutions for my research. I also want to express my deep gratitude to my mother, who would chat with me every day no matter how busy she is. Whenever I feel lonely in a foreign country, my mother will give me spiritual encouragement and emotional support to make me happy. I miss them every day in my four-year doctoral journey, and this dissertation is dedicated to my family and the future of myself.

Chapter 1 Introduction and background

1.1 Energy and environment

Energy is like the blood of a country that drives daily operations for humans. Although energy comes from various sources, it can be categorized as two major forms: primary and secondary forms of energy.[1-2] The crude oil, hard coal, natural gas, nuclear and wind energy that we are familiar with are classified as primary forms of energy since they only experienced extraction or capture before the utilization. For those energy such as petroleum, electricity and biofuels which are the results of transformation and conversion from the primary energy are all classified as the secondary forms of energy. The primary and secondary forms of energy both have numerous applications in human's society. As for the primary energy, fossil fuels take up the highest proportion of energy consumption in modern society. The utilization of fossil fuels is mainly carried out through the combustion; however, the massive combustion of fossil fuels will lead to a series of environmental problems. The combustion products of fossil fuels contain a large amount of CO_2 which has been identified as the main cause of global warming. The melting of polar ice sheet, rise of sea level and a sharp decline of biodiversity that caused by global warming will have a huge impact on human life. Furthermore, the sulfur and nitrate contained in fossil fuels will form SO_x and NO_x after the combustion, these oxides will form acid rain when they contact with water vapor in the sky. In addition, the formation of fossil fuels needs a very long time and the reserve of fossil fuels on earth is limited, so it is crucial to develop renewable and clean energy to release the dependence of fossil fuels in the future.

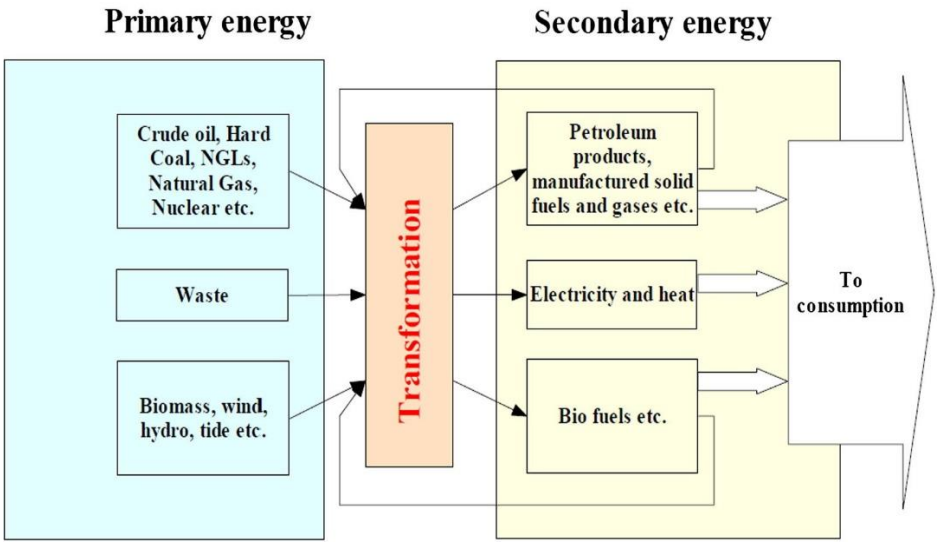

Figure 1.1 Primary and secondary energy.[2]

1.2 Renewable energy

Due to severe environmental issues and rapid depletion of primary energy with limited reserves, the utilization of clean and renewable energy has become the new regime. Renewable energy is collected from energy sources that are continually replenished by nature and derived directly from the sun (such as thermal, photo-chemical, and photo-electric), indirectly from the sun (such as wind, hydropower, and photosynthetic energy stored in biomass), or from other natural movements and mechanisms of the environment (such as geothermal and tidal energy).[3-4]

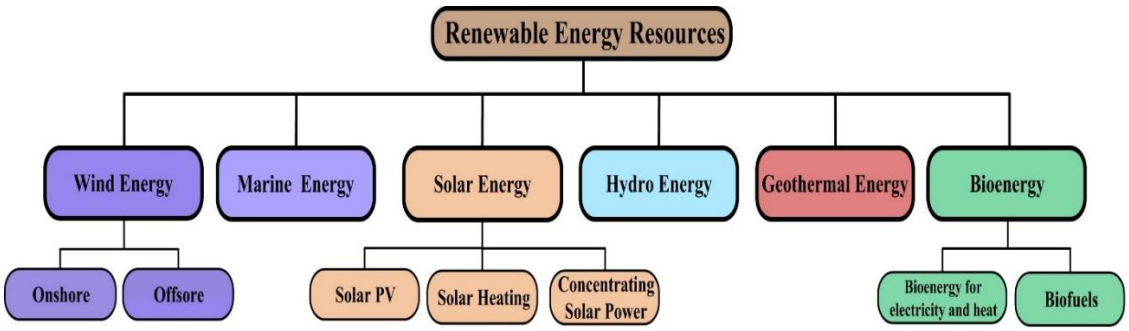

Figure 1.2 Overview of renewable energy sources[3]

Figure 1.2 shows an overview of renewable energy. Wind energy is defined as the conversion from wind turbines into assorted power forms; marine energy is mainly obtained from waves or tides that can convert the ocean energy into other forms; solar energy involves the utilization of sun energy through photovoltaic methods; hydro energy is derived from the energy of moving water; geothermal energy extracts thermal energy from the interior of earth which is stored in both rock and trapped steam or liquid water; biomass energy is the collection and storage of solar energy in plants or trees through photosynthesis pathways.[3] However, renewable energy is usually unstable in nature which means that it needs more efficient methods to use and reserve.

1.3 Energy storage systems

Energy storage systems can accommodate the fluctuations and intermittent nature of renewable energy and give the opportunity to mitigate the imbalance between the energy supply and demand.[5] A variety of energy storage systems have been developed to meet the needs of storage and utilization of renewable energy. Mechanical, thermal, chemical and electrochemical are four typical energy storage systems.[6-8]

1.3.1 Mechanical energy storage system

Mechanical energy usually converts potential or kinetic energy into other forms of energy such as electricity. Flywheel storage, pumped hydro storage and compressed air storage are three major types of mechanical energy storage systems.

1.3.1.1 Flywheel energy storage system

The flywheel energy storage (FES) system can generally transform the stored rotational kinetic energy into the electrical energy. FES system usually consists of a cylinder-shaped motor generator, a flywheel that can store the kinetic energy, a frequency inverter and several magnetic bearings. The working principle of FES system is that when flywheel is rotating with the driving force from the motor generator, the electrical energy will be stored as kinetic energy; when the flywheel slows down, the kinetic energy will be released as electrical energy.[5] The energy density of FES system is largely determined by the material that used for flywheel since the energy density is linearly related to the mass and the square of the angular velocity of the flywheel.[9] Therefore, a flywheel with higher Young's modulus and higher rotating speed will lead to a higher energy density of FES system. The FES system shows several advantages such as high power density, high energy storage efficiency, long working life, wide temperature working ranges and slight environmental concerns.[10]

1.3.1.2 Pumped hydro energy storage system

Pumped hydro storage (PHS) system stores the potential energy of water that is pumped from a lower level to a higher level. PHS system usually consists of an electrical generator that can raise the water from lower level to upper level, and then convert the potential energy that stored in water into the electrical energy by releasing water through turbines. PHS system can provide bulk electricity due to its large energy storage capacity. However, the practical

application of PHS system has been hindered by high cost and severe dependence on topography.

1.3.1.3 Compressed air energy storage system

Compressed air energy storage (CAES) system utilizes electricity to compress air that is stored in a large underground container, and electrical energy will be regenerated by recovering the compressed air from the storage.[11] CAS system consists of compressors, generator-motor, recuperator, coolers and turbines. Firstly, the compressed air is stored at a high pressure, and then the compressed air will be released and heated through turbines that are connected to an electrical generator to produce electricity. Although CAES system has the advantage of large energy storage capacity, it is not suitable for the application of portable devices due to its large volume and complicated technologies of underground storage.[12-13]

1.3.2 Thermal energy storage system

Thermal energy is widely existed in nature, and thermal energy can be stored as latent heat by warming up or melting the energy storage materials.[9] The heat sources of thermal energy can be categorized from solar thermal energy, geothermal energy, fossil-fuels power plants, nuclear power plants, industrial waste heat and biomass.[14-18]

1.3.2.1 Solar thermal energy storage system

Solar thermal energy storage system can convert solar irradiation into the thermal energy to heat the working devices. The solar irradiation can be absorbed by several parabolic solar collectors to transfer into the heat, then the working fluid inside the tank can store the heat to provide thermal energy for the boiler. Solar thermal energy storage system has the advantages of long working life, lower cost, limited toxicity in solar collector materials and high round-trip energy efficiency (50%-100%).[15, 19]

1.3.2.2 Geothermal energy storage system

Geothermal energy exists in the Earth's interior with the form of heat energy. Geothermal energy that stored in earth's mantle can be utilized in various fields. Geothermal fluid that has temperature higher than 150 °C is suitable for electricity generation, and geothermal fluid that has temperature lower than 100 °C can be directly used as drying of agricultural produce.[15, 20] Compared to other renewable energy sources such as solar and wind, the continuity of geothermal energy makes it suitable for base load power generation.[21]

1.3.3 Chemical energy storage system

Chemical energy storage (CES) system can convert the stored chemical energy into the electrical energy. Chemical energy that is stored in the chemical bonds of atoms and molecules can be released in a chemical reaction.[22] The most common used chemical fuels in CES system are hydrogen, natural gas, butane, ethanol and biodiesel. Hydrogen storage and synthetic natural gas storage are two major methods of CES system.

Hydrogen is a promising alternative energy since it is a carbon-free energy carrier and it exhibits the highest energy density compared to the other chemical fuels. Hydrogen energy storage system can be categorized as physical storage and materials-based storage. Gas-phase storage and liquid-phase storage are two major methods in physical storage of hydrogen energy. In gas-phase storage, hydrogen is usually stored in high-pressure gas cylinders with a maximum pressure of 80 MPa, while liquid hydrogen is stored in cryogenic tanks at 21.2 K and ambient pressure in liquid-phase storage.[23] Materials-based storage method utilizes the principle that hydrogen reacts with many transition metals and their alloys to form hydrides at elevated temperatures.[24-25] Alanates, borohydrides and amides are three typical groups of materials that have been widely used in hydrogen storage system.[26-27] As shown in Figure 1.3, hydrogen storage system is composed by a hydrogen generator such as water electrolyzer, a hydrogen storage container and energy conversion components. Hydrogen energy storage system has the advantages of cleanliness, abundance, affordability and high efficiency;[28-29] however, the production and distribution technologies of hydrogen energy still need further research.[30-31]

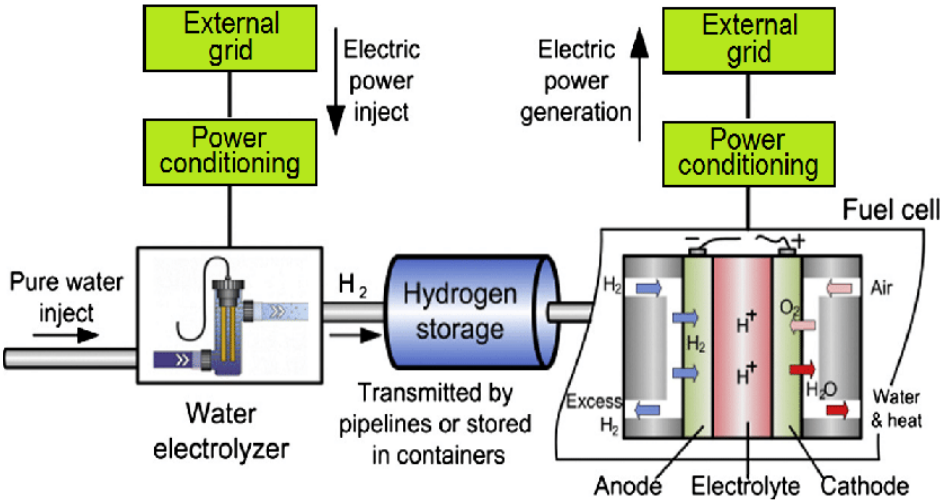

Figure 1.3 Topology of hydrogen storage system.[32]

Synthetic natural gas mainly consists of methane. The storage of synthetic natural gas is usually in pressure tanks or underground.[33-34] Similar to hydrogen energy storage, the synthetic natural gas storage system can provide clean and high-power energy with minimum effects on environment.

1.3.4 Electrochemical energy storage system

Current utilization of renewable energy relies on the conversion from those natural resources into electricity, heat or other forms of energy through variable technologies. Among several types of storage technologies, electrochemical energy storage system is one of the most desirable methods due to its high energy density, long cycle life, low cost and flexible power which can meet the needs of different functions.[35]

Electrochemical energy storage system (EES) is widely used in the fields of portable devices, transport vehicles and stationary energy storage.[36] The principle of EES is the reciprocity between converting chemical energy that stored in the reactants into the electrical energy, and transforming electrical energy to synthesize reactants in a reverse direction.[37] The driving force of this conversion in electrochemical energy storage system is the change of Gibbs free energy in the chemical reaction between electrodes. The electrostatic energy of charged reactants can be defined as zEF, where z is the charge number of transporting species, F is Faraday's constant and E is the cell voltage of the system. As for open circuit system, the

relation between cell voltage and the change of Gibbs free energy can be described as $\Delta G = -zEF$.

The electrochemical energy storage system is usually consisted of anode, cathode, separator and electrolyte. During the discharging process, electrochemical reactions will occur at the electrodes and generate electrons that flow through an external circuit; during the charging process, an external voltage will drive the movements of electrons and reactions in a reverse direction.[7]

A wide range of devices such as batteries, fuel cells and supercapacitors have been applied with the fundamental of electrochemical storage system. Batteries can store charge within electrodes, fuel cells store charge in the fuels, and supercapacitors can store charge either in the electric double layer at the electrode/electrolyte interface or as pseudo-capacitance governed by surface redox reactions.[37]

1.3.4.1 Batteries

According to different types of electrode materials, rechargeable batteries can be classified as lead-acid, nickel-cadmium (Ni-Cd), nickel-metal hydride (Ni-MH), sodium-sulfur (Na-S), zinc-air (Zn-air), lithium-sulfur (Li-S), lithium-ion and sodium-ion batteries. Various types of rechargeable batteries are shown in Figure 1.4.

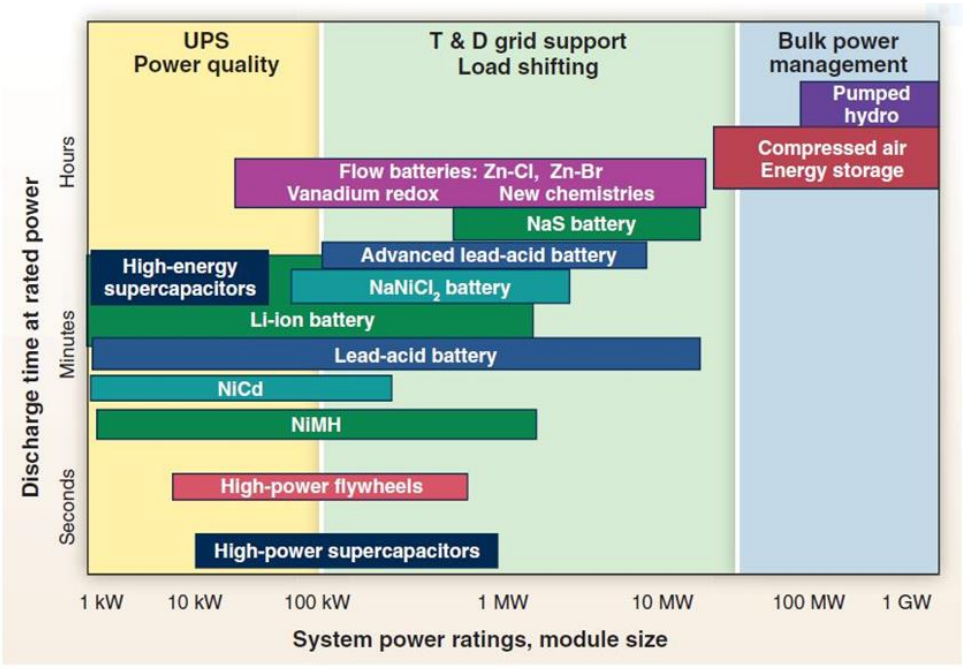

Figure 1.4 Comparison of discharge time and power ratings for various batteries.[35]

The oldest type of rechargeable batteries is the lead-acid battery that was invented by French physicist Gaston Plante in 1859. The lead-acid battery has the advantages of low cost, stable operating voltage (>2 V), moderate operating temperature (-40 °C~60 °C), good recharge efficiency (>70%) and availability in various designs.[38-40] Although lead-acid battery has been widely used in electrical vehicles and stationary power systems, it still suffers from low energy density (30-40 W h kg^{-1}), relatively low cycle life (approximately 500 deep cycles) , large volume occupation and irreversible damage under long discharging process.[41-42]

Nickel-cadmium (Ni-Cd) batteries have been applied in electronic devices for decades. The Ni-Cd battery is usually composed of a hydroxy-oxide cathode, a metallic cadmium anode and potassium hydroxide electrolyte.[43] In spite of low cost and high energy capacity, the market of Ni-Cd battery has been shrunk by the toxicity and scarcity of cadmium. In order to avoid

hazardous contamination of soil and water from cadmium, the recycling of Ni-Cd batteries is necessary.[44-45] Besides, the severe memory effect of Ni-Cd battery can lead to a sharp drop of the capacity and end the cycle life of Ni-Cd battery in a short time.[46]

Nickel-metal hydride (Ni-MH) battery was introduced to the commercial market in 1991. The electrochemical reaction occurs at the cathode of Ni-MH battery is similar to that of Ni-Cd battery, but Ni-MH battery uses hydrogen-absorbing alloy as the anode material instead. Hydrogen diffusion in anode side can dominate the high-rate discharge capability of Ni-MH batteries.[47] Compared to Ni-Cd battery, Ni-MH battery has the features of high energy density (up to 2000 W kg^{-1}), flexible cell sizes (30 mAh~250 Ah), safe operation voltage, low cost and good environmentally compatibility with non-toxic electrode materials.[48-50] However, Ni-MH battery will produce a huge amount of heat while charging at a high power, and thus lead a short lifespan of the battery.[48]

Sodium-sulfur (Na-S) battery is firstly invented by Ford Company in 1967 and it is composed of sodium metal anode, sulfur cathode, beta-Al_2O_3 ceramics electrolyte and the separator. The working principle of Na-S battery is based on the electrochemical reactions between sodium metal and sulfur and the formation of sodium polysulfide. When discharging, the sodium metal will be oxidized to sodium ions to transport across the membrane and reacts with reduced sulfur anions to form sodium polysulfide. The reverse reactions will happen when charging, and sodium polysulfide will decompose to sodium and sulfur. The operating temperature of Na-S battery usually ranges from 300 °C to 350 °C to guarantee sodium and sulfur as well as the reaction product sodium polysulfide can exist in a liquid state to afford high reactivity of the electrodes.[51] Although Na-S battery has the advantages of high energy

density (760 W h kg^{-1} at 350 °C),[52] temperature stability and low cost, the safety issue of flammable electrode materials still leaves a risk in transport.[53-54]

Zinc-air (Zn-air) battery was commercialized and applied in hearing aids in 1970s.[55] The Zn-air battery is usually composed by a zinc anode, an air cathode, a membrane separator and alkaline electrolyte. Zn-air battery generates electricity from the redox reactions between zinc anode and oxygen in the air from a porous cathode.[56] Zn-air battery has been regarded as a promising candidate for electrochemical energy storage due to its high theoretical energy density (1084 W h kg^{-1}),[57] low cost, safety and environmental friendliness.[58-59] Unfortunately, the practical application of Zn-air battery has been limited by the short cycle life. The short lifespan of Zn-air battery is mainly attributed to the growth of zinc dendrites during the cycling, morphology change of zinc anode and failure of air cathode.[60-61]

Lithium-sulfur (Li-S) battery is consisted by a metallic lithium anode, a sulfur cathode, a membrane separator and organic electrolyte such as dimethyl ether. The fundamental of Li-S battery relies on the reversible conversion between sulfur and lithium sulfides.[62] Li-S battery possess extremely high specific capacity (1675 mA h g^{-1}) and high energy density (2600 W h kg^{-1});[63-65] however, the commercialization of Li-S battery has been hindered by short lifespan, low charging efficiency, poor safety and a high self-discharge rate.[66-69] The challenges for Li-S battery are caused by parasitic reactions between the lithium polysulfide and lithium anode and electrolyte components.[66]

Lithium-ion battery (LIB) has become the predominant energy source of portable electrical devices and electric vehicles. The fundamental of lithium-ion battery is based on the reverse

reactions between a lithium anode and a lithium intercalation cathode. Compared to the other energy storage systems, lithium-ion battery exhibits miscellaneous advantages such as high energy and power density, long cycle life, low maintenance cost and no memory effects.[70-72] Although lithium-ion battery has been commercialized on a large scale, the battery capacity and electrode performance still deserve the further improvements.

Sodium-ion battery (SIB) is a new energy storage system that emerged in recent years. The large-scale applications of lithium-ion battery have caused excess consumption of lithium reserve on earth and result in an increase of the cost. Therefore, sodium-ion battery is considered to be an alternative battery system due to abundant sodium sources and similar intercalation mechanisms during electrochemical reactions.[73-74] In addition, the copper current collector in lithium-ion battery can be replaced by cheaper aluminum in sodium-ion battery since sodium does not alloy with aluminum.[75] However, the commercialization of sodium-ion battery has been impeded by unstable low energy density and poor cycling stability.[76] Hence, the amelioration of electrode materials in sodium-ion battery is urgently needed.

1.3.4.2 Fuel cells

Fuel cell is an electrochemical system that can convert chemical energy from fuels and oxidizing agents into electricity through a pair of redox reactions.[77] Hydrogen is usually identified as the fuel due to its carbon-free energy carrier property, and oxygen is often used as the oxidizing agent in the fuel cell system.[78-79] The first fuel cells were invented by Sir William Grove in 1838, and fuel cells have been commercialized in various fields such as power

vehicles and backup power for buildings. As shown in Figure 1.5, a fuel cell is usually consisted of an anode, a cathode and electrolyte that allows the movement of ions and protons between two electrodes. The fuels undergo the oxidation reactions to generate ions and electrons on the anode side, and then those ions move from the anode to the cathode through the electrolyte; the oxygen on the cathode side will react with the ions and electrons to form water and other products.[80] Compared to batteries that can only convert stored chemical energy into electricity, fuel cells can continuously output energy as long as the supplies of hydrogen and oxygen keep flow into the system. In addition, fuel cells are smaller and lighter than batteries and are easier to refuel or implement to a larger scale system.[81]

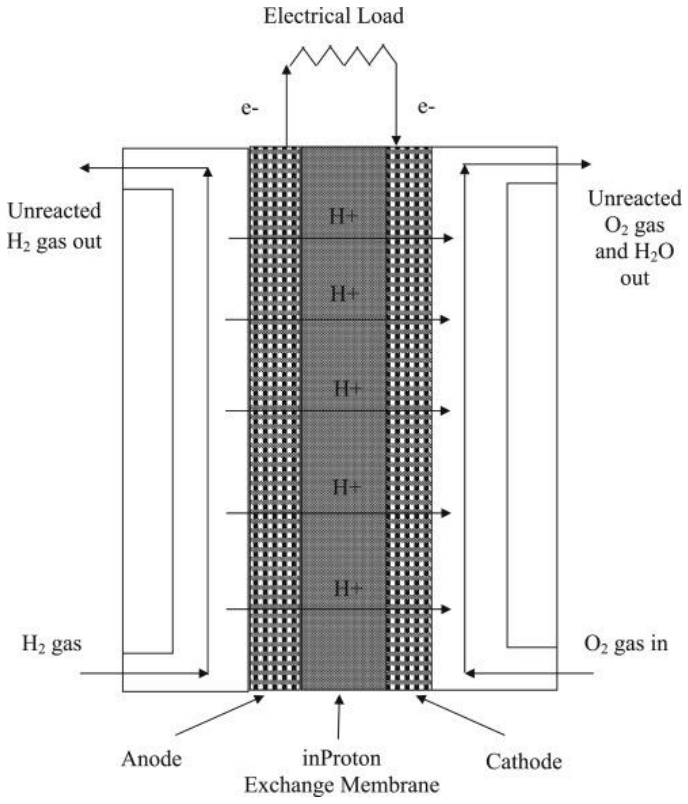

Figure 1.5 Schematic diagram of fuel cells.[81]

1.3.4.3 Supercapacitors

Supercapacitor acts as a bridge to gap the energy power difference between traditional electrolytic capacitors and rechargeable batteries.[82] Electrochemical double-layer capacitors (EDLCs), pseudo capacitors and hybrid capacitors are three major types of supercapacitors.

EDLCs use carbon-based electrodes to store charge through the formation of electrochemical double layers (non-Faradic process); pseudo capacitors use metal oxides or conducting polymers as the electrodes to store charge through the redox reactions (Faradic process); hybrid capacitors use the combination of electrodes from EDLCs and pseudo capacitors to store charge in both Faradic-process and non-Faradic process.[83] The schematic diagrams of EDLCs and pseudo capacitors are shown in Figure 1.6 and Figure 1.7, respectively.

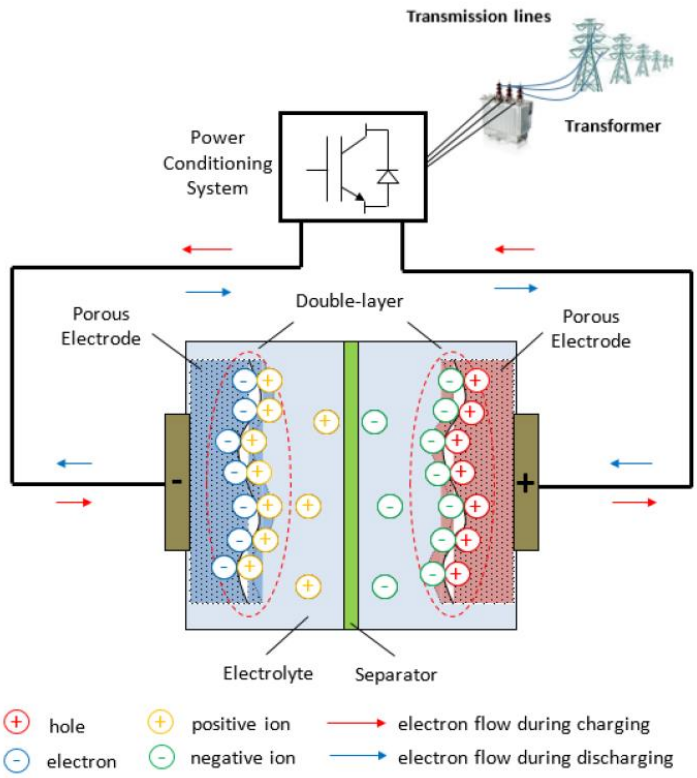

Figure 1.6 Schematic diagram of double-layer electrochemical double-layer capacitor.[84]

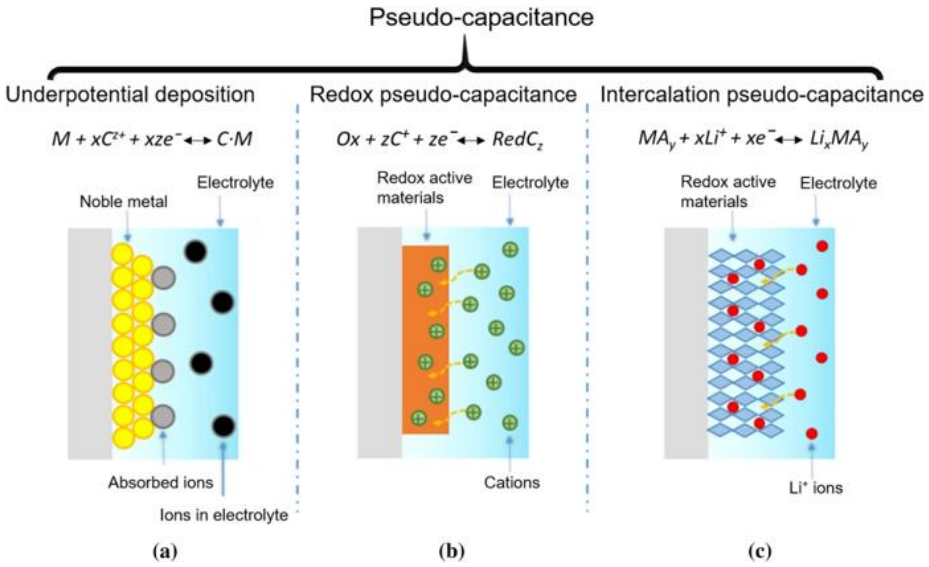

Figure 1.7 Schematic diagram of pseudo capacitor.[85]

Supercapacitors have gained much attention owing to their high specific capacitance, high power density, long cycle life, low maintenance cost, no memory effect and safety in utilization.[86-87]

1.4 Lithium-ion batteries

Lithium-ion battery has become the primary choice of power source in portable devices, electric vehicles and grid storage due to its high energy density, high working potential, low maintenance cost, low self-discharge and long lifespan.[88-90]

1.4.1 Fundamental of lithium-ion batteries

Lithium-ion batteries are composed by four major parts: cathode, anode, electrolyte and a membrane which separates anode and cathode. Conventionally, the process of lithium ions

entering the cathode is called "embedding", and the process of lithium ions leaving the cathode is called "deintercalation"; the process of lithium ions entering the anode is called "insertion", and the process of lithium ions leaving the anode is called "deintercalation". Lithium ions can move freely to be intercalated and deintercalated in both electrodes.

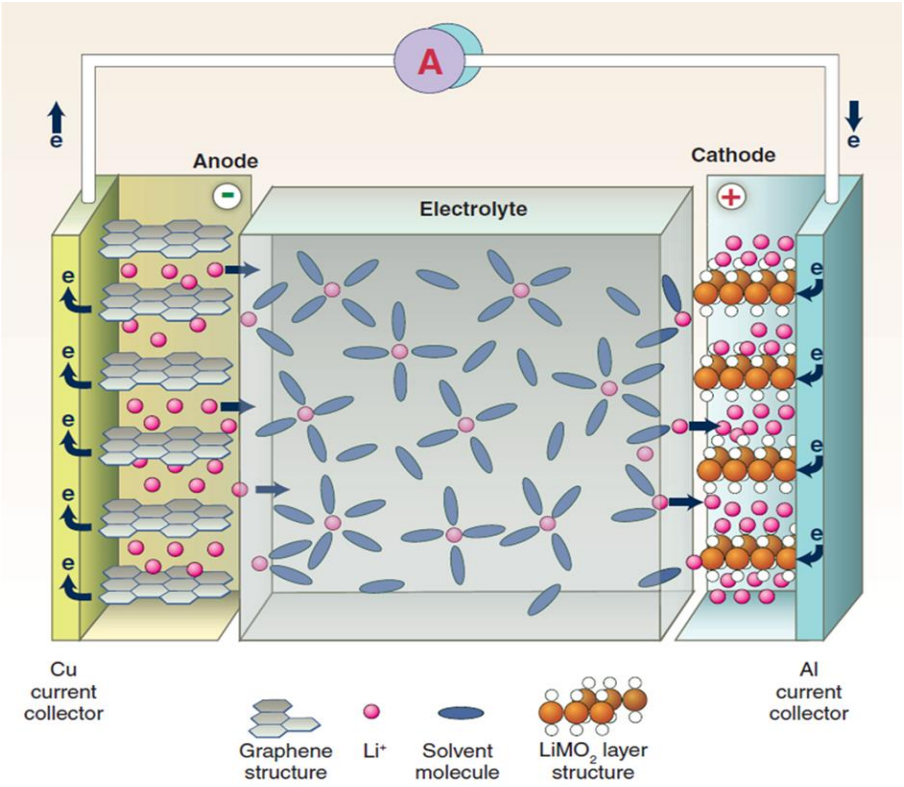

Figure 1.8 Schematic diagram of lithium-ion batteries.[35]

The basic components of lithium-ion battery are shown in Figure 1.8. When charging, lithium ions are removed or deintercalated from cathode side ($LiMO_2$ layer) and intercalated into the anode (graphite layer). The process will be reversed when the battery is discharging. The reactions that happened on the electrodes are below:

$$Anode: Li_xC_6 \leftrightarrow xLi^+ + xe^- + 6C$$

$$Cathode: Li_{1-x}MO_2 + xLi^+ + xe^- \leftrightarrow LiMO_2$$

Although lithium-ion batteries have been widely applied in portable devices and electrical vehicles, the growing needs for high energy density, high capacity, long lifespan and safe energy storage system still seek the innovation and improvement of electrode materials for lithium-ion batteries.

1.4.2 Anode materials of lithium-ion batteries

The performance of lithium-ion battery is largely determined by the theoretical specific capacity, electric conductivity, mechanical robustness, structure design and particle size of the electrode materials. Carbonaceous materials, lithium titanate, alloy-based materials and transition metal oxides are four major types of anode materials that are commonly used in lithium-ion batteries.

1.4.2.1 Carbonaceous materials

Carbonaceous materials have become the mainstay of anodes in lithium-ion batteries during the past decades. Compared to the other candidates such as metal oxides, chalcogenides and polymers, carbonaceous materials possess the features of higher specific charges, lower redox potentials and better cycling stability.[91] Graphite, hard carbon, carbon nanotubes, graphene are four typical carbonaceous materials that are utilized in lithium-ion batteries.

1.4.2.1.1 Graphite

Graphite is composed by layers of linked hexagons of carbon atoms, and the layers are stacked in a ABAB sequence so that half of the atoms in a layer are directly above and below carbon atoms in the adjoining layers, while half are directly above and below the center of the hexagons.[92] Benefit from this unique structure, graphite has a good thermal conductivity within the layers. In addition, graphite can conduct electricity since the valence electrons in carbon layers are free to move. The electrical and thermal conductivity of graphite facilitate its widespread utilization as electrode materials in energy storage.[93] In 1986, Rajeeva R. Agarwal and J. Robert Selman firstly introduced graphite as the anode materials for lithium-ion batteries.[94] With decades of development, graphite has become the most successful and widely commercialized anode materials for lithium-ion batteries. The layered structure of graphite provides an ideal space for lithium ions to insert and extract during the cycling. The intercalation mechanism of lithium-carbon (Li_xC_n) is described as the reversible reactions below:[95]

$$Li_xC_n \leftrightarrow xLi^+ + xe^- + C_n$$

As shown in Figure 1.9, graphite with perfect crystalline structure can form a lithium-carbon compound with every six carbon atoms take one lithium atom and possess a theoretical capacity of 372 mA h g^{-1} during the intercalation/deintercalation process.[96]

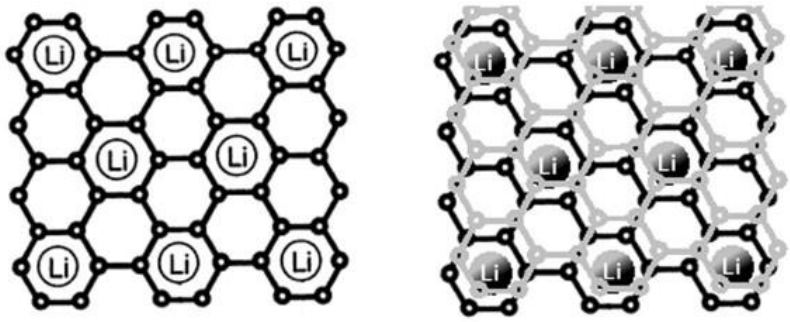

Figure 1.9 Schematic of lithium intercalation in graphite, lithium ions are inserted in every

second carbon hexagons and between the graphite layers.[70]

Although graphite has the properties of high initial coulombic efficiency, low working potential and long lifespan with stable structure, the specific capacity and rate performance of graphite anodes still need to be further improved. Ding modified graphite with a thin AlF_3 layer coated on the powders, and this AlF_3-coated graphite delivers a higher initial discharge capacity of 337 mA h g^{-1} and longer lifespan with capacity retention of 92% after 300 cycles.[97] Cheng reported a multi-channel graphite with surface etched by alkali compounds to increase the number of sites for lithium ions intercalation to reduce the diffusion distance of lithium ions and improve the rate capability of the battery.[98] Kim took the advantage that TiO_{2-x} coated layer can reduce the interfacial resistance between the electrode and the electrolyte to coat TiO_{2-x} on the surface of graphite, and the modified graphite anode exhibited 98.2% capacity retention at a high rate of 5 C without any degradation of the battery performances.[99]

1.4.2.1.2 Hard carbon

Hard carbon has been investigated as an anode candidate to replace commercialized graphite in lithium-ion batteries. Hard carbon has no graphitic structure and it is usually prepared from pyrolysis of polymers.[100] Compared to graphite, hard carbon has larger gap space for lithium ions insertion due to its irregular and disorder arrangement of carbon atoms. As a result, hard carbon delivers a higher capacity of 526 mA h g^{-1} (about 40% greater than graphite) with an initial coulombic efficiency of 80%.[101]

Although hard carbon has the advantages of higher capacity, long cycle life and safety, it displays a low initial coulombic efficiency and high voltage hysteresis.[102-103] In order to improve the electrochemical performances of hard carbon, tremendous efforts including modification of the electrode surface, design of the electrode structure and composite with other materials have been made. Jafari synthesized a nanoporous hard carbon electrode with large specific surface area that can accommodate more lithium ions and buffer the volume change during the lithium ions intercalation to improve a better rate capability and longer cycle life.[104] Kim prepared a hard carbon@microcrystalline graphite composite with core-shell structure to achieve a reversible capacity of 297.8 mA h g^{-1} with an initial coulombic efficiency of 89.8%, and the capacity retention is 97% after 250 cycles.[105]

1.4.2.1.3 Carbon nanotubes

Carbon nanotubes (CNTs) are tubes composed by carbon atoms with typical diameters at the order of nanometers. Single-walled CNTs can be regarded as a graphene sheet roll over into a seamless cylinder with typical diameter on the order of 1.4 nm; while multi-walled CNTs consist of concentric cylinders with an interlayer spacing of 3.4 Å and a diameter typically on the order of 10–20 nm.[106] The nanostructure of multi-walled CNTs and single-walled CNTs are shown in Figure 1.10(a) and Figure 1.10(b), respectively.

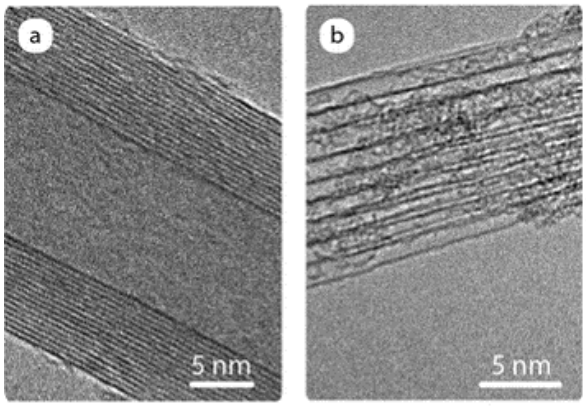

Figure 1.10 Transmission electron micrographs of an as-produced (a) multi-walled CNTs and (b) single-walled CNTs.[107]

As an allotrope of graphite, CNTs have aroused intense attention in energy storage due to their remarkable electrical conductivity (10^6 S m^{-1} at 300 K for single-walled CNTs and $>10^5$ S m^{-1} for multi-walled CNTs),[108] exceptional tensile strength (300 GPa for single-walled CNTs and 1000 GPa for multi-walled CNTs)[109] and excellent thermal conductivity (3000 W m^{-1} K^{-1} for single-walled CNTs and 6000 W m^{-1} K^{-1} for multi-walled CNTs).[110]

CNTs have been demonstrated as promising anode materials for lithium-ion batteries due to their remarkable electrical conductivity that can facilitate electrons transport, the structural integrity that can alleviate the pulverization of active materials during the charging/discharging process and the capability of composing the free-standing electrodes to provide physical support for metal anodes such as silicon or tin. Landi reported a free-standing single-walled CNTs anode (SWCNT) with a capacity of 520 mA h g^{-1} and good cycle stability that can maintain 95% of the initial capacity after 10 cycles.[111] Lahiri demonstrated a binder-free multiwall CNTs anode with a high reversible capacity of 767 mA h g^{-1} at a high discharging rate of 3.0 C (1.116 Ag^{-1}) with no capacity degradation in 50 cycles and a high coulombic

efficiency at 99%.[112] Ren developed aligned multi-walled CNTs fibers (MWCNT) as the lithium-ion battery anode that can achieve a capacity of 174.40 mA h g^{-1} at a current density of 2×10^{-3} mA.[113] Di Lecce reported a multiwalled CNTs anode that can deliver a capacity of 380 mA h g^{-1} at the current density of 124 mA g^{-1} with a small voltage hysteresis and high coulombic efficiency of 99.6%.[114] Kang used thermal compression process to synthesize a multi-stacked 3D CNTs anode with a high surface area and a bulk density that is twice to that of graphite anode to achieve a high mass loading of 1.85 g cm^{-3} with an excellent volumetric capacity of 465 mA h cm^{-3} at 0.5C.[115]

Although CNTs anodes have miscellaneous properties that can be applied in batteries, they still suffer from low coulombic efficiency, lack of voltage plateau and large voltage hysteresis issues.[116] CNTs anode can display a high specific capacity at the initial cycle, but there is a large percentage of lithium ions are consumed rather than stored in the anode and thus lead to a low coulombic efficiency.[117] CNTs anode also has a problem of flat voltage plateau that is caused by the broad changes in voltage as the cell discharges.[118] Another problem is that the working potential of CNTs anode is usually 0.6 V–3 V (vs Li/Li^+) higher than the potential of a commercial graphite anode, and this results in a large voltage hysteresis during the cycling.[119] Therefore, amelioration and modification of CNTs anode are still deserved further research.

Vinayan composited graphene sheets with multi-walled CNTs (graphene-MWNTs) to achieve a discharge capacity of 768 mA h g^{-1} after 100 cycles, the improved electrochemical performance of CNTs anode can be attributed to the strong electrostatic interaction between graphene sheets and multi-walled CNTs that can prevent the restacking of graphene and provide a shorten diffusion distance for lithium ions.[120] The nanostructure of graphene-

MWNTs composites is shown in Figure 1.11.

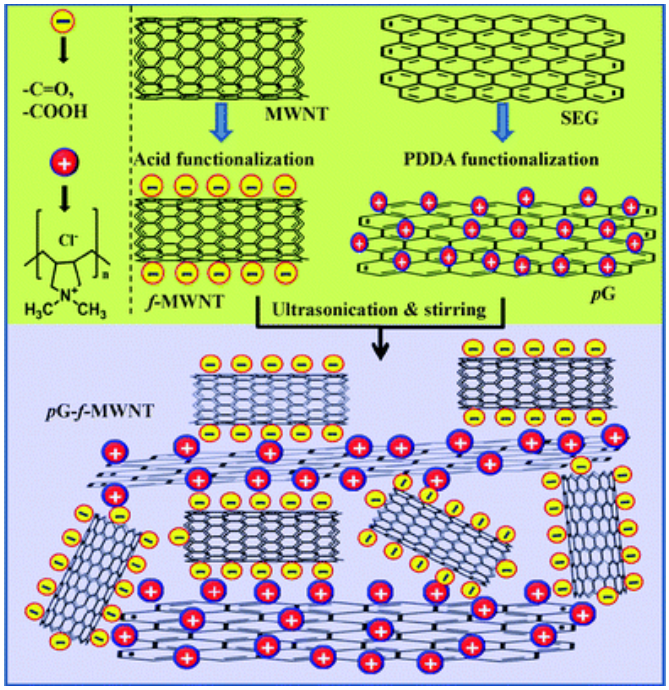

Figure 1.11 Schematic diagram of graphene-MWNTs composites.[120]

Park fabricated a three-dimensional aligned mesoporous CNTs filled with Co_3O_4 nanoparticles composites (Co_3O_4/MCT) as the anode material for lithium-ion battery, and the composites exhibit a high reversible capacity of 627 mA h g^{-1} for 50 cycles with less than 0.4% capacity loss per cycle.[121] The improved electrochemical performance of Co_3O_4/MCT can be ascribed to the shorten diffusion distance provided by the three-dimensional mesoporous CNTs and nanosize effect offered by Co_3O_4 nanoparticles. The structure of Co_3O_4/MCT is shown in Figure 1.12.

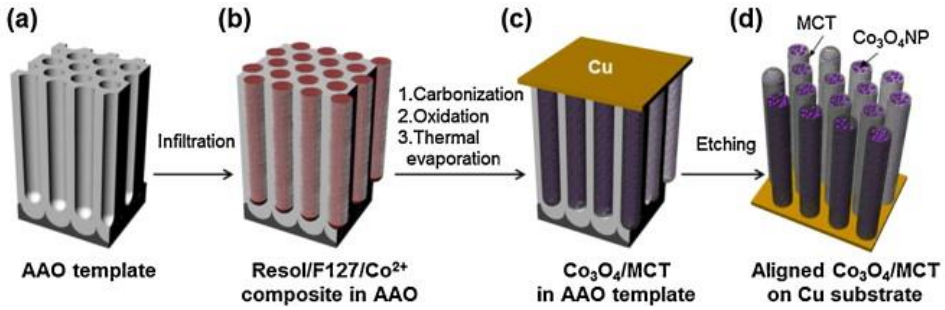

Figure 1.12 Process flow diagram for the preparation of a Co_3O_4/MCT composite aligned on a Cu current collector using a porous AAO template.[121]

1.4.2.1.4 Graphene

Graphene is a kind of two dimensional sheet of sp^2 hybridized carbon, it can be stacked to form three dimensional graphite, rolled to form one dimensional nanotubes and wrapped to zero dimensional fullerenes.[122] Each carbon atom in graphene is connected to three nearest carbon atoms with σ-bond, and contributes one electron to a conduction band that extends over the whole graphene sheet.[123] The basic structure of graphene is shown Figure 1.13.

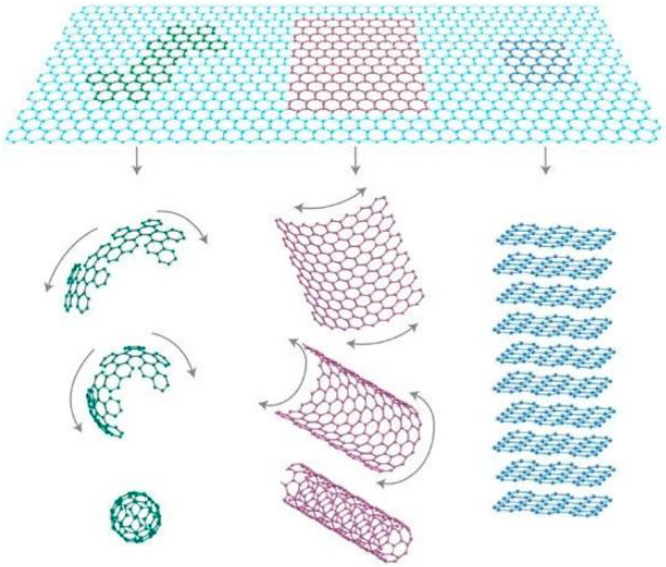

Figure 1.13 Graphene is the base for its allotropic carbonaceous materials.[124]

For a very long time, graphene is thought to be an academic concept but not existed substance in real life until Novoselov isolated a single-atom-thick layer of carbon in 2004.[125] Single layer graphene has extraordinary mechanical strength with a Young's modulus of 1.0 TPa and superior thermal conductivity of 5000 W m^{-1} K^{-1} which is 10 times of that of copper.[119] Graphene also has remarkable electron mobility (2.5×10^5 cm^2 V^{-1} s^{-1} at room temperature)[126] which lead to an excellent performance in electric conduction.[127] In addition, graphene also has a good optical absorption[128] and endurance of extremely high current densities.[129-130]

	Fullerene	**Carbon nanotube**	**Graphene**	**Graphite**
Dimensions	0	1	2	3
Hybridization	Mostly sp^2	Mostly sp^2	sp^2	sp^2
Hardness	High	High	Highest (for single layer)	High
Tenacity	Elastic	Flexible, elastic	Flexible, elastic	Flexible, non-elastic
Experimental Specific surface area (m^2 g^{-1})	80-90	~1300	~1500	~10-20

Electrical conductivity (S cm^{-1})	10^{-10}	Structure dependent	~2000	Anisotropic: 2×10^4~3×10^4
Thermal conductivity (W m^{-1} K^{-1})	0.4	3500	4840~5300	Anisotropic: 1500~2000

Table 1.1 The comparison of properties of graphene and other typical carbonaceous materials.[131]

As shown in Table 1.1, graphene can be considered as the most promising material for electrochemical energy storage system compared to other typical carbonaceous materials. First of all, graphene has the highest electrical conductivity coefficient among the rest of materials. This feature can help reduce the resistance during charge transfer process, improve rate performance and increase the energy density of the battery. Second, the specific surface area of graphene ranks the top of all other carbon-based materials which means that graphene can store more lithium ions both on internal surfaces and the empty nanopores existed between several layers.[131] The more lithium ions stored in electrode materials, the higher specific capacity will the electrode materials be. Graphene can provide a specific capacity of 744 mA h g^{-1} by a Li_2C_6 stoichiometry that is twice than the capacity of graphite (372 mA h g^{-1}).[132] The large specific area of graphene also facilitates the transport of ions and electrons and lead to an improvement of the rate capability of the battery. Third, graphene has a better flexibility than brittle and non-elastic graphite which can be favorable in bendable and portable electronic

devices. All of these unique characteristics laid the status of graphene in energy storage field, especially the battery applications.

Typical methods of mass production for graphene are summarized in Figure 1.14. The first method is mechanical exfoliation, the core of this method is to use external force to overcome the van der Waals attraction between adjacent graphene flakes to acquire graphene from the graphite.[133] The second approach is chemical vapor deposition (CVD), this approach allows the growth of high quality and uniform graphene, but this method will consume a large amount of energy since the production process is operated at a high temperature.[134-135] The third method is chemical exfoliation of graphitic materials, this method has been widely used in industry since it can produce bulk quantity of graphene at one time with relatively low costs; however, this method cannot grow very high-quality graphene.[136] The fourth approach is liquid-phase exfoliation, the basic procedure of this method is to expose graphite or graphite oxide powders into particular solvents and then sonicate solutions to acquire graphene.[137] Since the energy input of liquid-phase exfoliation is relatively low compared to the other approaches, this method usually has the advantage of low cost. Another method is epitaxial growth of graphene on silicon carbide (SiC), this method can control the number of graphene layers grown on the surface of SiC; unfortunately, the high cost of SiC wafer and high temperature required in the process have hindered the further applications of this method.[138-139]

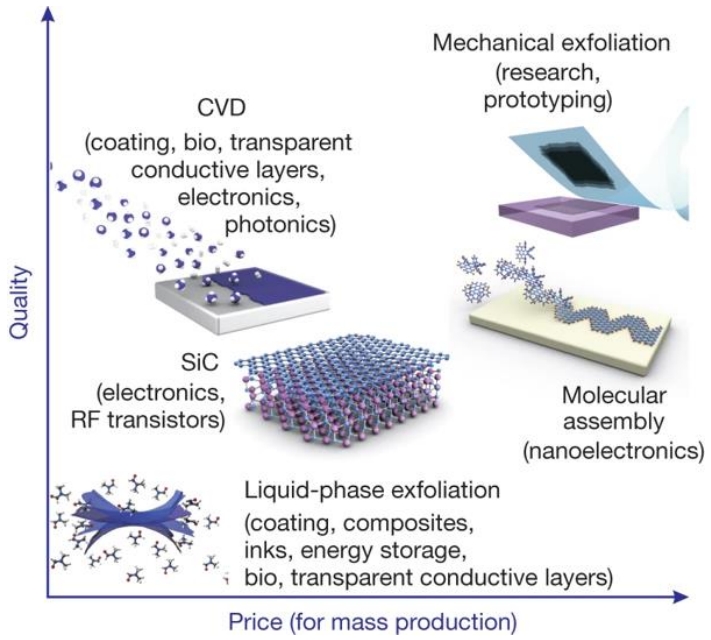

Figure 1.14 Several methods of mass-production of graphene, which allow a wide choice in terms of size, quality and price for any particular application.[140]

Graphene-based anodes have variable structures such as graphene sheets,[141] graphene spheres,[142] graphene fibers,[143] graphene ribbon[144] and three-dimensional graphene foam,[145] graphene aerogel[146] and graphene hydrogel.[147]

Graphene sheets can be prepared from graphite powders through chemical and thermal exfoliation process. The thin film structure of graphene can provide plentiful active edge sites to react with lithium ions, and facilitate the transport of ions and electrons by offering shorten diffusion pathways from a colossal surface area. Lian reported a graphene sheet with only four layers, and this tiny-layer graphene sheet can be applied as anode material for lithium-ion battery to achieve an initial capacity of 1264 mA h g^{-1} at a current density of 100 mA g^{-1}, the reversible capacity of this graphene sheet can be maintained at 848 mA h g^{-1} for 40 cycles.[122] Wang prepared graphene nanosheets as the anode for lithium-ion battery, this anode displayed

an initial capacity of 945 mA h g^{-1} and a reversible capacity of 650 mA h g^{-1} with no more than good cycling stability for 100 cycles.[148] The irreversible capacity decay can be attributed to the formation of solid electrolyte interface (SEI) layer. Zhang synthesized nanoporous graphene sheets to apply in the lithium-ion battery, the specific capacity of this anode can be retained at 800 mA h g^{-1} with a coulombic efficiency of 95.2% for 100 cycles.[149] The synthesis process of nanoporous graphene sheets is shown in Figure 1.15.

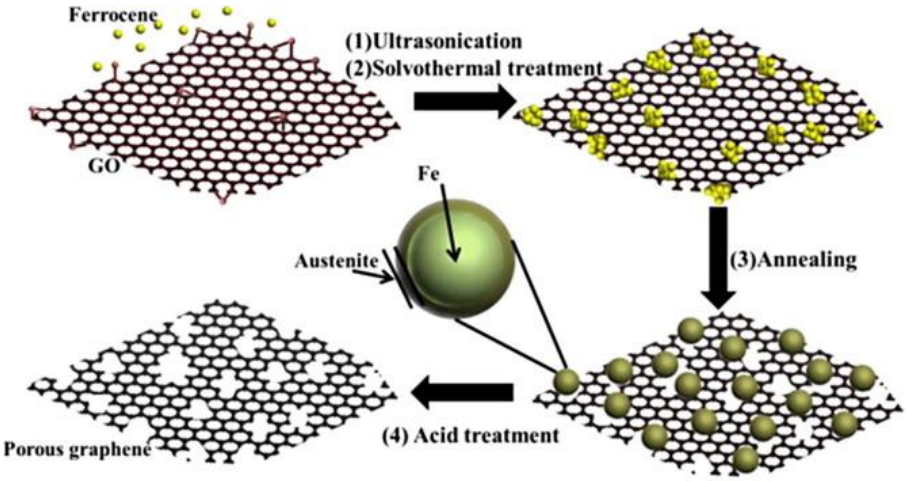

Figure 1.15 Schematic representation of the formation mechanism of nanoporous graphene.[149]

Although the progress of graphene nanosheets anodes has been made in lithium-ion batteries, there are still some problems related to this kind of nanostructure materials. The most significant issue is that graphene sheets tend to aggregate due to the van der Waals forces, and the severe aggregation will cause the loss of active reaction sites for lithium ions and reduction in effective surface area that can contact with electrolyte. Hence, graphene anodes with sphere or ball structure aroused the attention. Cai developed an ultrathin-shell graphene hollow spheres with a uniform thickness of only 5 nm as the anode material for lithium-ion battery, this graphene spheres anode exhibited a high reversible specific capacity of 249.3 mA h g^{-1} at

a high current density of 5 A g^{-1}, and 97.1% of the capacity can be maintained even after 100 cycles.[150] The hollow sphere structure can not only prevent the agglomeration of graphene nanosheets, but also decrease the diffusion distances of lithium ions with an interconnected structure. Besides, the porous interconnected graphene spheres can also provide an electrically conductive network to facilitate the transport of electrons, and abundant reaction sites for lithium ions storage due to its large surface area.

Graphene spheres are also widely used as the carbon support for metal oxide anodes of lithium-ion batteries. For instance, Yu composited ordered mesoporous graphene spheres (OMGSs) with GeO_2 nanoparticles as the anode for lithium-ion battery, and this anode delivered a high specific capacity of 1230 mA h g^{-1} at the current density of 0.2 A g^{-1}, and GeO_2@OMGSs can still exhibit a capacity of 770 mA h g^{-1} with a coulombic efficiency of 98% even after 500 cycles.[151] The highly ordered mesoporous graphene spheres endure the mechanical stress of volume expansion from GeO_2 nanoparticles during the cycling and enhance the lithiation and delithiation kinetics with large surface area and porous structure. The preparation steps and structure of GeO_2@OMGSs are shown in Figure 1.16.

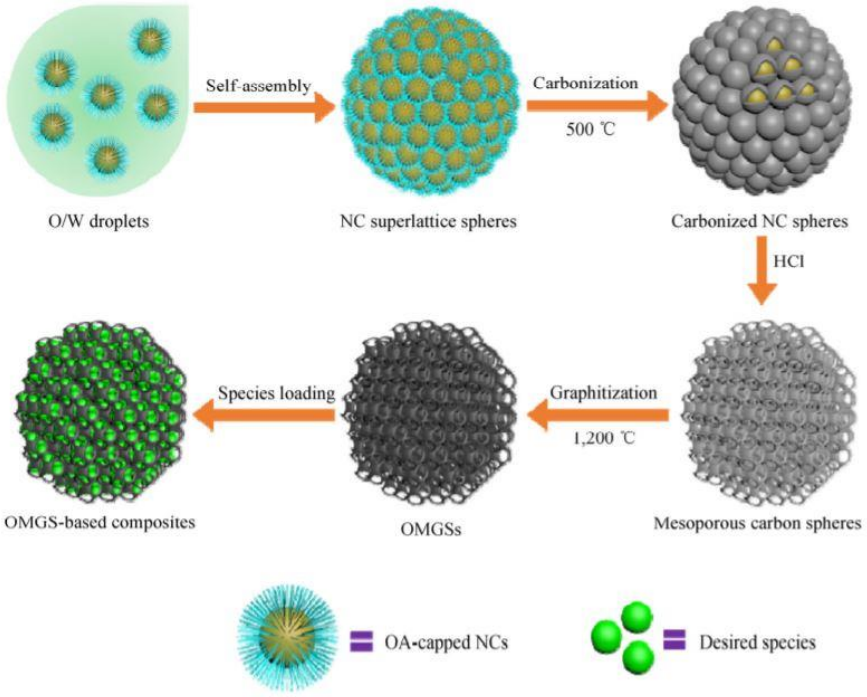

Figure 1.16 Schematic illustration of the overall procedure for synthesizing OMGSs and related OMGSs-based composites.[151]

Three-dimensional graphene materials that have large specific surface area, continuous electron conductive network, rapid ion-diffusion pathways and robust mechanical strength have become a cutting-edged research direction for lithium-ion batteries.[152]

Duan prepared a solvated graphene frameworks (SGFs) by using a solvent-exchange approach, the SGFs anode demonstrated a high reversible capacity of 1158 mA h g^{-1} at 0.1 A g^{-1} which is 2.6 times higher than that of unsolvated graphene, excellent rate capability (472 mA h g^{-1} and 307 mA h cm^{-3} at 5.0 A g^{-1}), and an ultra-stable cycling performance with a 93% capacity retention at the current density of 5 A g^{-1} for 500 cycles.[152] The remarkable electrochemical performances of SGFs are mainly ascribed to the large surface area and faster ions/electrons transfer provided by the porous networks of SGFs with an increased intersheet

distance. The synthesis procedure of SGFs is shown in Figure 1.17.

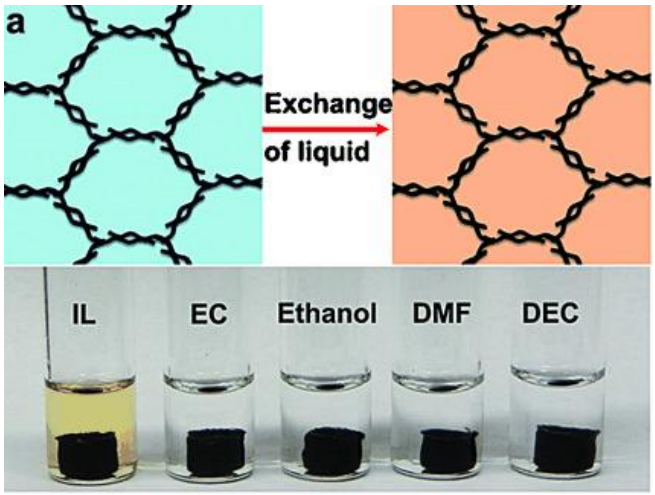

Figure 1.17 Schematic representation of solvent exchange for the preparation of SGFs (top) and photographs of SGFs in various organic solvents (bottom).[152]

Wang reported a three-dimensional Fe_2O_3/graphene sheets aerogels (Fe_2O_3/GS) to apply as the anode for lithium-ion battery, this hybrid anode exhibited a remarkable rate capability (930 mA h g^{-1} at 0.5 A g^{-1} and 520 mA h g^{-1} at 4 A g^{-1}) and stable cycling performance that can maintain the capacity of 733 mA h g^{-1} at a current density of 2 A g^{-1} for 1000 cycles.[153] The superior electrochemical performances of Fe_2O_3/GS can be ascribed to the large specific surface area and fast electron-ion diffusion pathways that provided by three-dimensional interconnected framework of graphene. Besides, Fe_2O_3 nanoparticles also contribute the capacity for this three-dimensional electrode during the cycling. The synthesis process and structure of Fe_2O_3/GS are shown in Figure 1.18.

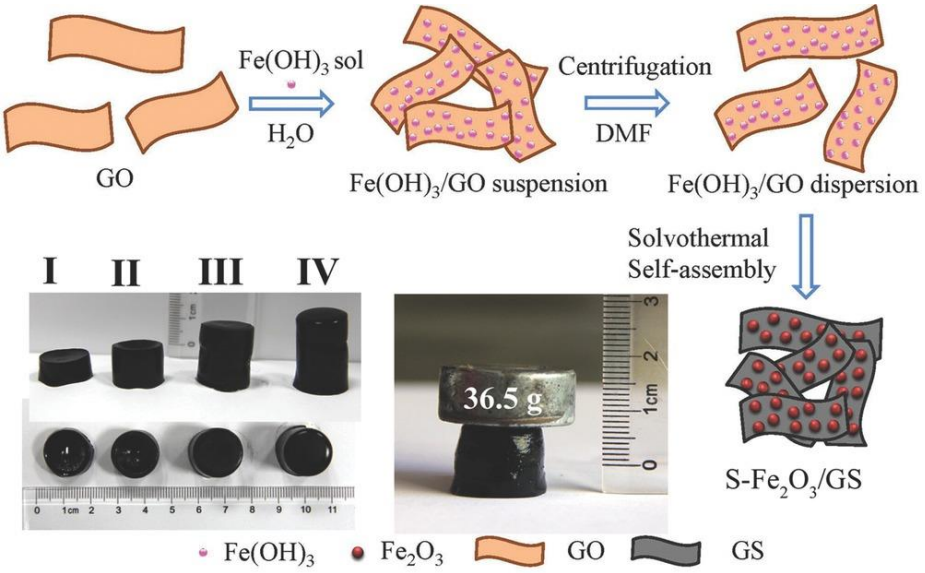

Figure 1.18 Schematic illustration of preparation of S-Fe_2O_3/GS aerogels.[153]

1.4.2.2 Lithium titanate oxide

Lithium titanate oxide (LTO) has been extensively investigated as the anode candidates for lithium-ion batteries for decades. The structure of $Li_4Ti_5O_{12}$, $Li_7Ti_5O_{12}$ and $Li_9Ti_5O_{12}$ are shown in Figure 1.19.

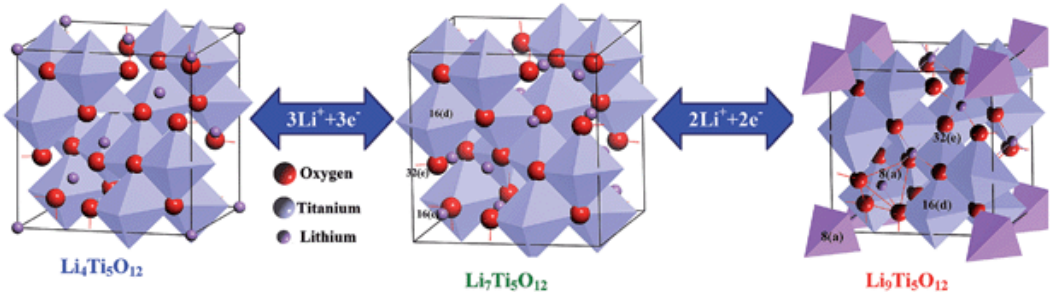

Figure 1.19 Structure of $Li_4Ti_5O_{12}$, $Li_7Ti_5O_{12}$ and $Li_9Ti_5O_{12}$.[154]

$Li_4Ti_5O_{12}$ spinel is regarded as the most promising material due to its zero strain features which lead to negligible volume expansion during the cycling, stable potential platform at 1.55 V (vs. Li/Li^+) which is above the potential of SEI formation, long cycle life and high

safety.[155-156] The theoretical specific capacity of LTO anode in lithium-ion battery is 175 mA h g^{-1}.[157] However, LTO anodes usually suffer from poor electrical conductivity and low lithium ions diffusion coefficient that leads to unsatisfactory of rate performances in lithium-ion batteries. To address the issues for poor rate capability of LTO anodes, tremendous efforts such as modification and design of the anode structures and adjunction of conductive agents have been made.

Jung developed microscale C-$Li_4Ti_5O_{12}$ composites with a carbon layer coated on the surface of $Li_4Ti_5O_{12}$ particles to form sphere structure, this composite anode delivered a high capacity of 165 mA h g^{-1} at 0.17 A g^{-1}which is very close to the theoretical capacity of $Li_4Ti_5O_{12}$, and the capacity of this anode can retain at 160 mA h g^{-1} even though the applied current density was increased to 1.7 A g^{-1}.[158] The structure of C-$Li_4Ti_5O_{12}$ composites is shown in Figure 1.20. The uniform carbon layer wrapped on the surface of $Li_4Ti_5O_{12}$ particles not only reinforced the electrical conductivity of LTO, but also provide the possibility for faster ions and electrons diffusion with the nanopores existed in the carbon layer. Besides, the mixed valence state of Ti^{3+} and Ti^{4+} also has a positive effect on the improvement of electrical conductivity ana rate capability of the anode.

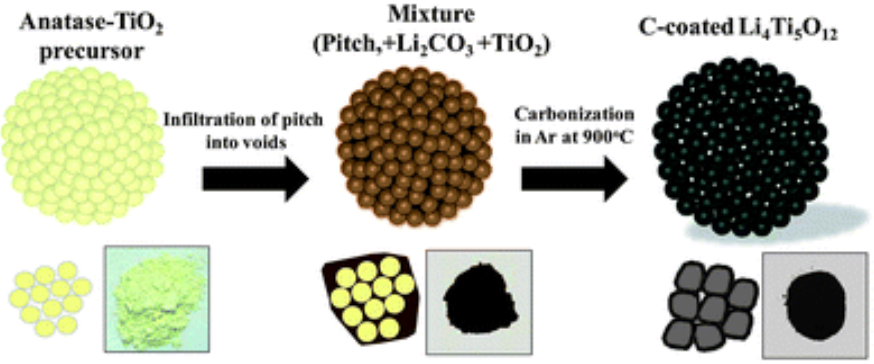

Figure 1.20 Schematic illustration of synthetic process of microscale, spherical, carbon-coated $Li_4Ti_5O_{12}$ and photographs of material formed during synthesis.[158]

Apart from the modification and design for the structure of LTO, the addition of materials with high electrical conductivity is another approach to improve the drawbacks of LTO anode. Graphene has been widely used as the conductive additives in LTO anodes due to its outstanding electrical conductivity, large specific surface area and high mechanical strength. For instance, Yang fabricated a composite of LTO with cathodically induced graphene (CIG) as the anode for lithium-ion battery, the composite exhibited an outstanding cycling performance for 96.2% capacity retention at 0.5 C for 500 cycles and excellent rate capability (162 mA h g^{-1} at 10C and 126 mA h g^{-1} at 100 C).[155] The structure of LTO/CIG is demonstrated in Figure 1.21.

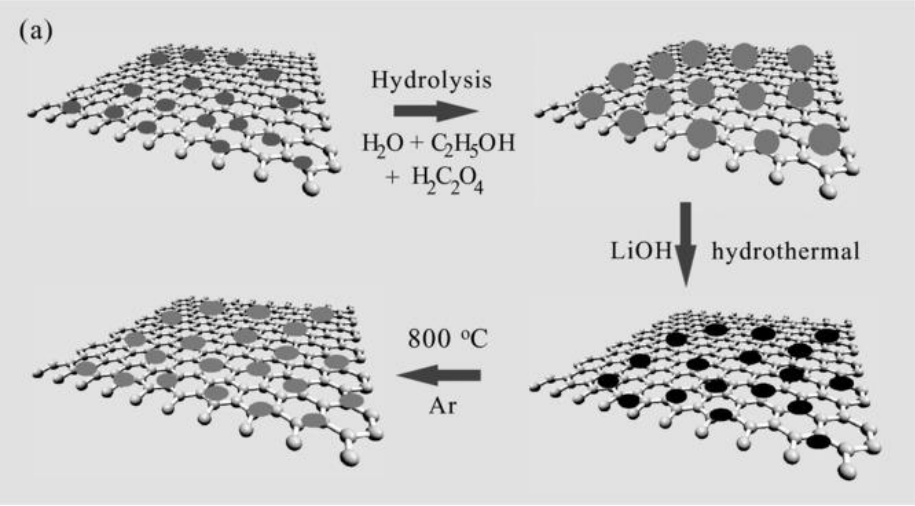

Figure 1.21 Schematic illustration for the fabrication of LTO/CIG composite.[155]

1.4.2.3 Alloys

Alloys have been investigated as promising substitute anodes for lithium-ion batteries since they possess theoretical specific capacities that are 2–10 times higher than that of graphite and

4–20 times higher than that of LTO.[159] Lithium can alloy with numerous metals, such as silicon, tin, antimony, aluminum, bismuth and so on.[160] Although alloy anodes are known for their high specific capacities and safety during the cycling, the commercialization of alloy anodes has been hindered by their severe volume expansion in lithium ions intercalation/deintercalation process and irreversible capacity decay caused by the pulverization of active alloy particles.[161] The comparison of different kinds of alloy anodes are displayed in Table 1.2.

Materials	Graphite	$Li_4Ti_5O_{12}$	Silicon	Tin	Antimony	Aluminum
Density (g cm^{-3})	2.25	3.5	2.33	7.29	6.7	2.7
Lithiated phase	LiC_6	$Li_7Ti_5O_{12}$	$Li_{4.4}Si$	$Li_{4.4}Sn$	Li_3Sb	LiAl
Theoretical specific capacity (mA h g^{-1})	372	175	4200	994	660	993
Theoretical charge density (mA h cm^{-3})	837	613	9786	7246	4422	2681

Volume change (%)	12	1	320	260	200	96
Potential vs. Li (~V)	0.05	1.6	0.4	0.6	0.9	0.3

Table 1.2 Comparison of the theoretical specific capacity, charge density, volume change and onset potential of various anode materials.[159]

Compared to the other alloys in Table 3, silicon (Si) anode has triggered enormous interests in energy storage due to its highest specific capacity (4200 mA h g^{-1}), huge volumetric capacity (9786 mA h cm^{-3}), low discharge potential (0.4 V vs Li/Li^{+}) and abundant reserve on earth. Unfortunately, the severe volume expansion of Si anode in lithium-ion battery can cause nearly 30% capacity decay only after five cycles.[162] In order to address the huge volume change and unstable SEI layer of Si anode during the cycling, several strategies have been exploited. As summarized in Figure 1.22, size control, surface coating, active/inactive alloy, void space design and composites are five typical approaches to solve the issues of Si anodes.[163] Decreasing the size of Si particles into nano range can mitigate the stress during the cycling and shorten the ions/electrons diffusion pathways to improve the rate capability of Si anodes. Coat a carbonaceous layer on the surface of Si anode can increase the electrical conductivity and avoid unfavorable reactions with the protection of outer layer. Active-inactive alloy can dilute lithium ions with the inactive phase to improve rate capability and improve the electrical conductivity of Si anode at the same time. Construct a void space structure can buffer the

volume expansion of Si particles and prevent the continuous growth of SEI layer. Composite Si particles with other materials can achieve higher energy density with great productivity.

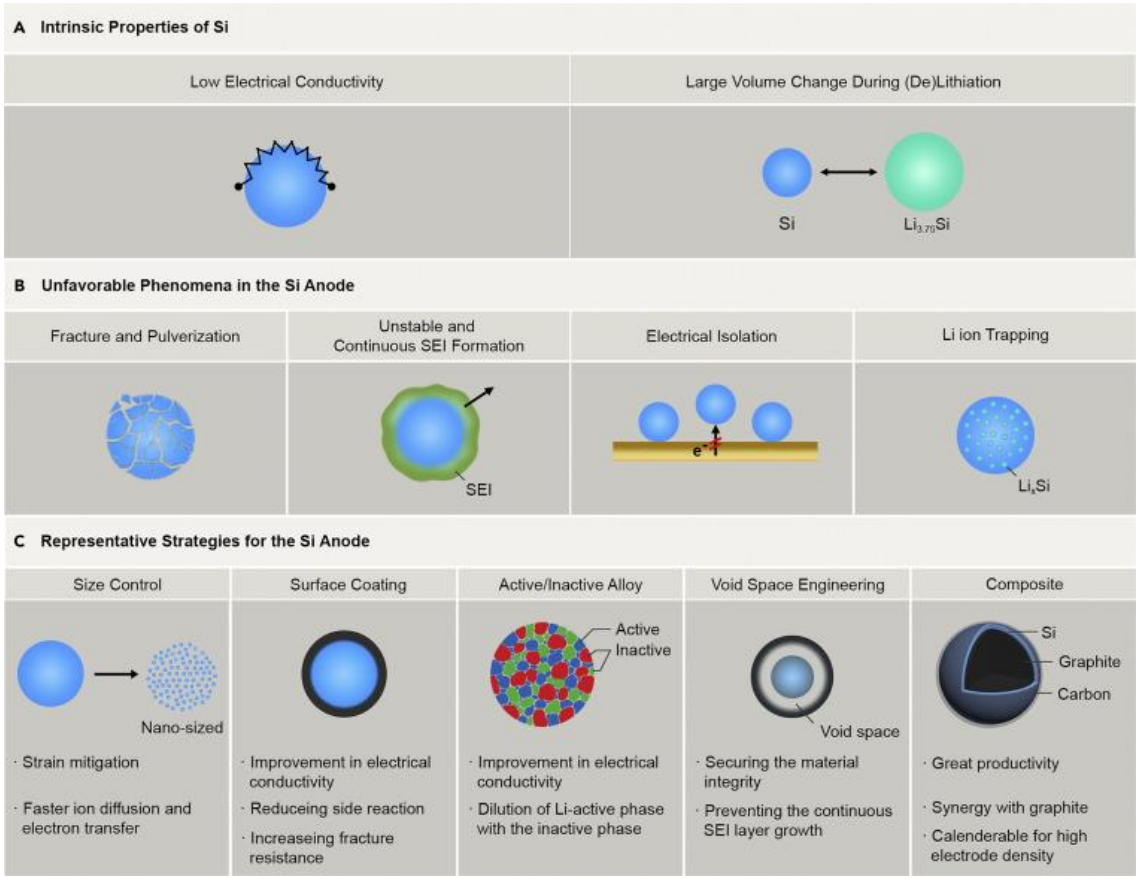

Figure 1.22 Overview of the challenges and representative strategies associated with the Si anode.[163]

Wang demonstrated a silicon nanowire/overlapped graphene sheet core-sheath nanocables intertwined with CNTs (SiNW@G-CNT) to achieve a high reversible capacity of 1120 mA h g^{-1} at a current density of 4.2 A g^{-1} which is approximately three times of a commercial graphite anode with a coulombic efficiency maintains at 99 %–100 %.[164] The nanostructure of SiNW@G-CNT is shown in Figure 1.23. In this hybrid structure, CNTs act as the buffer matrix to accommodate the volume changes of silicon, while overlapped graphene sheets prevent the direct contact of silicon with electrolyte to avoid side reactions and provide a shorten diffusion

pathway for lithium ions during the cycling.

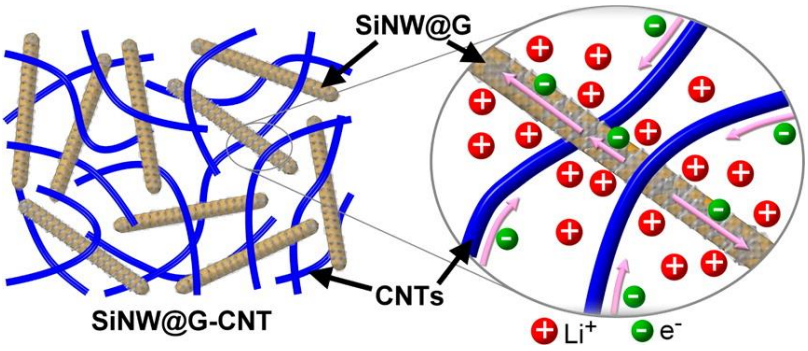

Figure 1.23 Schematic illustration of the 3D intertwined network of SiNW@G nanocables and CNTs.[164]

Cui designed a carbon-silicon core-shell nanowires (SiNWs) anode for lithium-ion battery that exhibits a high capacity of 2000 mA h g^{-1} with coulombic efficiency of 98−99.6% for 80 cycles.[118] The nanostructure of SiNWs is shown in Figure 1.24. Unlike other carbon shell that buffers the volume expansion of silicon anode from the outside, the carbon core that experienced less structural stress in SiNWs can function as a robust mechanical support and provide efficient electron transport pathways at the same time during the cycling.

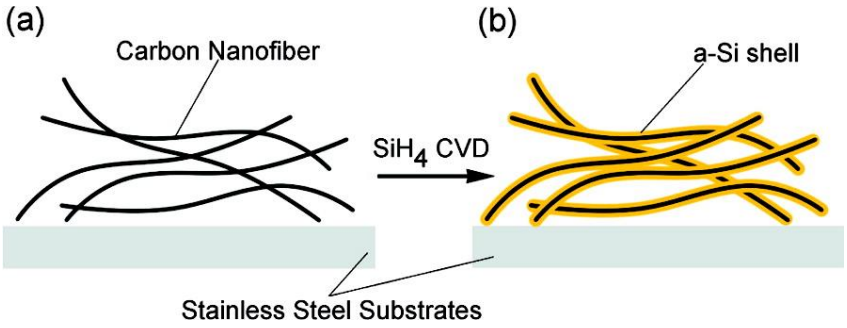

Figure 1.24 Schematic illustration of Si coating onto carbon nanofibers (a) Bare CNFs. (b) C−Si core−shell NWs.[118]

Similar to Si anodes, tin (Sn) anodes have been regarded as another promising alloy anodes

in lithium-ion batteries due to their high theoretical capacity (994 mA h g^{-1}), high tap density (3.15 g cm^{-3}), relatively low voltage (0.6 V vs Li/Li^{+}) and safety in charging/discharging process. The practical applications of Sn anodes are still impeded by the mechanical disintegration and severe capacity fading that caused by huge volume expansion during the cycling. Similar strategies have been applied to Sn anodes to solve the challenges of large volume change.

Wang designed a core-shell structure for Sn@C nanoparticles embedded in graphene nanosheets (Sn@C–GN), this composite anode delivered a specific capacity as high as 1069 mA h g^{-1} and an excellent cycling stability with capacity maintaining at 566 mA h g^{-1} for 100 cycles.[165] The synthesis procedure of Sn@C–GN is shown in Figure 1.25. The void space between the carbon shell and Sn core provided extra space to confine the growth of active Sn particles and buffer the volume expansion of Sn core during the cycling. Furthermore, the electrical conductivity and mechanical strength of the composites were improved by the presence of graphene sheets.

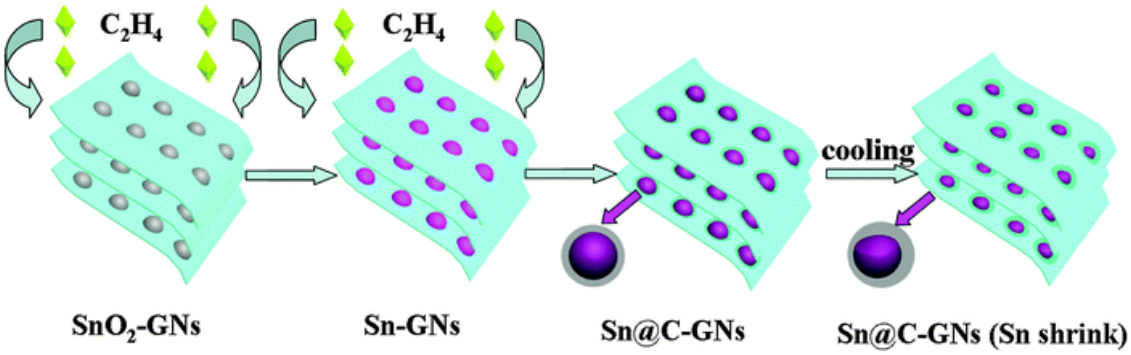

Figure 1.25 Schematic sketch for the Sn@C–GN composite growth procedure.[165]

Zhang encapsulated Sn nanoparticles into hollow elastic carbon spheres (TNHCs), and the

composite anode exhibited a high specific capacity (>800 mA h g^{-1} in the initial 10 cycles and >550 mA h g^{-1} even after 100 cycles).[166] The morphology of TNHCs is displayed in Figure 1.26. The void space of the carbon spheres provides enough buffer for the volume expansion of Sn nanoparticles during the insertion/extraction of lithium ions, and prolong the cycle life with excellent structural integrity. In addition, the hollow carbon spheres also construct a conductive network to enhance the electron transfer efficiency of the anode.

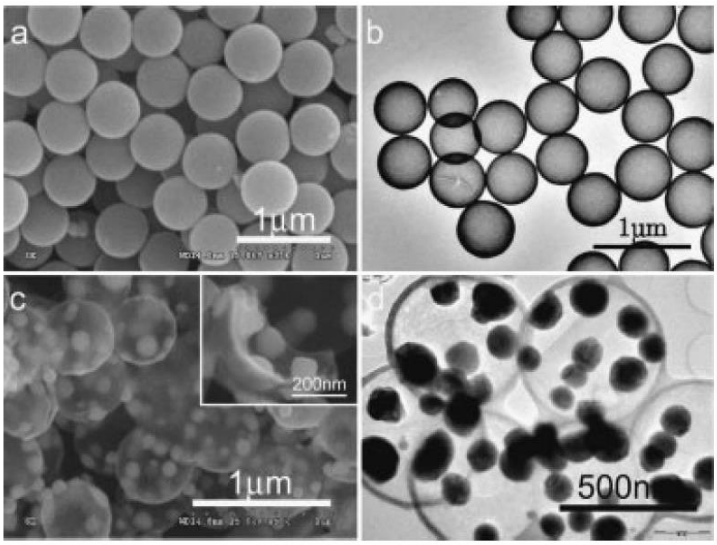

Figure 1.26 (a) SEM image of SnO_2 coated SiO_2 spheres; (b) TEM image of the hollow SnO_2 spheres; (c) and (d) SEM and TEM image of TNHCs, respectively.[166]

1.4.2.4 Transition metal oxides

Compared to alloys, transition metal oxides such as SnO_2, TiO_2, Fe_2O_3 and Co_3O_4 exhibit prolonged cycle life due to the formation of Li_2O that can cushion the volume change and provide crystal structure for lithium ions insertion at the same time.[167] However, the employment of metal oxides in lithium-ion batteries is still dampened by the poor electrical conductivity and unstable cycling performance. Compositing with porous carbonaceous

materials to enhance the electrical conductivity and shorten the diffusion pathways for lithium ions by large surface area has been a common method to address the drawbacks of metal oxide anodes.

Han used sulfur template to fabricate a cage hybrid composite of SnO_2 and graphene (SnO_2@GC) with void space, the composite anode exhibited an ultra-high volumetric capacity of 2415 mA h cm^{-3} at a current density of 100 mA g^{-1} for 300 cycles with 84% capacity retention.[168] The schematic structure of SnO_2@GC is demonstrated in Figure 1.27. The well-designed graphene cage provides adequate void space to buffer the volume expansion of SnO_2 nanoparticles during the lithium ions intercalation/deintercalation process, avoid the pulverization of SnO_2 nanoparticles to prevent the capacity decay, and offer the continuous electrically conductive network to facilitate the electrons transfer and improve the rate capability of the composite anode.

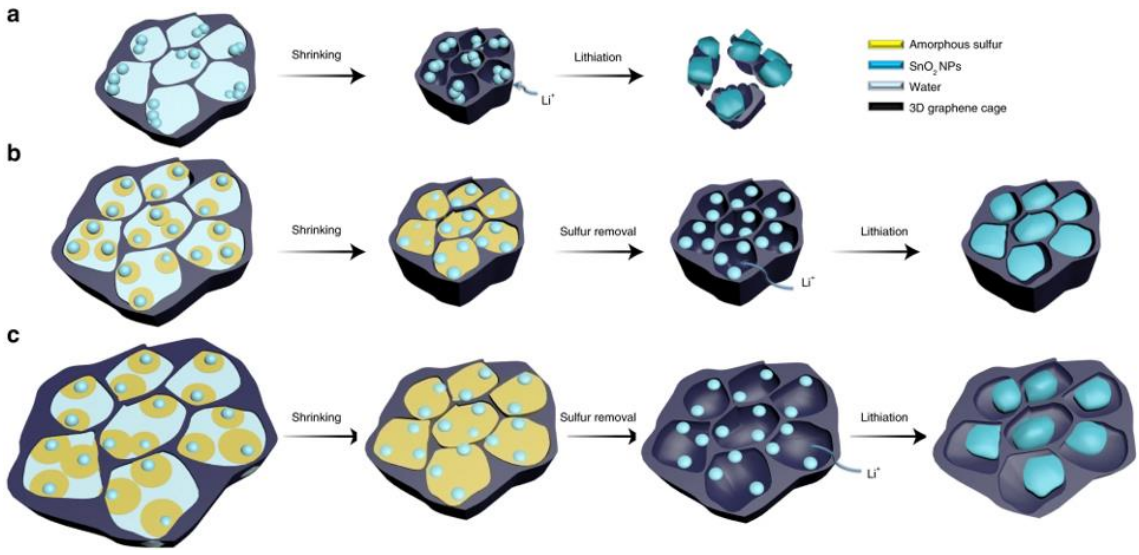

Figure 1.27 Sulfur template control of incorporated void space of SnO_2@GC.[168]

Xin fabricated a composite with TiO_2 nanoparticles condensed on a flower-like graphene oxide sheets, this TiO_2/graphene composite was able to deliver a capacity of 230 mA h g^{-1} at a current density of 17 mA g^{-1} and exhibited a superb cycling stability even at 50 C.[169] The synthesis procedure is illustrated in Figure 1.28. The porous flower-like graphene sheets offer a large surface area to shorten the diffusion distances of lithium ions and enhance electrical conductivity of the composite.

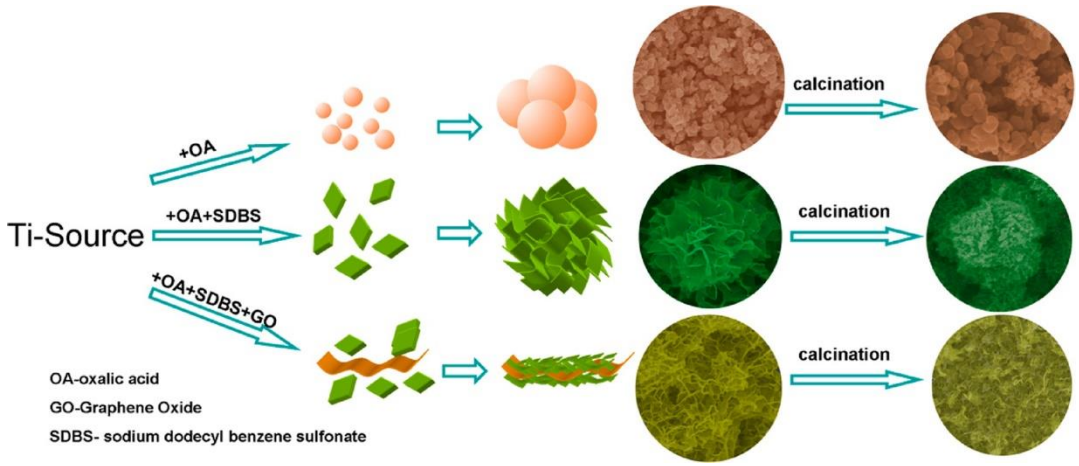

Figure 1.28 Illustration of the preparation processes and growth mechanisms of TiO_2-based nanocomposites.[169]

1.4.2.5 Graphene-alloy composites

Among various types of anode materials for lithium-ion batteries, alloy anodes aroused the attention with their extremely high gravimetric capacities and volumetric capacities, while graphene possess the intriguing properties of high specific surface area, excellent electrical and thermal conductivity and remarkable mechanical strength. Suffered from the restacking the agglomeration issues, graphene anodes usually have a big drop of the effective surface area, and thus lead to a large irreversible capacity loss after the initial cycle with a low coulombic

efficiency.[119, 170] Alloy particles can diffuse into the porous graphene layers easily to reduce the possibility of restacking and provide more activated sites for lithium ions insertion at the same time. Meanwhile, graphene can act as a carrier to support the nucleation of alloy particles, and help build a uniform surface for the composites to inhibit the growth of lithium dendrites that causes the short circuit of the battery. In order to integrate the merits from alloys and graphene anodes, address the severe volume expansion and pulverization issues from alloy anodes, tackle the restacking and agglomeration problems of graphene and increase the capacity of graphene anodes, graphene-alloy composites come into birth.

Progress of graphene-alloy composites have been made in recent decades. Zhang constructed a phosphorus bridge to connect SnO_2 nanoparticles with graphene (SnO_2@P@GO) to apply as the anode for lithium-ion battery, this composite exhibited a specific capacity of 610 mA h g^{-1} at the current density of 100 m A g^{-1} with 95% capacity retention for 700 cycles.[171] The synthesis procedure of SnO_2@P@GO composite is shown in Figure 1.29. The ultra-stable cycling performance and structure integrity of SnO_2@P@GO anode can be attributed to the covalent bonds through P-C and Sn-C-P which can buffer the change of mechanical stress during the volume expansion of SnO_2 nanoparticles.

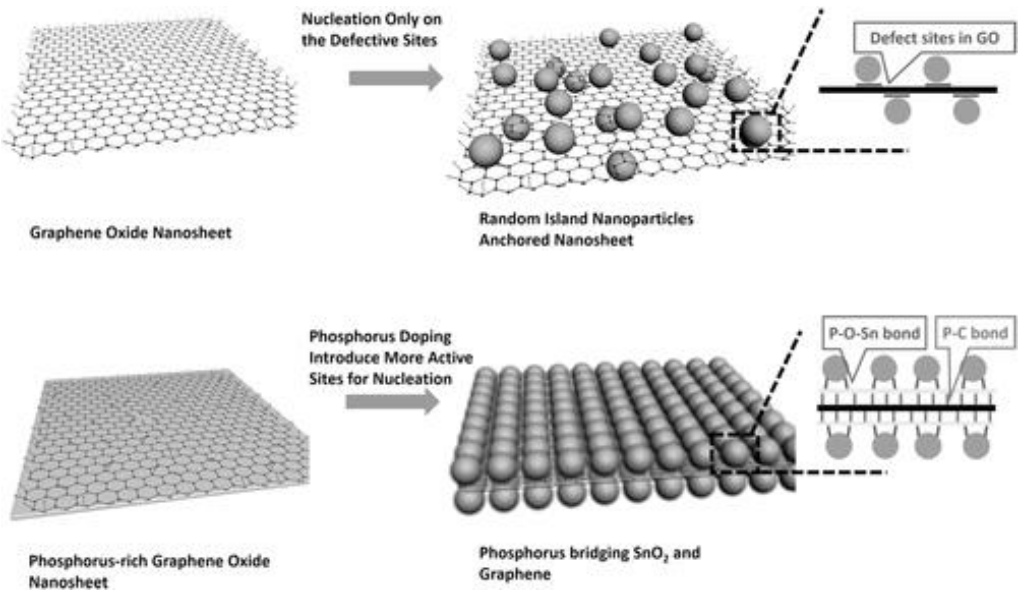

Figure 1.29 The schematic illustrations of formation process of SnO_2 /GO and SnO_2@P@GO.[171]

Teng designed an anode composite with MoS_2 nanosheets vertically grown on the graphene sheets (MoS_2/G), this composite manifests a high reversible capacity of 1077 mA h g^{-1} at 100 mA g^{-1} after 150 cycles with excellent rate capability and extraordinary cycling stability that can maintain the capacity of 907 mA h g^{-1} at 1000 mA g^{-1} after 400 cycles.[172] The nanostructure of MoS_2/G composite is demonstrated in Figure 1.30. The perpendicularly aligned MoS_2 nanosheets can not only prevent the restacking of graphene sheets, but also offer abundant edge sites for lithium ions to react. Besides, the graphene sheets can provide a colossal surface area to accommodate lithium ions as well as offer a shorter diffusion pathway for ions and electrons to facilitate the rate capability of the battery. In addition, the flexible graphene sheets can act as a buffer for volume expansion of MoS_2 nanosheets during the cycling.

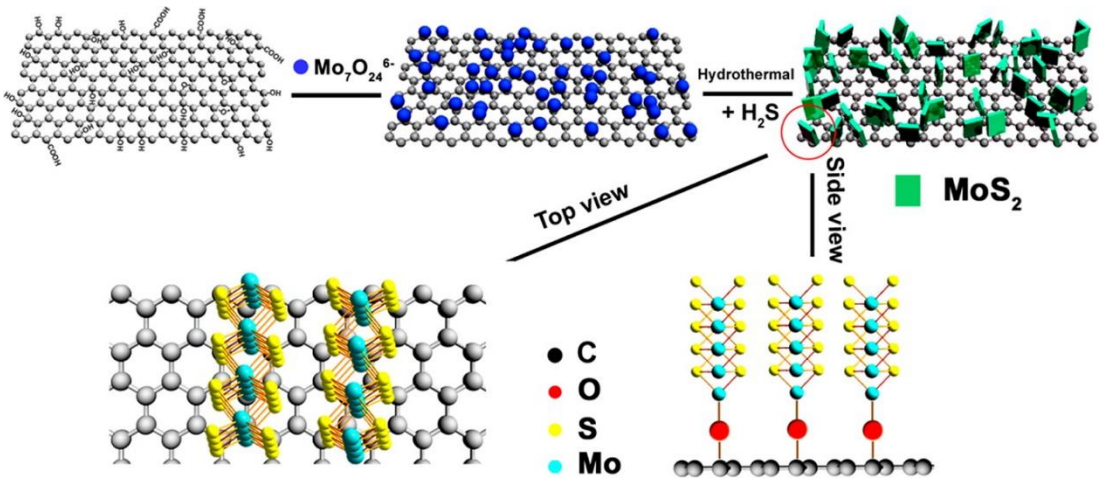

Figure 1.30 Schematic illustration of the synthesis procedure of MoS_2/G.[172]

Choi applied spray pyrolysis to synthesize Fe_3O_4-decorated graphene balls with uniform distribution of Fe_3O_4 nanoparticles on the surface, this composite anode possessed a high discharge capacity of 1210 mA h g^{-1} at the current density of 7 A g^{-1}, remarkable cycling stability that can maintain a capacity of 690 mA h g^{-1} for over 1000 cycles and excellent rate capability (1040 to 540 mA h g^{-1} with the current density increased from 1 to 30 A g^{-1}).[173] The nanostructure of Fe_3O_4-decorated graphene balls are illustrated in Figure 1.31. The uniform distribution of Fe_3O_4 nanoparticles on the graphene sheets can effectively prevent the agglomeration of graphene layers and guarantee enough surface area for lithium ions to accommodate in the anode which is beneficial in the capacity. In addition, the sphere design of the composite can keep the mechanical integrity of the anode, and thus improve the cycling stability of the battery. The porous spheres can shorten the diffusion distances of lithium ions and improve the rate capability of the composite.

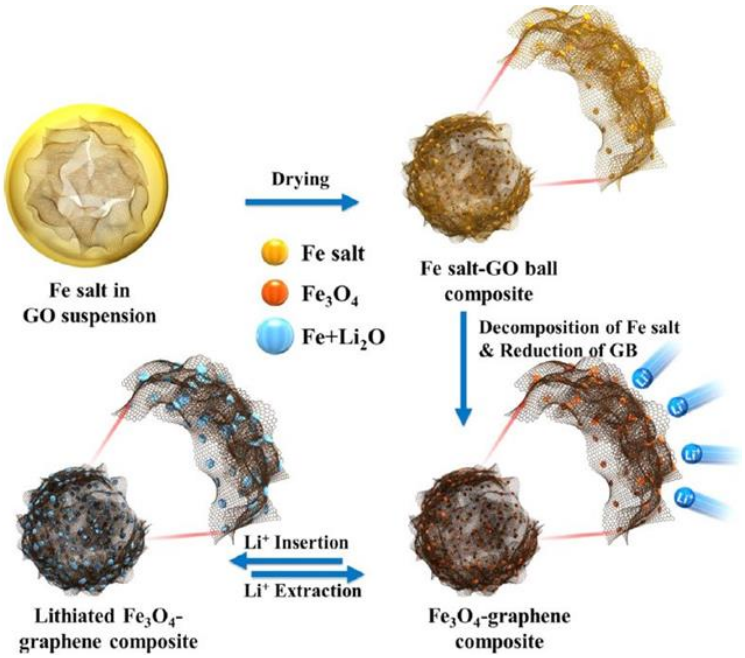

Figure 1.31 Schematic diagram of formation and lithium insertion/desertion mechanisms of Fe_3O_4-decorated hollow graphene ball.[173]

Luo designed a hierarchical composite with foam-like graphene matrix and Sn nanoparticles (F-G/Sn@C), the composite anode delivered a reversible capacity of 506 mA h g^{-1} for 500 cycles and a high-rate capacity of 270 mA h g^{-1} even at the current density of 3200 mA g^{-1} in lithium-ion battery.[174] The schematic structure of F-G/Sn@C is illustrated in Figure 1.32. The foam-like graphene matrix functions as a buffer for the severe volume expansion of Sn nanoparticles during the cycling, as well as a restricted frame to suppress the aggregation of Sn nanoparticles. The capacity exhibited by the composite can be ascribed to the synergetic effect of both Sn nanoparticles and graphene matrix.

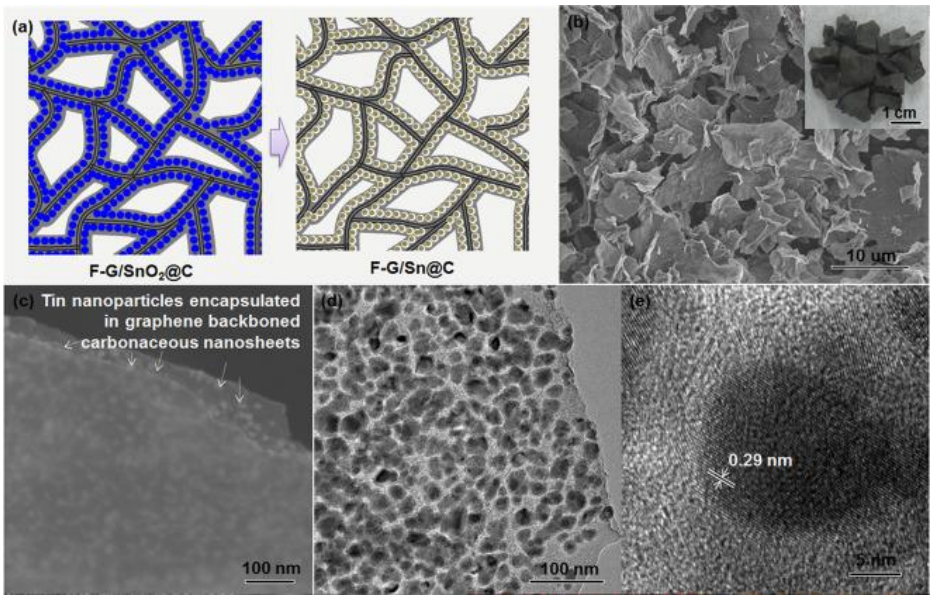

Figure 1.32 (a) Schematic illustration of the synthesis of F-G/Sn@C composite, (b, c) SEM images, (d) TEM image, (e) HR-TEM image.[174]

1.4.3 Cathode materials of lithium-ion batteries

The cathode materials in lithium-ion batteries are the major source of lithium ions during the charging/discharging phases.[175] The most common and commercialized cathode materials for lithium-ion batteries are lithium cobalt oxide ($LiCoO_2$), lithium iron phosphate ($LiFePO_4$), lithium manganese oxide ($LiMn_2O_4$) and lithium layered metal oxides.[176]

The most widely applied cathode material in lithium-ion battery is $LiCoO_2$ which has a distorted rock-salt structure where cations order in alternating (1 1 1) planes.[177] The structure of $LiCoO_2$ is illustrated in Figure 1.33. As the dominant cathode in lithium storage, $LiCoO_2$ has the advantages of high theoretical capacity (274 mA h g^{-1}), high tap density (3.9 g cm^{-3}) and long lifespan.[178] However, $LiCoO_2$ cathode still suffers from a high potential (>4.2 V vs Li/Li^+) that leads to unfavorable bulk phase transition, surface degradation and inhomogeneous

reactions.[179] In order to address the challenges of $LiCoO_2$ cathode, several methods such as modification of the electrode surface and composite with other conductive materials have been attempted. Lee modified the surface of $LiCoO_2$ cathode with a AlF_3 layer, and this composite delivered a capacity of 188 mA h g^{-1} at the voltage of 4.5 V (vs. Li/Li^+) with a 95% capacity retention for 50 cycles.[180] Sun coated graphene quantum dots on the surface of $LiCoO_2$ particles to exhibit a specific capacity of 158.9 mA h g^{-1} with a capacity retention of 82.8 % for 100 cycles.[181]

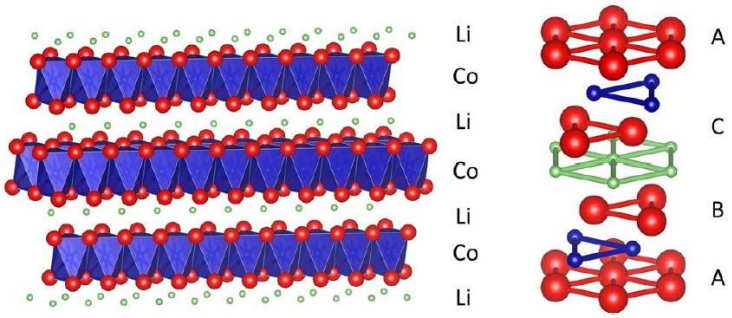

Figure 1.33 Schematic structure of $LiCoO_2$ (red: oxygen; purple: cobalt; green: lithium).[182]

$LiFePO_4$ possesses an olivine-like structure where phosphorus takes up tetrahedral sites, iron occupies octahedral sites and lithium form one-dimensional chains along the (0 1 0) direction.[183] The structure of $LiFePO_4$ is shown in Figure 1.34. $LiFePO_4$ has been known for its flat discharge plateau at 3.3 V vs Li/Li^+, a moderate charge capacity of 170 mA h g^{-1}, negligible volume change, excellent thermal stability and cheap price.[184] Unfortunately, the application of $LiFePO_4$ cathode has been impeded by low electrical conductivity, low tap density and poor performance at low temperature ranges.[185] The drawbacks of poor electrical conductivity and low tap density can be ameliorated by compositing $LiFePO_4$ with other carbonaceous materials such as CNTs or graphene. Li reported a composite of

$LiFePO_4$ particles with multi-walled CNTs that can deliver an initial capacity of 155 mA h g^{-1} at the current density of 0.05 mA cm^{-2}.[186] Wang designed a composite with $LiFePO_4$ particles embedded in the graphene sheets, and the cathode with a three-dimensional conducting network exhibited a discharge capacity of 160.3 mA h g^{-1} at 0.1 C which is very close to the theoretical capacity of $LiFePO_4$.[187]

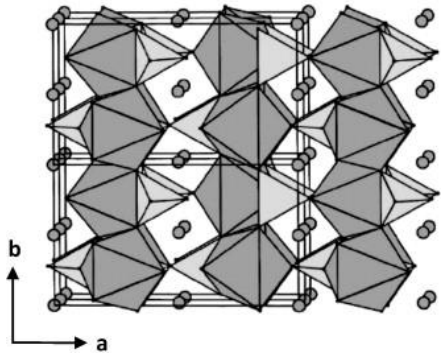

Figure 1.34 The crystal structure of $LiFePO_4$ viewed along the *c*-axis.[188]

$LiMn_2O_4$ provides a three-dimensional connected network that can facilitate the insertion and deintercalation of lithium ions, and the tetrahedral sites that neighbor to empty octahedral sites of Mn_2O_4 are occupied by lithium ions.[189] The structure of $LiMn_2O_4$ is displayed in Figure 1.35. Compared to $LiCoO_2$ cathodes with high toxicity and high cost, $LiMn_2O_4$ cathodes attract the attention due to their non-toxicity, low cost and abundant reserve on earth. The $LiMn_2O_4$ cathode with spinel structure can deliver a theoretical capacity of 148 mA h g^{-1}.[190] However, the obvious capacity decay at elevated temperature and surface degradation that leads to poor cycling stability have been a hamper for the commercialization of $LiMn_2O_4$ cathodes. Tu coated a gold layer on the surface of $LiMn_2O_4$ powders to enhance the electrical conduction and improve the cycling stability of the cathode, the composite displayed a capacity of 125 mA h

g^{-1} for 50 cycles.[191] Yu designed a flexible cathode that composed by hollow carbon nanofibers with truncated conical graphene layers and $LiMn_2O_4$ nanocrystals ($LiMn_2O_4$@C/CNF), this unique cathode exhibited a high specific capacity of 126 mA h g^{-1} with 81% capacity retention for over 1000 cycles at 1C.[192] The hollow carbon nanofibers in the composite provide abundant graphitic edge planes for the accommodation $LiMn_2O_4$ nanocrystals, and graphene layers can bear the high-temperature oxidation resistance during the cycling.

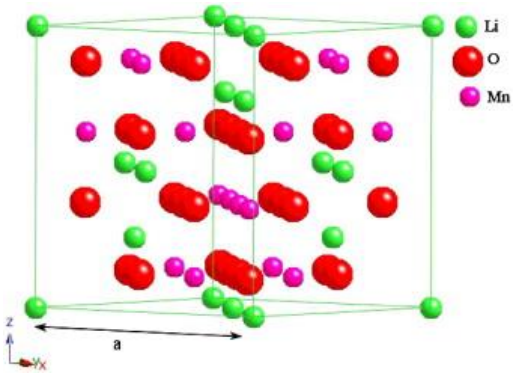

Figure 1.35 The crystal structure of spinel $LiMn_2O_4$.[193]

1.4.4 Current challenges of lithium-ion batteries

Lithium-ion batteries have been the most competitive candidates in electrochemical energy storage system since they have the advantages of high energy density, long lifespan, safety at wide range of temperatures, non-toxicity and low cost. The energy source of portable electronic devices and electrical vehicles are mainly provided by lithium-ion batteries, and the capacity of batteries largely relies on the intrinsic and extrinsic properties of electrode materials. Specifically, lithium-ion batteries with high-voltage and high-capacity cathodes as well as low-voltage and high-capacity anodes are pursued for energy storage and transportation.[194]

With the increasing demand for high energy density batteries in transportation and energy

storage, there is a growing interest in developing cathode materials with higher capacities and higher operating potentials. Based on the intention to lower the cost, consideration of environmental friendliness and safety concerns during the charging/discharging process, $LiMn_2O_4$ and $LiFePO_4$ cathodes have become intriguing choices as the replacement of $LiCoO_2$ cathodes. However, both $LiMn_2O_4$ and $LiFePO_4$ cathodes are suffered from the limited energy capacities and unfavorable reactions on the cathode surface. Coating the cathode surface with a protective layer to suppress the continuous formation of thick SEI layer and composite with other carbonaceous materials can be feasible methods to address the current issues of cathode materials in lithium-ion batteries.

Nowadays, the high-capacity anodes of lithium-ion batteries are focused on the design and construct of alloy materials. Although alloy materials have appealing properties of extremely high theoretical capacities, high volumetric capacities with considerable compacted densities and relatively low discharge potentials, the detrimental volume change that leads to pulverization of active alloy particles and drastic capacity decay during the lithium ions intercalation/extraction process has been an obstacle of the practical application of alloy anodes. Size control and surface modification of alloy particles can be possible approaches to enhance the electrical conductivity of alloy anodes, but this method cannot tackle with the huge volume expansion of the anodes. Therefore, design and construct of alloy composites with unique nanostructure to alleviate the volume expansion, cushion the mechanical stress, deliver high power densities and improve the cycling stability have been major challenges for anodes of lithium-ion batteries.

Another problem of lithium-ion batteries is the increasing price of raw materials due to the

limited reserve of lithium on earth. Reducing production costs while ensuring the high energy density has become a major challenge for next-generation lithium-ion batteries.

1.5 Sodium-ion batteries

The market of portable electronic devices has been dominated by lithium-ion batteries for decades. Although lithium-ion batteries possess the advantages of high energy densities, remarkable cycling stability and lightweight designs, the limited reserve of lithium on earth and elevated cost due to the insufficient supply of raw materials have risen the concerns of seeking complementary energy storage systems. Compared to the limited resources of lithium that illustrated in Figure 1.36, sodium attracts the attention with its abundant reserve in earth's crust.

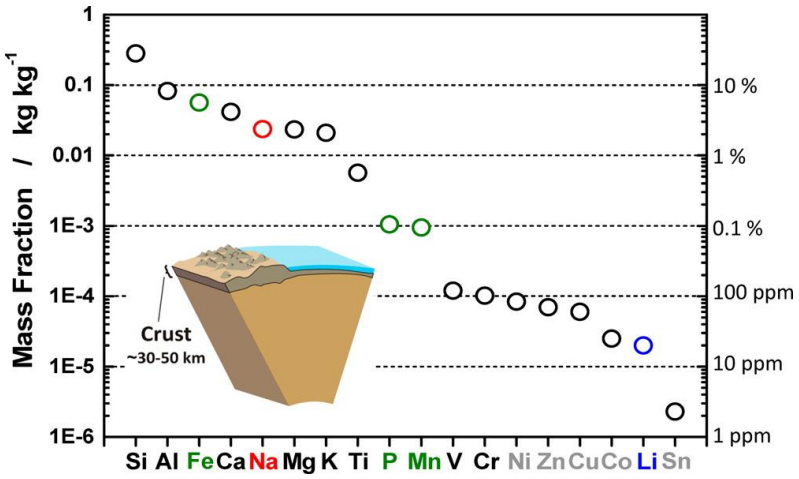

Figure 1.36 Elemental abundance in the Earth's crust.[195]

Due to the wide abundance of sodium, low electrochemical potential (−2.71 V vs the standard hydrogen electrode) which is only 330 mV above that of lithium[196] , high gravimetric

capacity (1165 mA h g^{-1})[197] and analogous intercalation mechanism in electrochemistry, sodium-ion battery (SIB) has been considered as an alternative energy source of lithium-ion battery.

1.5.1 Fundamental of sodium-ion batteries

Similar to the electrochemistry of lithium-ion battery, the fundamental of sodium-ion battery can be classified as intercalation, alloying and conversion.[196] As shown in Figure 1.37, a typical sodium-ion battery is composed by a cathode, an anode, ionic conductive electrolyte and a separator that isolates the cathode and anode.

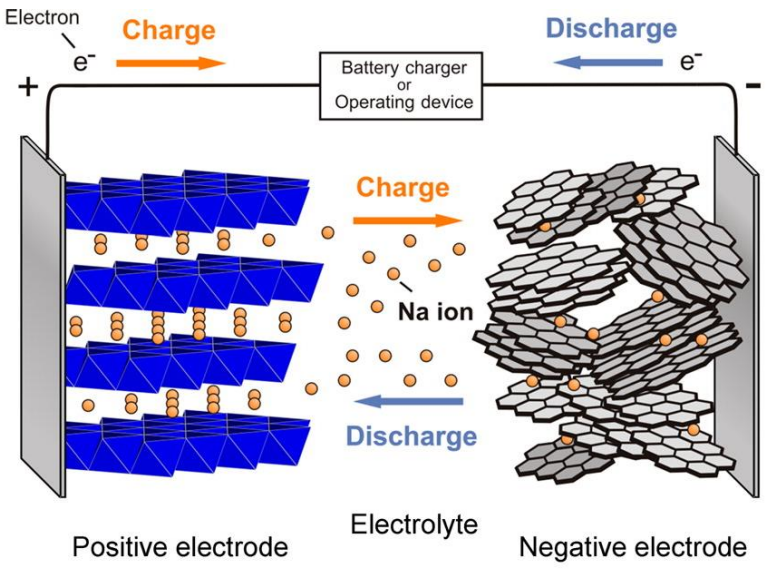

Figure 1.37 Schematic illustration of sodium-ion batteries.[195]

During the charging process, sodium ions are extracted from the cathode side and intercalated into the anode. The process will be in reverse direction when the battery is discharging. The reverse reactions that happened on the electrodes are below, and M represents

the electrode active material:

$$xNa^+ + M + xe^- \leftrightarrow Na_xM$$

Compared to lithium ions, sodium ions have the larger radius size that leads to greater mechanical stress and volume change during the insertion/extraction process. As a result, the electrode materials for sodium-ion batteries need to have enough space to accommodate sodium ions as well as sustain huge volume expansion without cracking of active particles or change of morphology.

1.5.2 Anode materials of sodium-ion batteries

In parallel to the anode materials that are widely applied in lithium-ion batteries, the typical anode materials of sodium-ion batteries can be classified as carbonaceous materials, alloys and metal oxides.

1.5.2.1 Carbon-based materials

As the most successful commercialized anode in lithium-ion batteries, graphite is not suitable for sodium-ion batteries due to the insufficient interlayer space for sodium ions insertion. Graphite only has an interlayer distance of 0.34 nm that is smaller than the minimum distance of 0.37 nm for sodium ions to be inserted.[198] In order to solve the problem of small interlayer space, Wen reported an expanded graphite with an interlayer distance of 0.43 nm to accommodate sodium ions, the anode can deliver a reversible capacity of 284 mA h g^{-1} which

is 8 times of the theoretical capacity of graphite in SIBs (35 mA h g^{-1})[199] with a capacity retention of 73.92% for 2000 cycles.[200] Similar methods to enlarge the interlayer space of graphite to accommodate sodium ions have been reported.[201-203]

Hard carbon has been widely applied in sodium-ion batteries due to its highly disordered structure that can provide large interlayer space for sodium ions insertion. Unlike graphite that can only store sodium ions between the graphitic layers, hard carbon has a versatility in the storage of sodium ions. The intercalation of sodium ions can be held in turbostratic graphitic structure, closed micropores and defects on the surface of hard carbon.[204] However, the utilization of hard carbon anode has been hampered by low initial coulombic efficiency and poor rate capability. Optimizing the surface of electrode with lower defects and constructing interconnected electrically conductive network can be efficient ways to address current issues of hard carbon. Xiao synthesized a hard carbon anode with low defects, and this anode exhibited a high reversible capacity of 361 mA h g^{-1} and excellent cycle stability for 93.4% capacity retention over 100 cycles.[205] Yuan designed a three-dimensional hard carbon anode with interconnected network, this anode deliver a high initial capacity of 341 mA h g^{-1}, outstanding rate capability (210, 128 and 112 mA h g^{-1} at 200, 5000, 8000 mA g^{-1}, respectively) and ultralong lifespan of 3000 cycles.[206]

Graphene has numerous appealing properties including large specific surface area, excellent electrical conductivity, outstanding thermal conductivity and robust mechanical strength. Unfortunately, pure graphene anode can only deliver a low capacity of 105 mA h g^{-1} due to its undersized interlayer space for the intercalation of sodium ions.[207] Therefore, introducing alloys or metal oxide particles to enlarge the interlayer of graphene can be a

feasible way to improve the electrochemical performances of graphene anodes. Yue reported a composite with Sn/SnSb nanoparticles homogeneously dispersed on a nitrogen-doped graphene sheet, the anode delivered a high discharging capacity of 709 mA h g^{-1} at 0.2 A g^{-1}, excellent rate capability (320 mA h g^{-1}, 202 mA h g^{-1} and 119 mA h g^{-1} at 0.6 A g^{-1}, 2 A g^{-1} and 5 A g^{-1}, respectively) and remarkable cycling stability with a capacity of 251 mA h g^{-1} at 1 A g^{-1} for 1000 cycles.[208] The synthesis process is displayed in Figure 1.38. The uniformly dispersed Sn-SnSb nanoparticles can prevent agglomeration of graphene sheets and enlarge the space of intercalation layer for sodium ions. Besides, the flexible graphene can buffer the volume expansion of alloy particles and shorten electrons/ions diffusion distance with its large surface area.

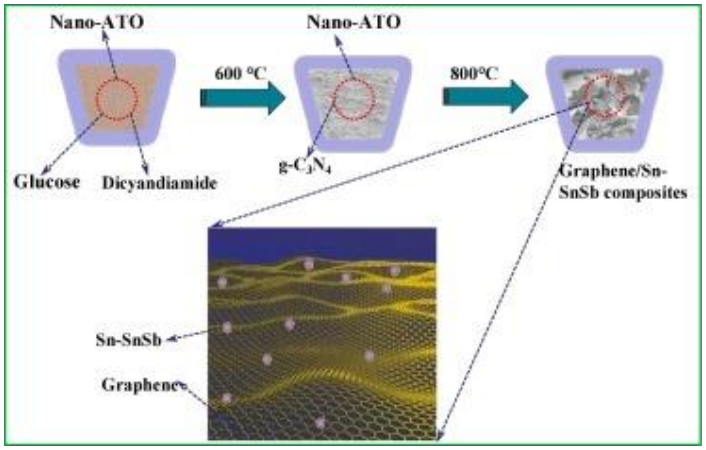

Figure 1.38 Schematic illustration of the preparation procedures for highly dispersed nano Sn-SnSb/G composite.[208]

Liu synthesized a mesoporous Co_3O_4 sheets/3D graphene networks nanohybrid (Co_3O_4 MNSs/3DGNs), and this composite anode exhibited a high initial capacity of 670.5 mA h g^{-1} with a coulombic efficiency of 91%.[209] The morphology of Co_3O_4 MNSs/3DGNs is shown in Figure 1.39. The mesoporous Co_3O_4 sheets can provide extra surface area to insert more

sodium ions and reduce the diffusion distances for electrons/ions transfer to enhance the kinetics of the anode. Moreover, the 3D graphene networks can serve as a buffer for the volume changes of Co_3O_4 to refrain the pulverization of active materials. Besides, the Co_3O_4 nanosheets can prevent the restacking of graphene layers.

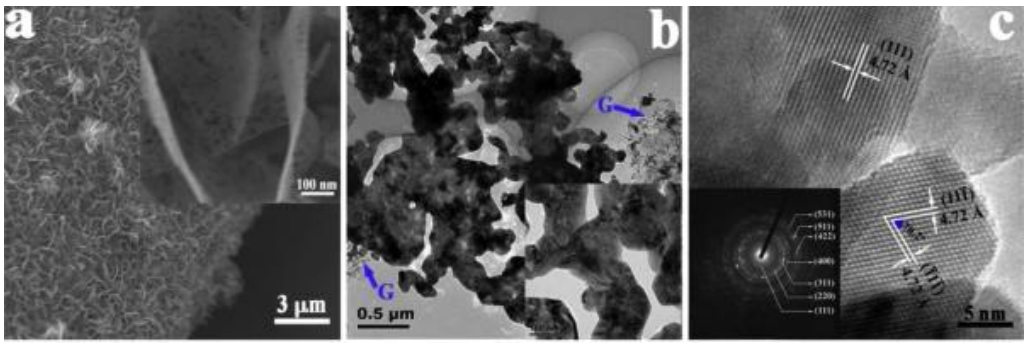

Figure 1.39 (a-c) Structural characterizations of Co_3O_4 MNSs/3DGNs nanohybrids.[209]

1.5.2.2 Alloy-based materials

Silicon anodes that are widely used in lithium-ion batteries are abandoned in sodium-ion batteries since they cannot form reversible alloy reactions with sodium ions. The most common alloy anodes that have been intensively studied in sodium-ion batteries are tin (Sn) and antimony (Sb).

Sn anodes have been regarded as the most promising alloy anode in sodium-ion batteries due to their high theoretical specific capacity of 847 mA h g^{-1} and relatively low discharge potential.[210] However, the huge volume expansion (~420% associated with the formation of $Na_{15}Sn_4$) that leads to fracturing of active Sn particles and loss of contact with electrolyte has impeded the practical application of Sn anodes in sodium storage.[211] For the sake of ameliorating the poor cycling stability and sluggish kinetics due to the pulverization of Sn

anodes, tremendous efforts including design of the electrode structure, composite with carbonaceous materials and construct void space to buffer the volume changes have been made.

Liu encapsulated Sn nanodots into porous nitrogen-doped carbon nanofibers as a free-standing anode for sodium-ion batteries, the Sn NDs@PNC nanofibers exhibited a high reversible capacity of 633 mA h g^{-1} at the current density of 0.2 A g^{-1}, and maintain a capacity of 483 mA h g^{-1} at the current density of 2 A g^{-1} for over 1300 cycles.[212] The synthesis process of Sn NDs@PNC nanofibers is shown in Figure 1.40. The huge volume change and mechanical strain of Sn can be balanced by uniformly distribution of Sn nanodots and carbon nanofibers with integrity and flexibility. Moreover, the interconnected conductive network that linked by porous carbon nanofibers can enhance the transport efficiency of sodium ions and improve the rate capability of the anode. The carbon nanofibers can also function as a current collector to prevent the loss of contacts between Sn nanodots and electrolyte.

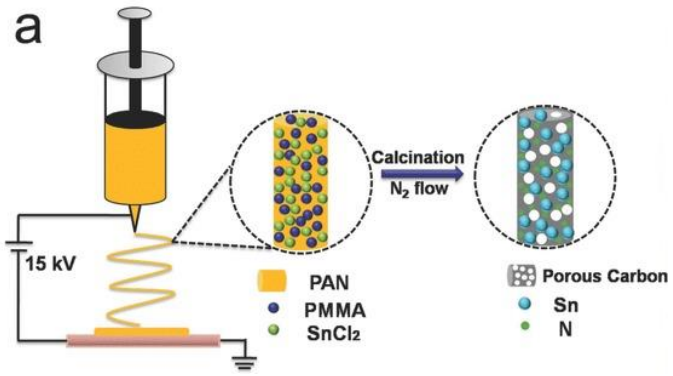

Figure 1.40 Schematic illustration of the preparation process for Sn NDs@PNC nanofibers.[212]

Jeon prepared a porous scaffold reduced graphene oxide as the host for Sn nanoparticles, the anode delivered a high reversible capacity of 615 mA h g^{-1} and stable cycling performance with a 84% capacity retention after 50 cycles.[213] The synthesis steps are shown in Figure 1.41.

The porous graphene scaffold endows enough space for the intercalation of sodium ions as well as provides a three-dimensional conductive network to facilitate the electrons transfer and leads to an improvement in the rate capability of the anode. Furthermore, the porous graphene scaffold can help buffer the volume expansion caused by Sn nanoparticles and avoid the cracking of the electrode.

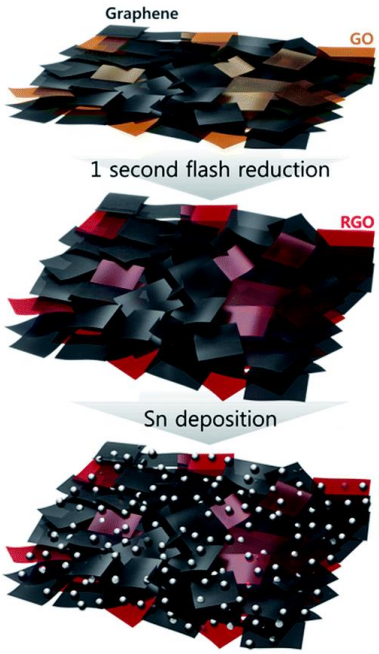

Figure 1.41 Schematic illustration of Sn coated *c*-axis popped graphene fabrication and mechanical property diagram according to the mixing ratio of GO and graphene.[213]

Antimony (Sb) has emerged as an intriguing alloy anode for sodium-ion batteries in recent years. Sb anode possesses a theoretical capacity of 660 mA h g^{-1} associated with the formation of Na_3Sb.[214] Similar to Sn anodes, Sb anodes also suffer from the drastic volume expansion that causes the quick capacity decay only after a few cycles. Since both Sn and Sb anodes are facing the analogous challenges as severe volume changes during the cycling, the approaches to tackle with these issues are in resemblance.

Cui developed a Sb/C composite with Sn nanorods encapsulated into the conductvie N-S codoped carbon (Sb@(N, S–C)), the hybrid anode delivered a high reversible capacity of 621.1 mA h g^{-1} for 150 cycles and an excellent rate capability (534.4, 430.8 and 374.7 mA h g^{-1} at the current density of 2, 5 and 10 A g^{-1}, respectively).[215] The nanostructure and reaction mechanism of Sb@(N, S–C) are illustrated in Figure 1.42. The cross-linked carbon frameworks provide large surface area to adsorb Sb nanorods and decrease the diffusion pathways of ions/electrons transport. Furthermore, the codoped carbon networks can act as a cushion to accommodate the volume expansion of Sb nanorods and enhance the electrical conductivity to ameliorate the rate capability and cycling performance.

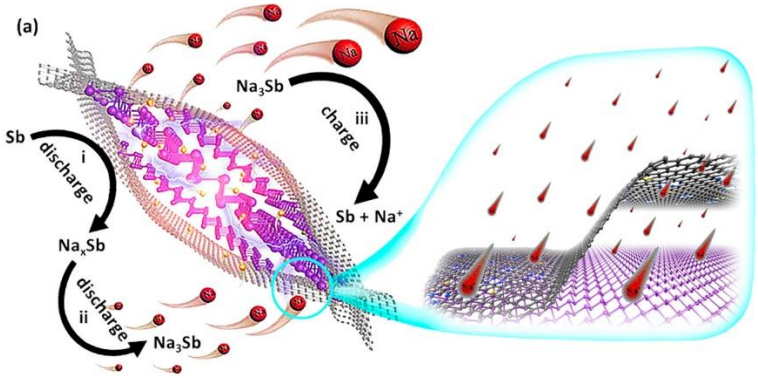

Figure 1.42 Scheme of the reaction mechanism during the charge/discharge process for Sb@(N, S–C).[215]

Luo synthesized a composite with Sb nanoparticles anchored in three-dimensional carbon network (SbNPs@3D-C), the anode exhibited a high reversible capacity of 456 mA h g^{-1} at 0.1 A g^{-1} with a 94.3% capacity retention after 500 cycles, and fabulous rate capability (270 mA h g^{-1} at 2 A g^{-1}).[216] The synthesis steps are shown in Figure 1.43. The three-dimensional carbon network not only buffers the drastic volume changes from Sb nanoparticles during the insertion/extraction of sodium ions, but also provides conductive channels for electrons/ions

transport. The uniform distribution of Sb nanoparticles can also help enhance the electrical conductivity and prevent agglomeration of active particles.

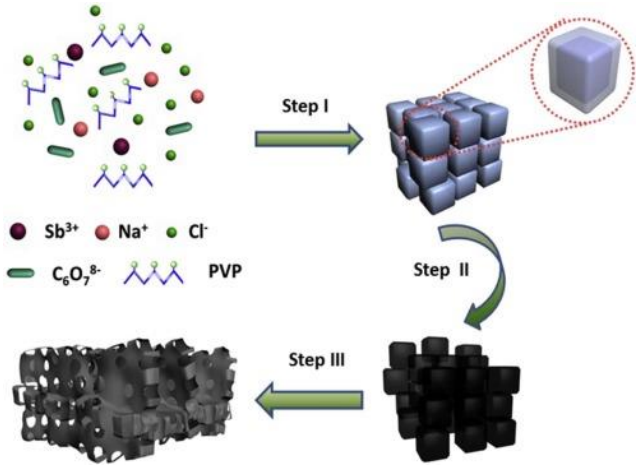

Figure 1.43 Synthesis procedure of SbNPs@3D-C. Step I: freeze drying; step II: carbonization; step III: template removal.[216]

1.5.2.3 Phosphorus-based materials

As a possible anode candidate for sodium-ion batteries, phosphorus (P) can deliver a particularly high theoretical capacity of 2596 mA h g^{-1} when it forms Na_3P compound.[217] Red P, white P and black P are three allotropes of phosphorus. Since white P has safety hazard and red P is electronically insulate, black P is investigated as the electrode for energy storage. Although black P has a high theoretical capacity, the practical application of phosphorus has been dampened by low electrical conductivity ($\sim 10^{-14}$ S cm^{-1})[218] and detrimental volume expansion (up to 500%)[219] that leads to a sharp decline of the capacity and unsatisfied cycling stability.

Tin phosphide (Sn_4P_3) aroused the attention in energy storage since it integrates the high electrical conductivity from Sn and high theoretical capacity from P. Sn_4P_3 possesses a high

theoretical capacity of 1132 mA h g^{-1}, decent electrical conductivity of 30.7 S cm^{-1} and dendrite-preventive redox potential of 0.3V (*vs.* Na/Na^{+}).[220] The only drawback that is still remained is the huge volume expansion of active materials during the cycling. To tackle with the issues of Sn_4P_3 anodes, several strategies have been applied. Ran fabricated a composite with Sn_4P_3 nanoparticles grown on the surface of a porous stem-like carbon nanotube (Sn_4P_3@CNT/C), the hybrid anode delivered a high capacity of 742 mA h g^{-1} at 0.2C for 150 cycles and superb rate capability for a capacity of 449 mA h g^{-1} at 2C for 500 cycles.[221] The morphology of Sn_4P_3@CNT/C is illustrated in Figure 1.44. The porous stem-like CNT acts as a buffer of the severe volume changes from Sn_4P_3 nanoparticles, as well as an electron expressway to facilitate the rate capability of the composite. Furthermore, the fructus-like Sn_4P_3 nanoparticles on the surface of CNT can expose more active sites for sodium ions to react.

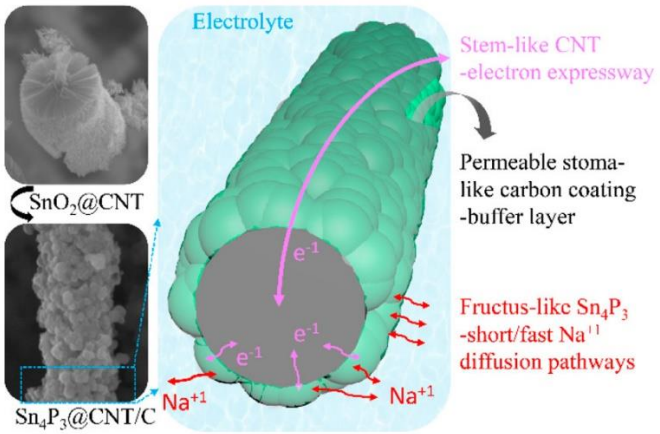

Figure 1.44 Schematic illustration of the transport mechanism of Sn_4P_3@CNT/C.[221]

Liu synthesized uniform yolk-shell Sn_4P_3@C nanospheres, and the composite displayed a high reversible capacity of 790 mA h g^{-1} and excellent cycling stability that can retain a

capacity of 360 mA h g^{-1} at 1.5C for 400 cycles.[222] The synthesis procedure of Sn_4P_3@C nanospheres is demonstrated in Figure 1.45. The carbon shell can provide a void space for the volume expansion of Sn_4P_3 nanoparticles and lead to a uniform and stable growth of SEI layer for the anode to improve the cycling stability. Moreover, the carbon shell can function as the conductor for ions and electrons to increase the transport efficiency of the anode.

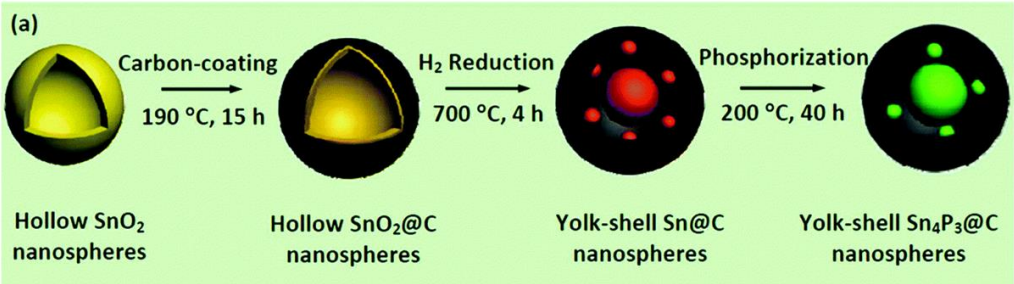

Figure 1.45 Schematic illustration of the fabrication of uniform yolk–shell Sn_4P_3@C nanosphere anodes.[222]

Ran encapsulated Sn_4P_3 nanoparticles into a porous carbon nanofiber as a self-supported anode, the composite showed a high reversible capacity of 712 mA h g^{-1} with 99% coulombic efficiency for 200 cycles and excellent cycling stability that can maintain a capacity of 336 mA h g^{-1} even after 500 cycles.[223] The fabrication of Sn_4P_3@CNF is shown in Figure 1.46. The porous carbon nanofiber with large surface area can provide intimate contact between Sn_4P_3 nanoparticles and electrolyte to promote the electrons and ions transport. The inner space of carbon nanofiber can confine the growth of Sn_4P_3 nanoparticles and mitigate the volume expansion of the anode.

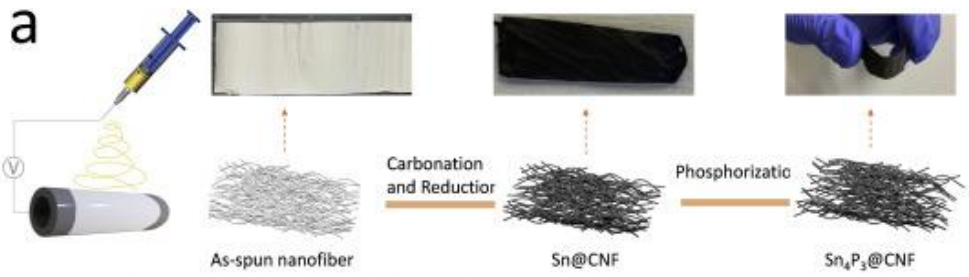

Figure 1.46 Schematic illustration of the fabrication of Sn_4P_3@CNF.[223]

1.5.2.4 Metal oxides and sulfides

Transition metal oxides such as TiO_2, Fe_2O_3, Co_3O_4 have been investigated as the anode candidates for sodium-ion batteries due to their high energy densities, low cost and environmental benignity. Unfortunately, the commercialization of metal oxide anodes has been hampered by low initial coulombic efficiency, sluggish kinetics and poor cycling stability.[224] To solve the problems of metal oxide anodes, composite with conductive materials to enhance the rate performance may be a feasible way. Oh coated a carbon layer on TiO_2 microsphere to deliver a high discharge capacity 155 mA h g^{-1} at 0.1 *C* with 100% capacity retention for 50 cycles.[225] Li reported a composite of Fe_2O_3 nanoparticles with graphene nanosheets that exhibited a specific capacity of 440 mA h g^{-1} with 81.2% coulombic efficiency.[226] Xu confined Co_3O_4 nanoparticles into rambutan-like hybrid hollow spheres of carbon to exhibit an ultra-high capacity of 712 mA h g^{-1} with 74.5% capacity retention after 500 cycles.[227] Metal sulfides such as MoS_2, CuS, Bi_2S_3 [228]and Co_9S_8 also have been studied as the anode materials for sodium-ion batteries.[229-231]

1.5.3 Cathode materials of sodium-ion batteries

The most common cathode materials in sodium-ion batteries can be classified as layered metal oxides and polyanion compounds.

Layered transition metal oxides such as Na_xMO_2 (M can be Fe, Mn, Ti, Co etc.) have been investigated as the cathode materials for sodium-ion batteries due to their high discharge potential, simple crystalline structure and facile synthesis that are favorable for large-scale production. However, layered metal oxide cathodes usually suffer from a series of phase transitions that caused by the extraction of sodium ions, and this will lead to structural collapse and rapid capacity decay of the anodes.[232] To mitigate the drawbacks of layered metal oxide cathodes, solutions including limit the cutoff voltage to avoid the phase change and composite with different types of metal oxides have been attempted. Han reported a Ca-doped Na_xCoO_2 cathode that exhibited a specific capacity of 110 mA h g^{-1} with a negligible capacity decay (0.07 mA h g^{-1} $cycle^{-1}$) for 60 cycles.[233] Zhuang coated a carbon layer on $NaFeO_2$ cathode to deliver a high reversible specific capacity of 89.6 mA h g^{-1} at 0.1C with 87.3% capacity retention after 100 cycles.[234] Billaud reported a β-$NaMnO_2$ with a high capacity of 190 mA h g^{-1} at a rate of C/20 and a good capacity retention for 100 mA h g^{-1} after 100 cycles.[235]

Polyanion compounds with the unit of $(SO_4)^{2-}$, $(PO_4)^{3-}$, $(BO_3)^{3-}$ and $(SiO_4)^{4-}$ have been explored as cathode candidates for sodium-ion batteries, since they can raise the redox potential largely and enhance the safety with a higher potential.[236] The most representative polyanion compound cathodes are $NaFePO_4$ and $Na_3V_2(PO_4)_3$. $NaFePO_4$ with triphylite structure has a one-dimensional sodium ion transport channel, while $Na_3V_2(PO_4)_3$ possesses a rhombohedral crystalline structure that can accommodate the sodium ions. The wide applications of $NaFePO_4$

and $Na_3V_2(PO_4)_3$ have been impeded by the low electrical conductivity and sluggish kinetics. As a result, the improvement for both cathodes are deserved further research. Ma reported $NaFePO_4$@C loaded on an acid-etched carbon cloth to deliver a high reversible capacity of 142 mA h g^{-1} at 0.1 C.[237] Li fabricated hollow $NaFePO_4$ nanospheres that can exhibit a high specific capacity of 147.8 mA h g^{-1} for 100 cycles with excellent capacity retention.[238] Rui designed a three-dimensional hierarchical $Na_3V_2(PO_4)_3$ hybrid cathode that can maintain a capacity of 91 mA h g^{-1} for 10000 cycles.[239] Saravanan prepared a porous $Na_3V_2(PO_4)_3$/C composite that can have a capacity of 114 mA h g^{-1} with a 92.2% capacity retention at 10 C.[240]

1.5.4 Current challenges of sodium-ion batteries

Sodium-ion battery is not a complete substitute for lithium-ion battery, but a complementary battery system in energy storage. Compared to lithium-ion battery, the competitive point for sodium-ion battery lies in its abundant reserve for raw materials, and the production cost is cheaper than lithium-ion battery while achieving the same capacity. Therefore, design and construct of high-capacity electrode materials with low-cost have become the key challenge in the commercialization of sodium-ion batteries.

The most apparent problems for cathode materials in sodium-ion batteries are the low electrical conductivity from the intrinsic properties of cathodes and sluggish kinetics that caused by a series of complicated phase transitions of their crystalline structures. Several approaches including modification of the electrode surface, composite with different types of metal oxide or carbonaceous materials to improve the electrical conductivity and rate capability

have been investigated. The application of cathode materials with high operating voltage and high capacity still remained as challenges for further research.

Alloy-based anodes are very promising in sodium-ion batteries due to their high theoretical capacities and relatively low potentials that can ensure a larger range of operating voltage. The obvious capacity degradation that caused by drastic volume changes and huge mechanical strain of active alloy particles during the insertion/extraction process of sodium ions has hindered the development of alloy-based anodes. Composite with carbonaceous materials that have robust mechanical strength to keep the structural integrity and enhance the rate capability by providing intimate contacts between active materials and electrons can be a possible method to ameliorate the drawbacks of alloy anodes.

In comparison with other mature energy storage systems, sodium-ion battery is still regarded as a new-born technology with immeasurable potential, and these challenges are expected to be solve in the future research.

Chapter 2 Objective of this dissertation

The objective of this dissertation is to develop high-capacity graphene-alloy composite anodes to address the structural fracture, huge capacity degradation and sluggish kinetics caused by alloy anodes in lithium-ion batteries and sodium-ion batteries, as well as open up a new avenue for the design and construct of anode materials for energy storage. This dissertation is mainly focused on the characterizations and electrochemical performances of graphene tube/Sn-based composite anodes for lithium and sodium storage.

In order to tackle with the sluggish kinetics of current commercialized graphite anodes, we attempt to design a flower-like nitrogen-doped graphene tube with Sn nanoparticles composite. Such porous composite with hierarchical nanostructure can be applied in lithium-ion batteries to achieve a high reversible capacity and good rate capability with significant improvement compared to pristine Sn anodes.

After the successful attempt of flower-like graphene tube/Sn composite in lithium-ion batteries, we aim to further optimize the composite with an amphiphilic graphene tube that has hydrophobic graphene layer outside and hydrophilic graphene layer inside to confine the growth of Sn nanoparticles inside the tube to resist the mechanical strain from Sn nanoparticles during the cycling. This well-designed double-graphene-tube/Sn composite can exhibit a high gravimetric and volumetric energy density with a remarkable rate capability and ultra-stable

cycling performance in lithium-ion batteries.

Because of the analogous reaction mechanism possessed by alloy anodes between the lithium-ion batteries and sodium-ion batteries, we tried to expand the application of Sn-based composite with amphiphilic graphene tube into the sodium storage. We replaced Sn in the composite with Sn_4P_3 since Sn_4P_3 has a higher theoretical capacity in sodium-ion batteries, and the Sn_4P_3/graphene tube anode endowed a high reversible capacity with superior rate capability and excellent capacity retention after long cycling.

The successful applications of graphene tube/Sn-based composite in lithium-ion and sodium-ion batteries mean that this unique design of structure can have broader versatility in electrode materials with drastic volume change in energy storage.

Chapter 3 High-capacity anodes for lithium-ion batteries based on hierarchical flower-like graphene tube/Sn composites

3.1 Introduction

With the ever-increasing demands for portable electronic devices and environmentally friendly electric vehicles, the development of lithium-ion batteries is explosive in recent decades. As a result, electrode materials with high energy densities have been extensively investigated.

Alloy-based materials are one of the most promising anode candidates in lithium-ion batteries due to their high theoretical capacities that are 2–10 times higher than that of graphite and 4–20 times higher than that of LTO,[159] relatively low discharge potential and safety during the long cycling. Despite many advantages associated with alloy-based materials, they usually suffer from severe volume change occurred in lithium ions intercalation/deintercalation process, and thus result in pulverization of active alloy particles and irreversible capacity degradation in a few cycles.

As a typical alloy material for lithium-ion batteries, Sn can react with 4.4 lithium ions to form $Li_{4.4}Sn$ to deliver a high theoretical capacity of 994 mA h g^{-1} with a huge volume expansion which can reach up to 260% in charging/discharging process. Tremendous efforts have been made to mitigate the volume change of Sn particles, such as size control, surface

coating, active/inactive alloy, void space design and composite with carbonaceous materials. Hybrid nanocomposites based on alloy materials are proposed as the next-generation anodes for lithium-ion batteries due to their extremely high energy densities and stable cycling performance. As the most common composite material, graphene is known for its appealing properties including large specific surface area, excellent electrical conductivity, outstanding thermal conductivity and robust mechanical strength. Graphene-alloy composites can combine the merits from both alloy and composite materials, as well as adapt to various applications with its different kinds of nanostructures, several attempts to synthesize graphene-alloy composites have been reported.[153, 165, 168-169, 171]

Compared to two-dimensional nanostructures that may have the drawbacks of agglomeration of graphene layers and loss of active sites to react with lithium ions, one-dimensional hierarchical graphene-based composites are particularly desirable since the transport of electrons and ions can proceed along one dimension to shorten the diffusion distances and enable fast-charging performance.

Here, we synthesized a hierarchical flower-like graphene tube with dense porous nanostructure and superior conductivity fabricated by chemical vapor deposition. To demonstrate its potential application in lithium-ion batteries, Sn nanoparticles were anchored on hierarchical flower-like graphene tube (Sn/FGT) to form the graphene-alloy composite through facile hydrothermal reactions. The robust flower-like graphene hierarchical tube not only worked as a highly conductive host matrix for enabling efficient ion and electron transportation, but also provided large surface area to accommodate more Sn nanoparticles to improve the electrochemical performances of the electrode.

3.2 Experimental

Synthesis of $MgCO_3•3H_2O$ tube. $MgCl_2•6H_2O$ (0.9744 g, Sigma-Aldrich) and NH_4HCO_3 (0.7584 g, Sigma-Aldrich) was added into deionized water (60 mL) to form a uniform precursor solution of $MgCO_3•3H_2O$. The solution was then transferred into a volumetric flask (100 mL) and diluted with deionized water. Ethanol (25 mL) was added into a round-bottomed flask (250 mL) and stirred at a speed of 450 r min^{-1} in a water bath of 50 ºC. The as-prepared $MgCO_3•3H_2O$ solution (50 mL) was added into the stirring ethanol and kept stirring for 2.5 min. After the stirring, the mixed solution was aged in a water bath of 50 ºC without stirring for 2 h followed by filtered and washed with deionized water and ethanol. The product was dried in oven at 60 ºC for 8 h to obtain $MgCO_3•3H_2O$ tube.

Synthesis of flower-like MgO tube. The as-formed $MgCO_3•3H_2O$ rod (2.0 g) was added into deionized water (60 mL) at 80 ºC followed by stirring and ultrasonic treatment until the $MgCO_3•3H_2O$ tube is uniformly dispersed in the solution. Then, the $MgCO_3•3H_2O$ tube solution was stirred at a speed of 200 r min^{-1} for 15 min in a water bath of 80 ºC. The obtained products were filtered, washed with deionized water and ethanol, then dried in oven at 60 ºC for 8 h. After drying, the $4MgCO_3•Mg(OH)_2•4H_2O$ tube is obtained through the phase inversion of $MgCO_3•3H_2O$ tube. Thereafter, the flower-like MgO tube was produced by calcination of

$4MgCO_3•Mg(OH)_2•4H_2O$ tube at 500 ºC for 4 h with a heating rate of 10 ºC min^{-1}.

Synthesis of hierarchical flower-like graphene tube. The as-prepared flower-like MgO tube was placed in a horizontal quartz tube to develop graphene with chemical vapor deposition (CVD) method. The quartz tube was heated to 900 °C under a flow of Argon (1000.0 mL min^{-1}) and another Argon stream (150.0 mL min^{-1}) flowing through a flask of acetonitrile for 15 min to develop nitrogen-doped graphene coated on the flower-like MgO tube. Finally, the product was etched with hydrochloric acid solution (1 mol L^{-1}) to obtain hierarchical flower-like graphene tube.

Synthesis of hierarchical flower-like graphene tube/Sn composite. $SnCl_4$ (0.015 mmol, Sigma-Aldrich) was added into the as-prepared hierarchical flower-like graphene tube (50 mg) to deposit homogenous SnO_2 nanoparticles on the tube. The final product of flower-like graphene tube/Sn composite was obtained from flower-like graphene tube/SnO_2 composite under a thermal reduction at 650 °C for 6 h with a flow of mixed gas of Argon and hydrogen.

Material characterization. The morphology and structure of the as-prepared products were conducted by field-emission scanning electron microscopy (FESEM, FEI Nova 430), transmission electron microscopy and high-resolution transmission electron microscopy (HRTEM, FEI Titan STEM). Powder X-ray diffraction was performed on Rigaku Miniflex II diffractometer with Cu Kα radiation operated at 30 kV and 15 mA. Raman spectroscopy was measured with Renishaw 2000 System. Thermogravimetric analysis was characterized using Netzsch STA 449 F3 Jupiter.

Electrochemical measurements. The flower-like graphene tube/Sn composites electrode was prepared by mixing 80 wt-% active materials, 10 wt-% acetylene carbon black, 10 wt-% PVDF binder, and an adequate amount of N-methyl-2-pyrrolidone. The slurry was coated onto copper foil and dried in a vacuum oven at 110 °C for 12 h. The electrode was cut into a round shape with a diameter of 1.2 cm circular pieces. To measure the performance, CR2025 type coin cells were assembled using Li metal foil as the counter electrode and 1 M $LiPF_6$ in ethyl carbonate/dimethyl carbonate (1:1 v/v) as electrolyte. The charge-discharge properties were measured using Land Battery Test System (LAND CT2001A) within a voltage window from 0.01 to 2.5 V (versus Li^+/Li) at room temperature. The capacities were calculated according to the total weight of the flower-like graphene tube/Sn composites.

3.3 Results and discussions

The preparation process of hierarchical flower-like graphene tube/Sn composite is illustrated in Figure 3.1. The first step is to prepare precursor $MgCO_3•3H_2O$ with uniform tube structure by precipitation from soluble magnesium salt and bicarbonate salt, then the tube-like $4MgCO_3•Mg(OH)_2•4H_2O$ was obtained from $MgCO_3•3H_2O$ through phase inversion, the flower-like MgO tube template was produced by the calcination of $4MgCO_3•Mg(OH)_2•4H_2O$ tube. Second, the flower-like MgO tube template was moved into a quartz boat to develop nitrogen-doped graphene layer with acetonitrile in CVD process. Third, the MgO template was etched by dilute hydrochloric acid to obtain the hierarchical flower-like graphene tube. The fourth step is a crucial one where the homogeneous SnO_2 nanoparticles were deposited by using $SnCl_4$ and spontaneously encapsulated SnO_2 nanoparticles into flower-like graphene

hierarchical tube matrix. The final step is a thermal reduction that transformed SnO_2 nanoparticles into Sn nanoparticles to obtain the hierarchical flower-like graphene tube/Sn composite.

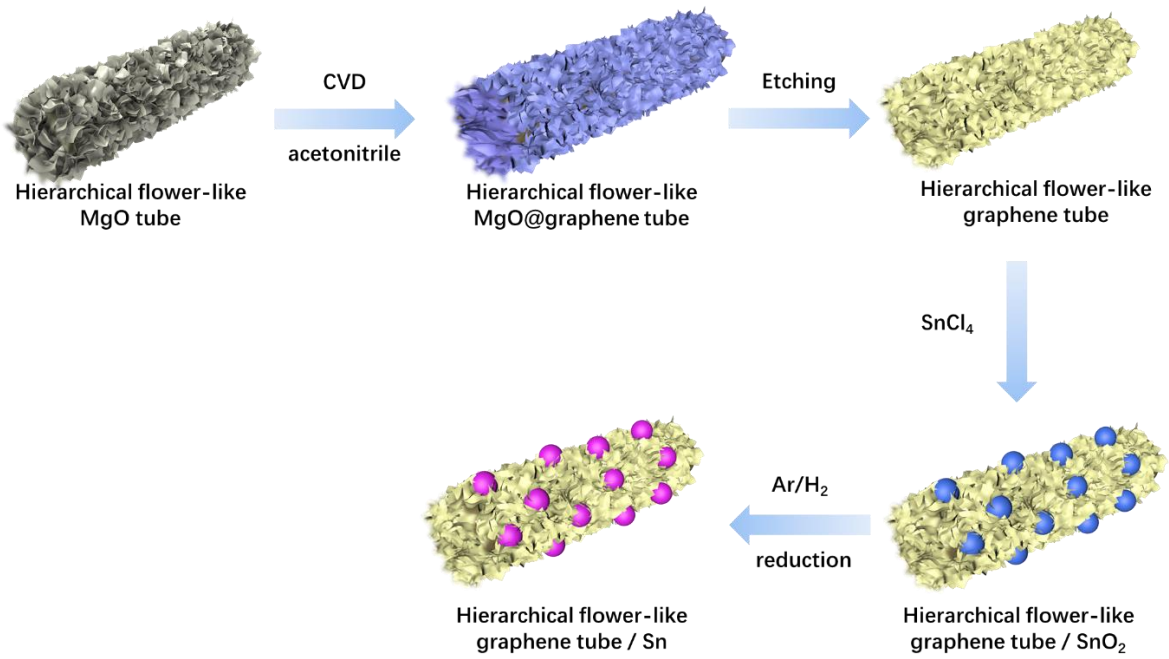

Figure 3.1 A schematic illustrating the synthesis process of hierarchical flower-like graphene tube/Sn composite with chemical vapor deposition and hydrothermal reactions.

3.3.1 Characterization

X-ray diffraction (XRD) patterns of flower-like graphene tube, flower-like MgO@graphene tube and flower-like MgO tube are shown in Figure 3.2(a). The flower-like MgO exhibited two typical patterns with (2 0 0) and (2 2 0) reflections at two-theta 43.1° and 62.5°, respectively. After the nitrogen-doped graphene layer was developed on the surface of MgO template, the typical diffraction peaks of MgO still remained in the flower-like MgO@graphene tube, but the shape of two peaks become sharper as the size of MgO nucleus is increasing under the high temperature atomosphere in CVD process. When the MgO template was etched, the characteristic diffraction peaks for MgO disappeared and only left a

broaden peak at around 25° in the pattern of flower-like graphene tube. This broaden peak is usually recognized as the typical (0 0 2) diffraction peak of graphene.

Figure 3.2 (b) displays the Raman spectra for flower-like graphene tube. The typical D band at 1350 cm^{-1}, G band at 1570 cm^{-1} and 2D band at 2630 cm^{-1} are corresponding to the characteristic spectra of graphene. The presence of D band reflected the defects in the graphene which were attributed to the disorder graphitic layers and nitrogen dope.[168] The observed G band in the curve represented the vibration of sp2-boned carbon atoms in the graphene.[241] The 2D band stands for the high intensity of single layer graphene. The higher relative intensity of G band over D band denotes the high graphitization degree and electrically conductive nature of flower-like graphene tube.

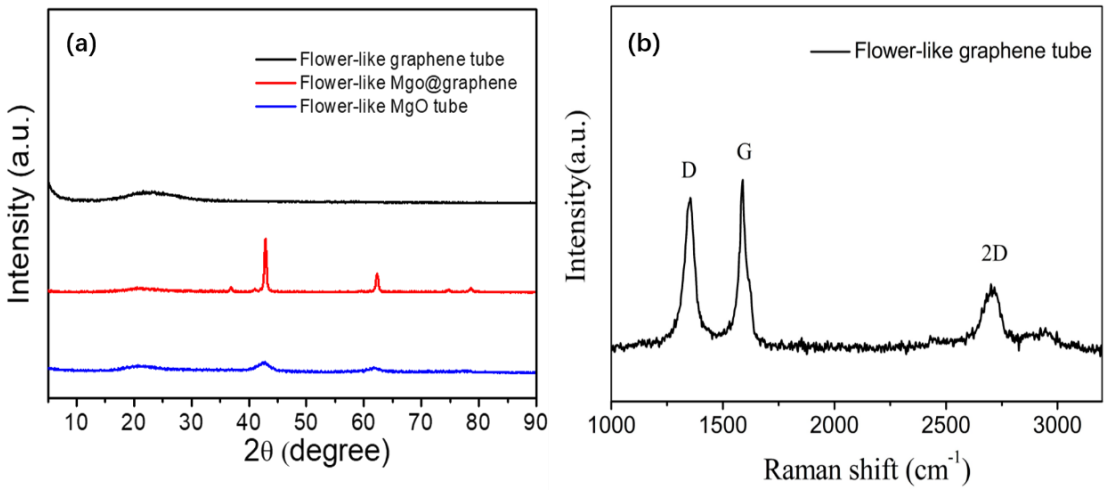

Figure 3.2 (a) XRD patterns of flower-like graphene tube, flower-like MgO@graphene tube and flower-like MgO tube. (b) Raman spectra for flower-like graphene tube.

The morphologies of hierarchical flower-like MgO tube were investigated by scanning electron microscopy (SEM), and the corresponding results are shown in Figure 3.3 (a)-(d). As shown in Figure 3.3 (a), the MgO template showed a rod-like porous morphology. When we zoomed in to focus on the single MgO template in Figure 3.3 (b), it was found that the MgO

template possessed a hierarchical flower-like tube structure with an average diameter of 10 μm. The individual element mapping of magnesium and oxygen on hierarchical flower-like MgO tube were demonstrated in Figure 3.3 (c) (d), the results revealed that magnesium and oxygen were uniform distributed in the flower-like MgO tube.

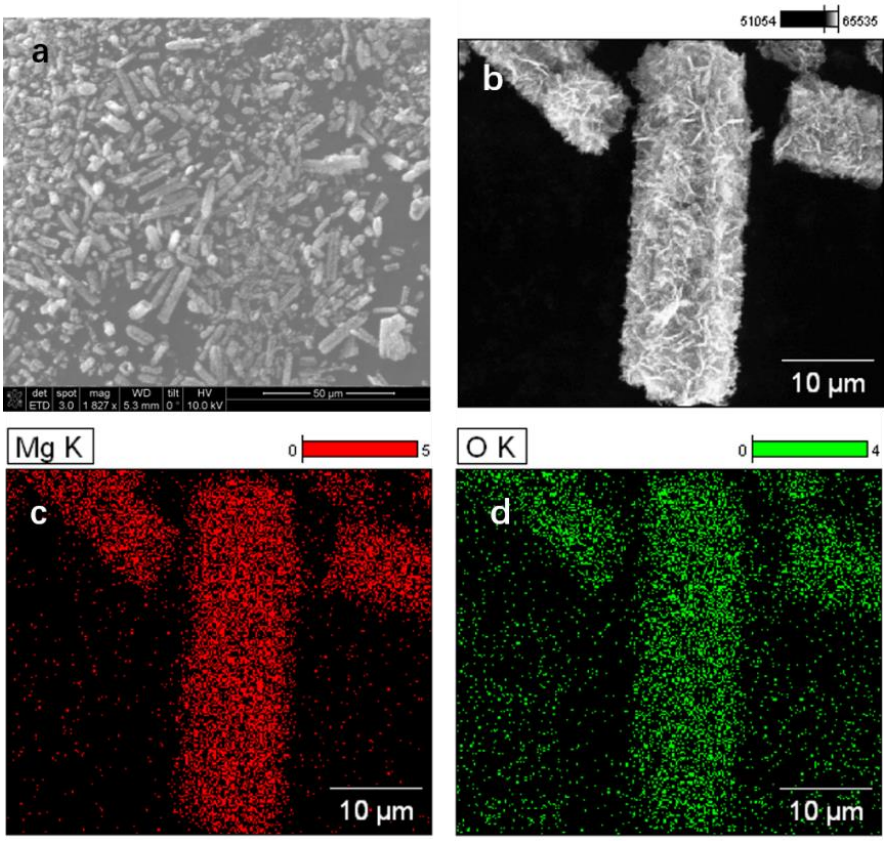

Figure 3.3 Morphology of hierarchical flower-like MgO tube. (a) (b) SEM images of hierarchical flower-like MgO tube; (c) (d) Element mapping of Mg and O of hierarchical flower-like MgO tube, respectively.

The morphologies of hierarchical flower-like MgO@graphene tube were displayed in Figure 3.4 (a)-(f). As shown in Figure 3.4 (a) (b), the porous flower-like tube structure of MgO template was still remained after the nitrogen-doped graphene layer coated on the template, and the average diameter of the hierarchical flower-like MgO@graphene tube was still at the range of 10 μm. The element mapping results from Figure 3.4 (c)-(f) proved that magnesium

oxygen, carbon and nitrogen were uniform dispersed in the flower-like MgO@graphene tube.

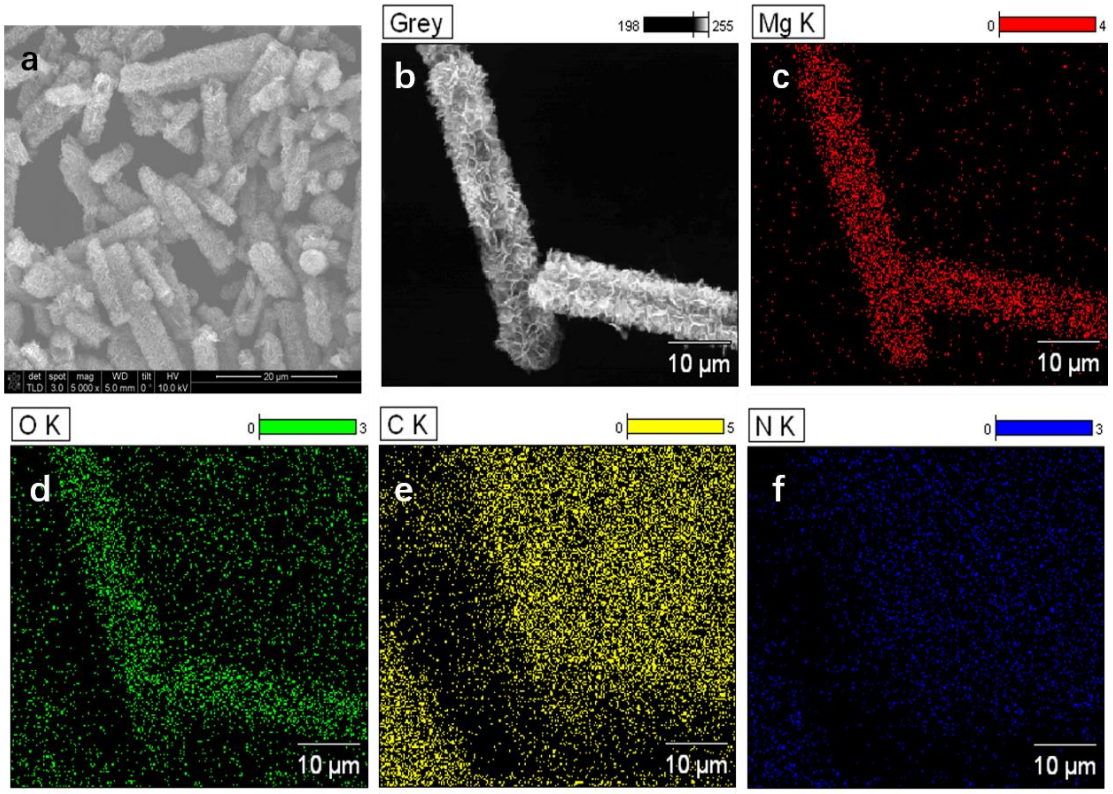

Figure 3.4 Morphology of hierarchical flower-like MgO@graphene tube. (a) (b) SEM images of hierarchical flower-like MgO@graphene tube; (c)-(f) Element mapping of Mg, O, C and N of hierarchical flower-like MgO@graphene tube, respectively.

Figure 3.5 (a)-(d) show the SEM images of flower-like graphene tube, and the hierarchical porous structure of graphene tube retained well even after the removement of the MgO template. The average diameter of the flower-like graphene tube was shrunk to 5 μm and a length at around 20-40 μm. Figure 3.5 (e)-(h) demonstrate the high-resolution transmission electron microscopy (HRTEM) images of flower-like graphene tube. The porous petal nanostructure can be clearly visualized from the HRTEM images shown in Figure 3.5 (f) (g). Figure 3.5 (i) exhibits the selected-area electron diffraction (SAED) of the flower-like graphene tube.

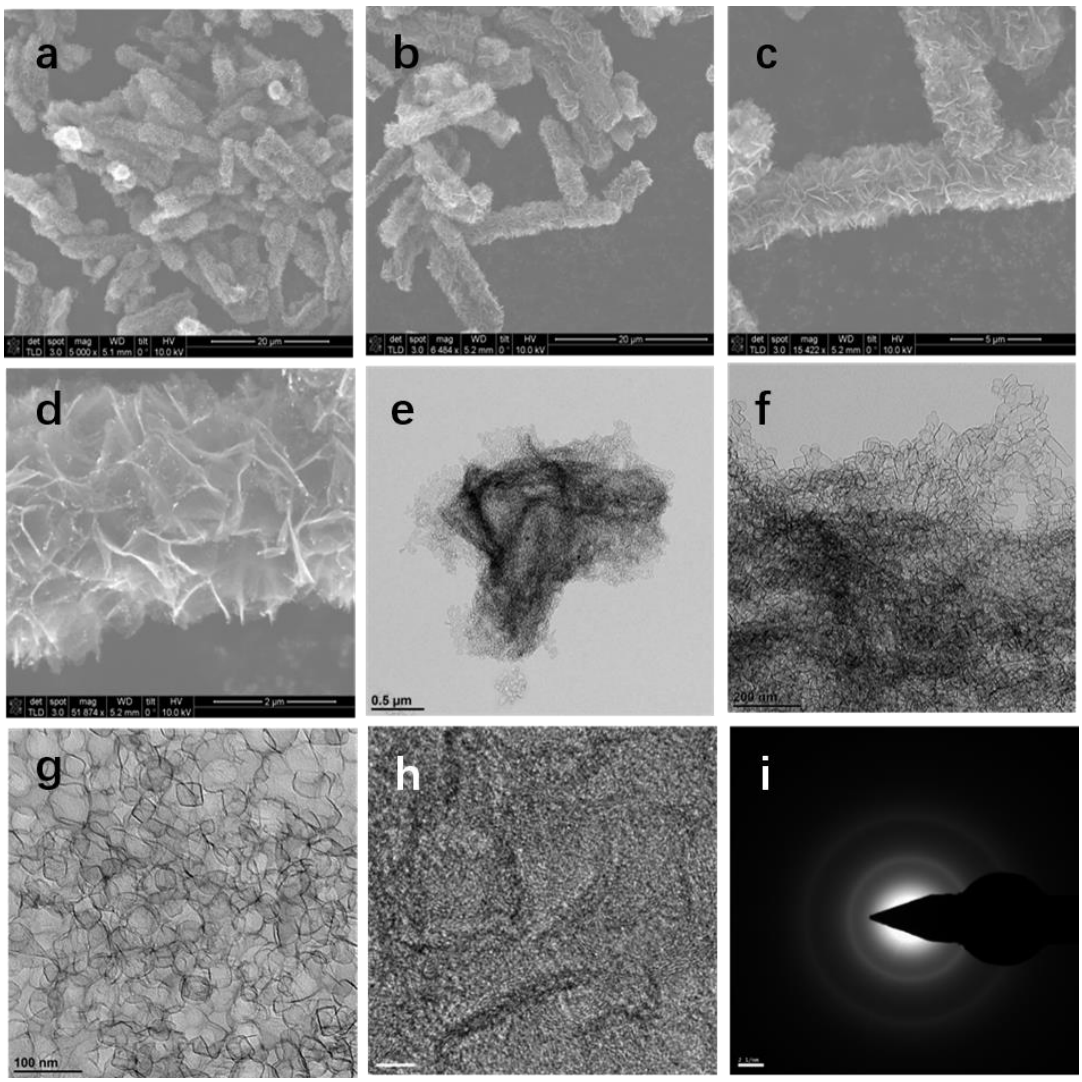

Figure 3.5 Morphology of flower-like graphene hierarchical tube. (a)-(d) SEM images of hierarchical flower-like graphene tube; (e)-(h) High-resolution TEM images of hierarchical flower-like graphene tube; (i) Selective area electronic diffraction of hierarchical flower-like graphene tube.

Figure 3.6 (a) shows the XRD pattern of hierarchical flower-like graphene tube/Sn composite. The well-matched diffraction peaks in the composite are corresponding to the typical XRD pattern of Sn (JCPDS No. 04-0673).[212] The small broaden peak at around 25° is the characteristic diffraction peak of graphene. Figure 3.6 (b) displays the thermogravimetric analysis (TGA) results of hierarchical flower-like graphene tube and hierarchical flower-like graphene tube/Sn composite. The TGA of both materials are tested at 800°C under the air flow.

Since carbon will be completely combusted at 800°C, so there is no weight remained after the test for flower-like graphene tube. For flower-like graphene tube/Sn composite, the weight loss started at 480°C, became rapid at 500°C and leveled off at 600°C. During the heating process, Sn nanoparticles reacted with oxygen to form SnO_2 which were not burned at 800°C, and this conversion led to an increase of the mass from the sample. Meanwhile, graphene was burned completely at 800°C. As a result, the weight drop of the sample is caused by the mass difference between increasing weight from SnO_2 and weight loss from graphene. The mass loading of Sn in the hierarchical flower-like graphene tube/Sn composite can be calculated as 62.53%.

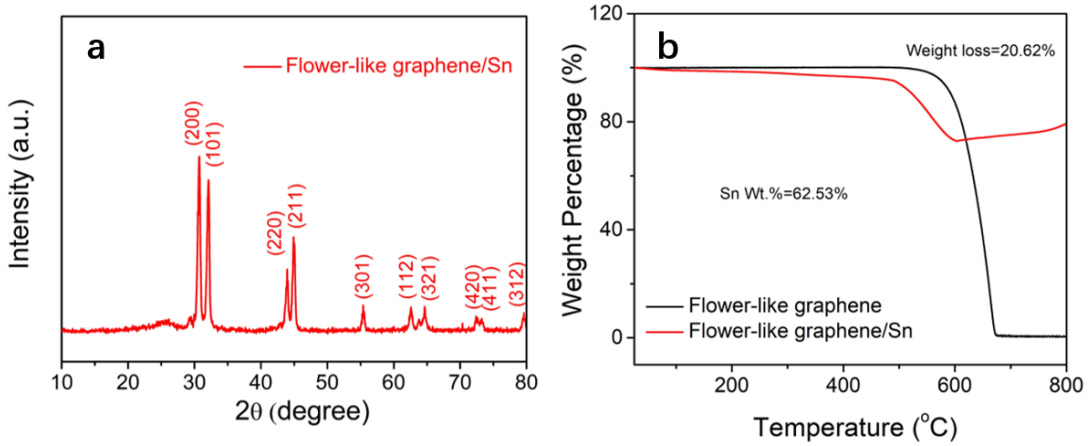

Figure 3.6 (a) XRD pattern of hierarchical flower-like graphene tube/Sn composite; (b) TGA results of hierarchical flower-like graphene tube and hierarchical flower-like graphene tube/Sn composite.

Figure 3.7 (a)-(c) show the SEM images of hierarchical flower-like graphene tube/Sn composite. The average diameter for this composite is at the range of 5 μm. When we zoomed in to focus on the single composite tube in Figure 3.7 (c), it was clearly visualized that Sn nanoparticles are uniformly distributed either on the graphene petal or inside the tube. Figure 3.7 (d) (e) are HRTEM images of the hierarchical flower-like graphene tube/Sn composite which proved that Sn nanoparticles were not only grown on the surface of the graphene tube,

but also embedded inside the graphene tube. Figure 3.7 (f) exhibits the selected-area electron diffraction (SAED) of hierarchical flower-like graphene tube/Sn composite confirming the formation of tetragonal-phase Sn.[212]

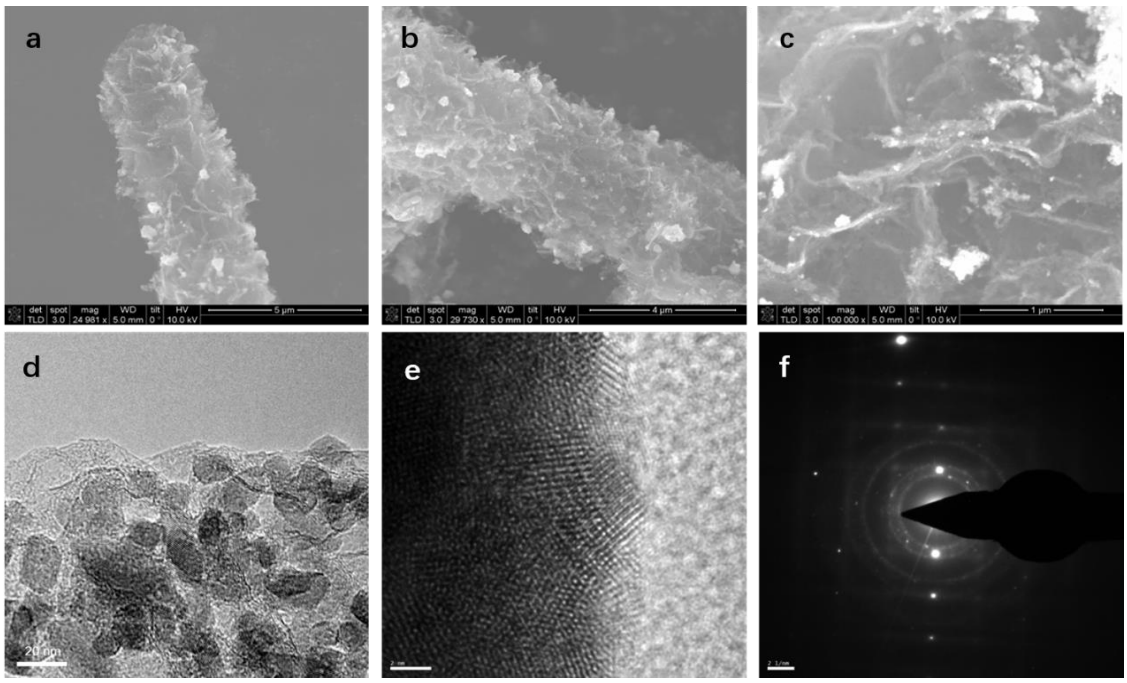

Figure 3.7 Morphology of flower-like graphene hierarchical tube/Sn composite. (a)-(c) SEM images of hierarchical flower-like graphene tube/Sn composite; (d) (e) High-resolution TEM images of hierarchical flower-like graphene tube/Sn composite; (f) Selective area electronic diffraction of hierarchical flower-like graphene tube/Sn composite.

3.3.2 Electrochemical performance

The cyclic voltammetry curves of hierarchical flower-like graphene tube/Sn composite are shown in Figure 3.8. Under a scan rate of 0.2 mV s^{-1}, hierarchical flower-like graphene tube/Sn composite exhibits the anodic peak at 0.62 V which is consistent to the oxidation from $Li_{4.4}Sn$ to LiSn, and the anodic peak at 1.40 V is corresponding to the oxidation from LiSn to Sn. The cathodic peaks of hierarchical flower-like graphene tube/Sn composite at around 0.05 V and 0.8 V can be explained as the reduction of Sn to LiSn and the reaction of $Sn+4.4Li^{+}+4.4e^{-}\rightarrow$

$Li_{4.4}Sn$, respectively. The peak shift from the first cycle to second cycle is mainly caused by the formation of SEI layer and partial irreversibility of lithium oxide (Li_2O) formation.[242]

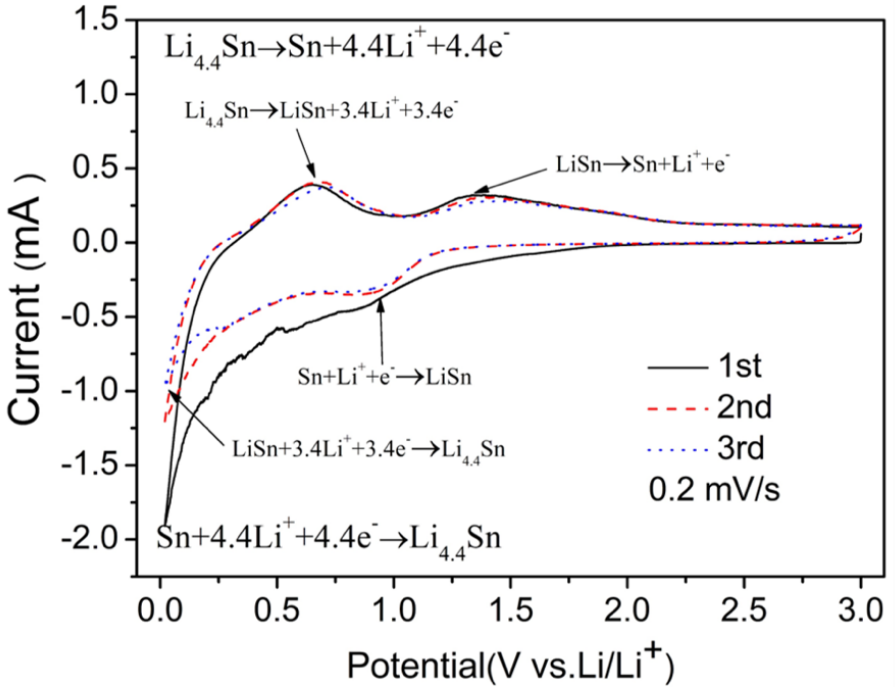

Figure 3.8 Cyclic voltammetry curves of hierarchical flower-like graphene/Sn composite.

Figure 3.9 illustrates the capacity of flower-like graphene tube/Sn composite at 1st, 2nd, 10th, 100th and 200th cycle. The initial capacity of the composite can reach as high as 1550 mA h g^{-1}, and then drops to 880 mA h g^{-1} at the second cycle. The irreversible capacity degradation between the first and second cycle is attributed to the formation of SEI layer. The cycling performance of the composite is very stable with a capacity maintained at 810 mA h g^{-1} at the current density of 0.2 A g^{-1}. In addition, the very well overlapped charging/discharging curves from 10th cycle to 200th cycle verify the excellent cycling stability of hierarchical flower-like graphene tube/Sn composite anode.

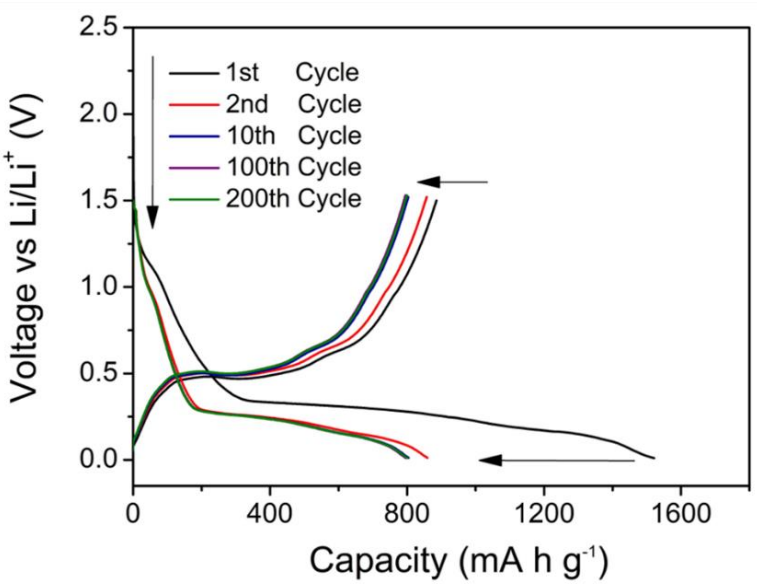

Figure 3.9 Charge/discharge profiles of hierarchical flower-like graphene/Sn composite.

The cycling performance of hierarchical flower-like graphene tube/Sn composite is shown in Figure 3.10 (a). The composite anode exhibits a high specific capacity of 742 mA h g^{-1} with a Coulombic efficiency maintained at 99% for 200 cycles. Rate capabilities and discharging capacities of hierarchical flower-like graphene tube/Sn composite are displayed in Figure 3.10 (b). The capacities of the composite exhibit as 812 mA h g^{-1}, 761 mA h g^{-1}, 715 mA h g^{-1}, 603 mA h g^{-1} and 409 mA h g^{-1} under the current density of 0.2 A g^{-1}, 0.5 A g^{-1}, 1.0 A g^{-1}, 2.0 A g^{-1} and 5.0 A g^{-1}, respectively. Even at an extremely high current density of 8 A g^{-1}, the composite can still deliver a capacity of 211 mA h g^{-1}. Remarkably, the capacity of the composite can recover to the initial capacity at 0.2 A g^{-1} after cycling at high current densities.

The excellent rate capability and good cycling stability of the composite are ascribed to the porous flower-like graphene tube that can cover a certain amount of Sn nanoparticles with petals to prevent Sn nanoparticles from detachment caused by the severe volume expansion. Furthermore, the flower-like graphene tube provides a large specific surface area that can

expose active Sn nanoparticles to the electrolyte, and shorten the diffusion pathways for the ions and electrons to facilitate the rate capability of the composite. In addition, the intrinsic high electrical conductivity from graphene also has a positive effect on the electrochemical performances of the anode.

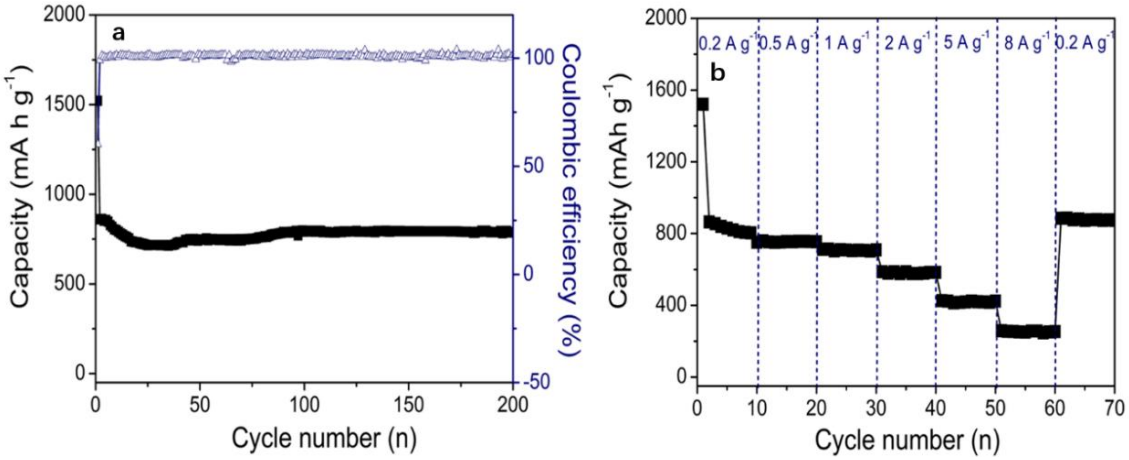

Figure 3.10 (a) Cycling performance of hierarchical flower-like graphene tube/Sn composite. (b) Rate capabilities of hierarchical flower-like graphene tube/Sn composite. Electrochemical performances of the flower-like graphene/Sn composites.

3.4 Conclusion

The synthesized hierarchical flower-like graphene tube/Sn composite with high reversible capacity of 742 mA h g^{-1}, excellent rate capability (211 mA h g^{-1} at 8 A g^{-1} with 99% capacity retention when the current density is back to 0.2 A g^{-1}) and long cycle life without structural damage is regarded as a desirable anode material in lithium-ion batteries. The hierarchical flower-like tube structure enables fast charge transfer with shortened diffusion distances, and provides large surface area to accommodate volume change of Sn nanoparticles during the cycling. We hope this work can inspire more ideas on the design and construct of alloy-based composites for lithium-ion batteries with high capacities and stable cycling performances.

Chapter 4 Tin-graphene tubes as anodes for lithium-ion batteries with high volumetric and gravimetric energy densities

4.1 Introduction

There are increasing demands for lithium-ion batteries (LIBs) with high gravimetric energy; meanwhile, due to the limited space that are available to accommodate the batteries in microelectronics and electric vehicles, developing LIBs with high volumetric energy density is also emerging as a particularly important theme.[243-246] The current LIBs generally adapt graphite as the anode material and lithium-nickel-manganese-cobalt oxides (NMC) as the cathode materials. Graphite has a theoretical gravimetric capacity of 372 mA h g^{-1} (based un-lithiated graphite), crystal density of 2.266 g cm^{-3}, and volumetric capacity of 841 mA h cm^{-3} (based on un-lithiated graphite)[247] or 719 mA h cm^{-3} (based on full-lithiation graphite).[248] Whereas the commercially used graphite generally has a low tap density (e.g., 1.1 g cm^{-3}), which occupies a significant portion of a battery volume.[249] For example, when paired with commercial cathode materials (e.g., NMC111, NMC523, NMC622, and NCM811), the graphite coatings could account for 55–60% of the volume of a cell, including the anode and cathode coatings, current collector, and separator.[250-252] Exploring novel anode materials that can reduce the volume of the anode coatings occupied, in this context, is of paramount importance towards LIBs with significantly improved volumetric energy density.

Among the vast library of anode materials, metals and metal oxides generally exhibit significantly higher volumetric capacities than the carbonaceous materials owning to their high gravimetric capacity and tap density.[253-256] For example, tin (Sn) has a theoretical volumetric capacity of 7316 mA h cm^{-3} (based on un-lithiated Sn)[257-259] or 2111 mA h cm^{-3} (based on full-

lithiation Sn),[248] respectively, which are significantly higher than those of graphite (841 mA h cm^{-3} and 719 mA h cm^{-3}, respectively).[257-258] In addition, Sn is a low-cost material with a low working potential (<0.5 V versus Li/Li^+), making it a highly promising anode candidate with both high volumetric and gravimetric energy density. Nonetheless, Sn exhibits large-volume change during the lithiation and delithiation, which disrupts the electrode structure and electronic conductive networks and results in poor cycling life.[260-261] To address these issues, various Sn, Sn alloys,[262-265] and Sn-based composites with designed structures (e.g., nanowires, nanosheets, and porous structures) have been explored,[266-272] whereas making Sn anodes with high energy density and long cycling life remains challenging.

Herein, we show a design of high-performance Sn anodes, which were made by confining Sn nanoparticles within the frameworks of graphene tubes. This design suggests an effective solution to spontaneously encapsulate Sn nanoparticles into double hydrophilic N-doped graphene/void/hydrophobic graphene tube (Sn/DGT) with control over position, the so-called the incorporation of nanoparticle-in-tube structure and double-shelled architecture. Such the Sn/DGT nanocomposite has multiple advantages: (1) The nanosized Sn particles may effectively alleviate the mechanical stress during the alloying/dealloying process and supply short lithium ion diffusion path for LIBs; (2) Sn nanoparticles are spontaneously encapsulated inside of inner N-doped graphene layer with multipoint physical contacts, greatly improving electrical conductivity of Sn electrode and increasing space utilization ratio; (3) The flexible inner voids and “intershell” spaces may significantly buffer volume changes of Sn electrode during the charging and discharging process; (4) The static outer shell is favorable to form the stable SEI film; (5) The whole graphene tube framework provides the high kinetics of lithium

ion and fast electron and ion diffusion.

4.2 Experimental

Synthesis of MgO tube. An aqueous urea solution (1.2 g in 20 mL deionized water) was dropped into a magnesium acetate solution (12 g in 80 mL deionized water). The mixed solution was stirred for 1h, sealed in a 200 mL Teflon-lined autoclave, and heated at 180 °C for 2 h. As-formed $Mg(OH)_2$ was filtrated, washed with ethanol, dried in vacuum at 100 °C, and calcined at 600 °C for 6 h in air to obtain the MgO nanowire template.

Synthesis of DGT. The MgO template was placed in a horizontal quartz tube to develop graphene with chemical vapor deposition (CVD) method. The quartz tube was heated to 900 °C under a flow of Argon (1000.0 mL min^{-1}) and another Argon stream (150.0 mL min^{-1}) flowing through a flask of acetonitrile for 10 min to develop nitrogen-doped graphene coated on the MgO template. As-formed nitrogen-doped graphene was dispersed in a solution which contains $Mg(NO_3)_2{\cdot}2H_2O$ (0.5 g, Sigma-Aldrich) and urea (0.2 g, Sigma-Aldrich) in deionized water (100 mL) to sonicate for 30 min. After refluxing at 90 °C for 24 h, the mixture was washed and dried at 80 °C overnight. The nitrogen-doped graphene/MgO was coated with graphene under a flow of CH_4 (400.0 mL min^{-1}) and Argon (1000.0 mL min^{-1}) at 1000 °C for 10 min. Finally, the product was etched with hydrochloric acid solution (1 mol L^{-1}) to obtain the double graphene tubes (DGT).

Synthesis of Sn/DGT. DGT (60 mg) was added in deionized water (60 mL) and sonicated for

30 min, in which $K_2SnO_3 \cdot 3H_2O$ (0.5 g, Sigma-Aldrich) was dissolved and stirred for 1 h. The solution was then transferred into a Teflon-lined autoclave (100 mL), which was maintained at 180 °C for 12 h. As-formed samples were obtained by centrifugation and filtration, dried under 80 °C overnight, and annealed at 650 °C in a gas mixture of Argon and hydrogen for 10 h.

Synthesis of Sn/C. The carbon-coated Sn nanoparticles were prepared by the polymerization of dopamine-hydrochloride on commercial Sn particles with a weight ratio of 2:1 (Sn:C), and followed by the carbonization at 750 °C for 6 h.[258]

Material characterization. The morphology and structure of the as-prepared products were conducted by field-emission scanning electron microscopy (FESEM, FEI Nova 430), transmission electron microscopy and high-resolution transmission electron microscopy (HRTEM, FEI Titan STEM). Powder X-ray diffraction was measured on Rigaku Miniflex II diffractometer with Cu Kα radiation operated at 30 kV and 15 mA. Raman spectroscopy was performed with Renishaw 2000 System. The TGA was determined on an SDT Q600 thermoanalyzer under air. In situ TEM was carried out using a FEI Titan microscope operated at 300 kV.

Electrochemical measurements. The samples were mixed with carboxymethyl cellulose (CMC) binder and Super P carbon black to obtain uniform slurry at the weight ratio of 8:1:1. Then the slurries were coated onto copper foil and dried in a vacuum oven under 120 °C for 24 h. The electrodes were cut into a round shape with a diameter of 1.2 cm circular pieces. To measure the performance, CR2025 type coin cells were assembled using Li metal foil as the counter electrode and 1 M $LiPF_6$ in ethyl carbonate/dimethyl carbonate (1:1 v/v) as electrolyte.

The charge-discharge properties were measured using Land Battery Test System (LAND CT2001A) within a voltage window from 0.01 to 2.5 V (versus Li^+/Li) at room temperature. Electrochemical impedance measurement was evaluated in a range of 0.01–10 MHz at 10 mV with perturbation amplitude of 10 mV on the cells at open circuit potential. The capacities were calculated according to the total weight of the composites (Sn and DGT). For the full-cell performance, a commercial lithium-nickel cobalt manganese oxide (NCM622, Tianjin B&M Science and Technology Co., Ltd) was used as the cathode with a fixed areal capacity of 3.2 mA h cm^{-2}. The N/P ratio, defined by total capacity ratio between anode and cathode, was chosen to be 1.0–1.1. The capacities were calculated according to the electrode mass loading, including the binder and carbon black.

4.3 Results and discussions

As illustrated in the Figure 4.1 (a), using magnesium oxide (MgO) as the template and catalyst, we first grew nitrogen-doped graphene around MgO nanowires by chemical vapor deposition (CVD) using acetonitrile as the precursor. As-formed graphene-coated nanowires were then coated with a thin layer of MgO, on which graphene was grown using methane as the precursor. Removal of the templates leads to the formation of double-graphene-tubes (DGT), which consists of an inner hydrophilic graphene tube (nitrogen-doped) and an outer hydrophobic graphene tube (un-doped). Dispersing the DGT in a K_2SnO_3 solution allows the aqueous precursor to infiltrate into the hydrophilic tubes, as well as growth of SnO_2 nanoparticles within the inner tubes in a subsequent hydrothermal reaction. Finally, reducing the SnO_2 nanoparticles leads to the formation of Sn nanoparticles encapsulated within

the double-graphene-tubes, denoted as Sn/DGT.

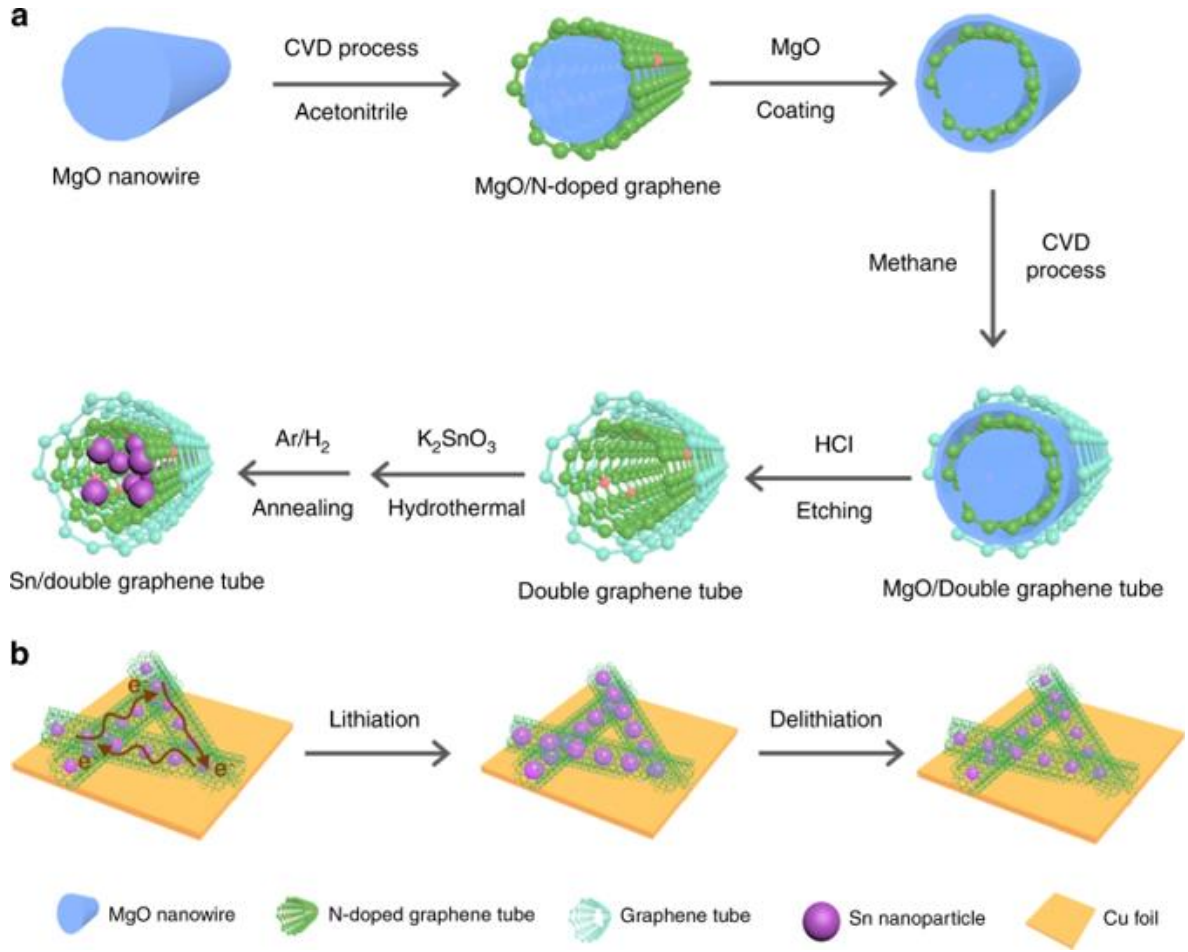

Figure 4.1 (a) A schematic illustration of the synthesis of Sn/DGT composite; (b) A schematic illustration of the lithiation process of a Sn/DGT electrode, during which Sn nanoparticles are retained within the graphene tubes despite their large-volume change, preserving the electron-conduction networks and integrity of the electrode.

As depictured in the Figure 4.1 (b), by confining the Sn nanoparticles within the electronically conductive and mechanically robust DGT, the structural integrity of the electrodes, as well as the electron-conduction networks among the nanoparticles, could be well preserved, despite their large-volume change during the lithiation and delithiation. In addition, the small size of the Sn nanoparticles shortens their ion-diffusion paths and alleviates the mechanical stress during the alloying/dealloying process. Meanwhile, the tubular structure

allows a high loading of Sn nanoparticles, which is critical for high energy density. Note that Sn-carbon composites were also synthesized by infiltrating Sn precursors to carbon scaffolds (e.g., porous carbon particles and carbon fibers) followed by a reduction process.[266-269, 273] In these approaches, it is difficult to assure as-formed Sn particles are confined within the scaffolds, whereas detachment of the Sn particles from the carbon scaffolds could unavoidably result in decay of the capacity.

4.3.1 Characterization

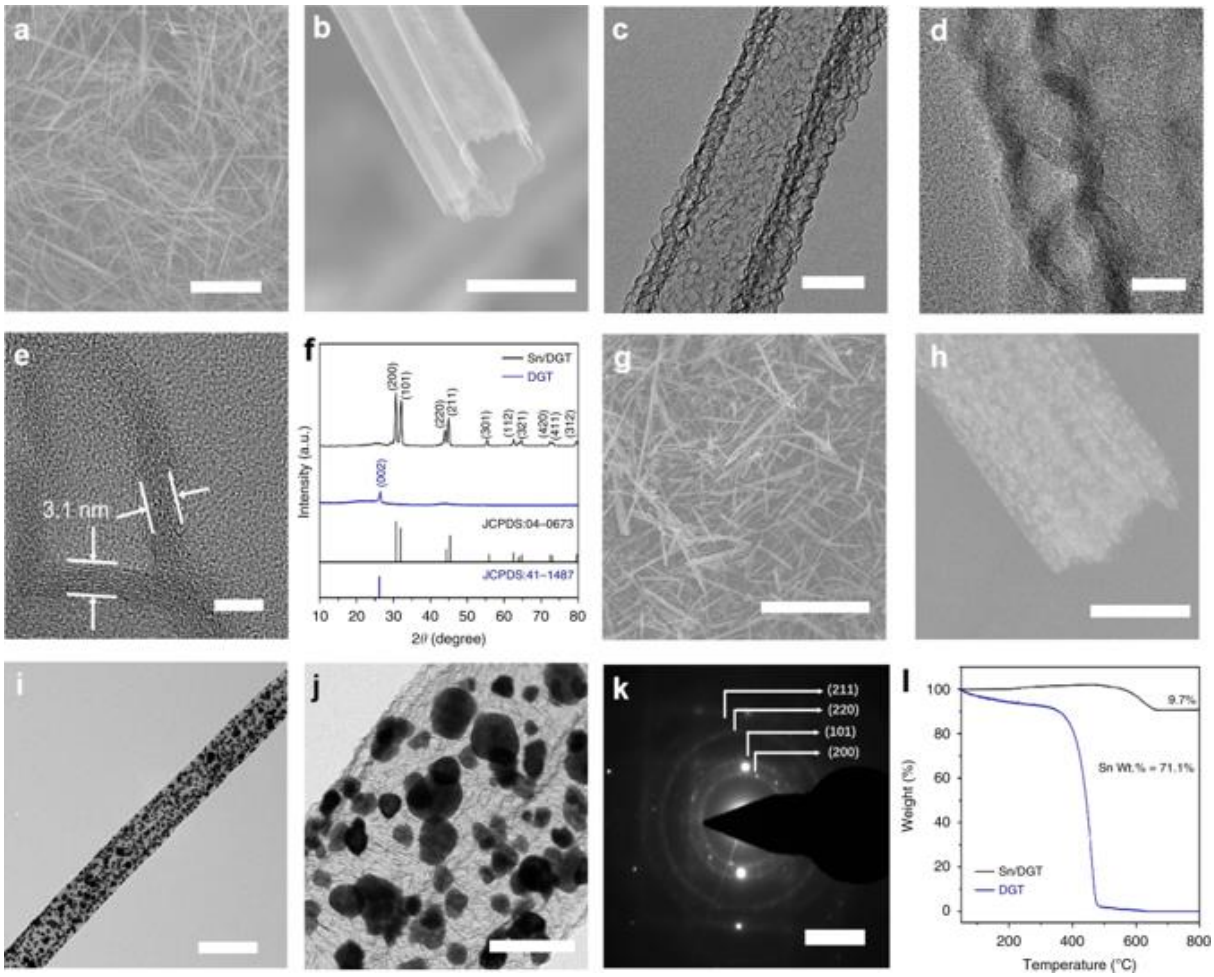

Figure 4.2 Morphology and structure of DGT and Sn/DGT. (a) (b) SEM images of DGT (Scale bars: (a) 10 μm; (b) 500 nm); (c)-(e) TEM images of DGT (Scale bars: (c) 200 nm; (d) 10 nm; (e) 5 nm); (f) XRD patterns of DGT and Sn/DGT; (g) (h) SEM images of Sn/DGT (Scale bars: (g) 10 μm; (h) 200 nm); (i) (j) TEM images of Sn/DGT (Scale

bars: (i) 500 nm; (j) 100 nm); (k) Selective area electronic diffraction of Sn/DGT (Scale bar: (k) 5 1/nm); (l) TGA results of DGT and Sn/DGT.

Figure 4.2 (a)-(d) illustrate the SEM and TEM images of DGT, which show an average diameter of 350 nm and a length between 10 μm and 20 μm in Figure 4.2 (a). The double-tube structure can be clearly visualized from the SEM image shown in Figure 4.2 (b), which is further confirmed by the TEM image in Figure 4.2 (c). The distance between the inner and outer tube is ~10 nm; meanwhile, porous structure in the tube wall can be clearly observed in Figure 4.2 (d), providing pathways for the transport of electrolytes. Figure 4.2 (e) shows a higher-magnification TEM image of DGT, indicating the graphene structure has a tube-wall thickness of 3.1 nm (approximately nine layers of graphene). In addition, chemical mapping results of the graphene tubes from Figure 4.3 confirms the presence of nitrogen, indicating successful nitrogen doping of the inner graphene tubes.

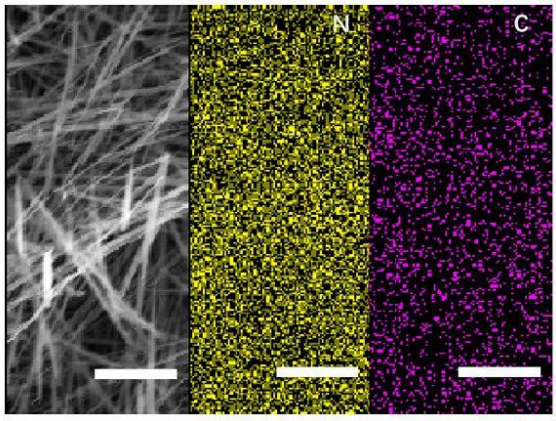

Figure 4.3 EDS elemental maps of C and N (Scale bars: 5 μm).

Figure 4.2 (f) shows the XRD patterns of DGT and Sn/DGT. DGT exhibits the (002) peak at ~26°, Sn/DGT exhibits intense diffractions of tetragonal Sn (JCPDS No. 04-0673),[168, 212] and

no diffraction peaks from the graphene tubes can be observed due to its low content. Raman spectra of Sn/DGT in Figure 4.4 show two peaks centered at 1331 cm^{-1} and 1586 cm^{-1}, attributed from the DGT moiety.[241, 274] Figure 4.2 (g) (h) show the SEM images of Sn/DGT, where Sn nanoparticles are encapsulated within the graphene tubes. TEM image in Figure 4.2 (i) (j) suggest that Sn nanoparticles are uniformly distributed within the DGT with an average diameter of 40 nm. No Sn nanoparticles outside the DGT could be observed.

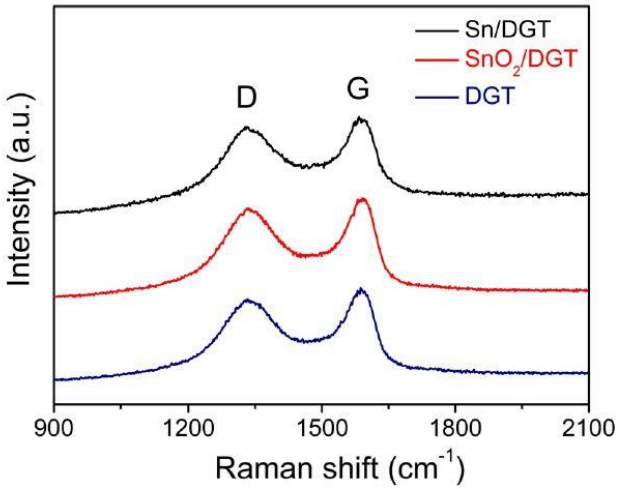

Figure 4.4 Raman spectra of DGT, SnO_2/DGT and Sn/DGT.

As demonstrated in Figure 4.5, the Sn nanoparticles have an interplanar distance of 0.29 nm, attributed to the (200) facet of tetragonal Sn.[168, 212] Figure 4.2 (k) exhibits the selected-area electron diffraction (SAED) of Sn/DGT confirming the formation of tetragonal-phase Sn. Figure 4.2 (l) shows the TGA results of DGT and Sn/DGT measured using an air atmosphere. DGT experiences a major weight loss from 400 to 500 °C due to its oxidation reaction, while the weight of Sn/DGT increases before 500 °C attributed to the oxidation of the Sn nanoparticles. Further increasing the temperature causes oxidation of the DGT moiety, accompanied by a weight loss. The final weight loss of Sn/DGT is around 9.7%, corresponding

to a Sn content of ~71.1 wt%.

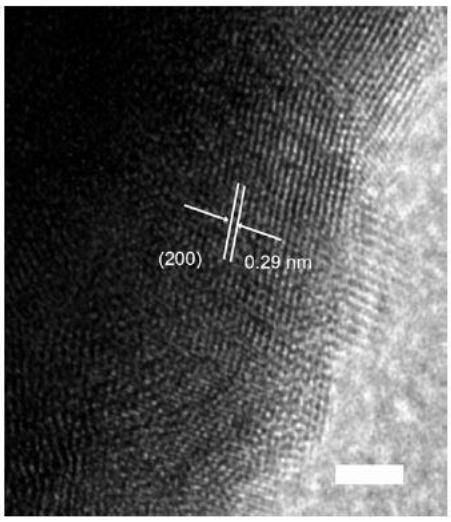

Figure 4.5 High-resolution TEM images of a Sn nanoparticle in Sn/DGT (Scale bar: 2 nm).

Figure 4.6 (a)-(c) show the wetting process of water on nitrogen-doped graphene tubes, while Figure 4.6 (d)-(f) demonstrate the wetting process of water on un-doped graphene tubes. The nitrogen-doped graphene tubes (the inner tubes of DGT) exhibit an initial contact angle of 64.1°, which is rapidly decreased to 0° after 1 s, indicating a hydrophilic surface. In contrast, the un-doped graphene tubes (the outer tubes of DGT) show a stable contact angle of ~128.9°, indicating a hydrophobic surface. Such biphilicity (the co-exitance of hydrophilic and hydrophobic tubes) is critical to ensure the encapsulation of Sn nanoparticles within the DGT and avoid their attachment outside the DGT.

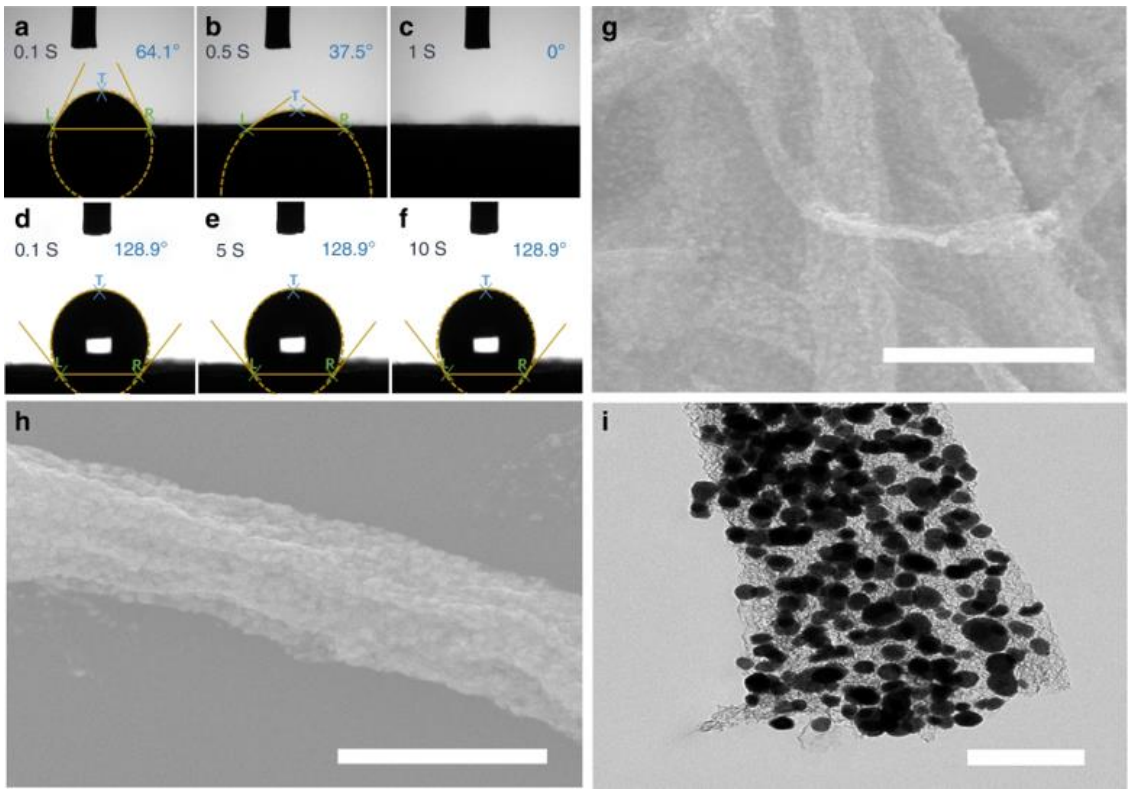

Figure 4.6 (a)-(c) Wetting process of water on nitrogen-doped graphene tubes; (d)-(f) Wetting process of water on un-doped graphene tubes; (g) (h) SEM images of Sn/DGT* (Scale bars: (g) 2 μm; (h) 500 nm); (i) TEM image of Sn/DGT* (Scale bar: 200 nm).

Firstly, the biphilicity of DGT allows the aqueous precursor solution to infiltrate to the inner hydrophilic tubes, where tin oxide (SnO_2) nanoparticles were formed. Figure 4.7 show SEM and TEM images for the SnO_2/DGT composite. Figure 4.7 (a) show that the graphene tubes maintain their tubular structure after the growth of SnO_2 nanoparticles; chemical mapping results from Figure 4.7 (b) indicate a uniform distribution of the nanoparticles within the DGT. Secondly, it appears that Sn nanoparticles prefer to grow on nitrogen-doped graphene surface than the un-doped graphene surface. To confirm, we prepared double-graphene-tubes that consist an outer hydrophilic graphene tube and an inner hydrophobic graphene tube. Sn nanoparticles were also grown on these tubes using a similar process, resulting in a composite denoted as Sn/DGT*. As expected, an appreciable amount of Sn nanoparticles was grown

outside the double-graphene-tubes in Figure 4.6 (g)-(i), confirming the roles of biphilicity on selective growth of SnO_2 nanoparticles within the DGT. Thirdly, although Sn nanoparticles may also be formed in the reaction solution; such nanoparticles could be readily removed during the filtration process, a step used to separate Sn/DGT from the reaction mixture. The ability to confine the growth of Sn nanoparticles within DGT, as well as the ability to remove free Sn nanoparticles from the Sn/DGT, is essential to ensure the high performance of such Sn anodes. For further confirmation, hydrophobic graphene tubes were also synthesized, and the growth of Sn nanoparticles on the hydrophobic graphene tubes could not be observed in Figure 4.8.

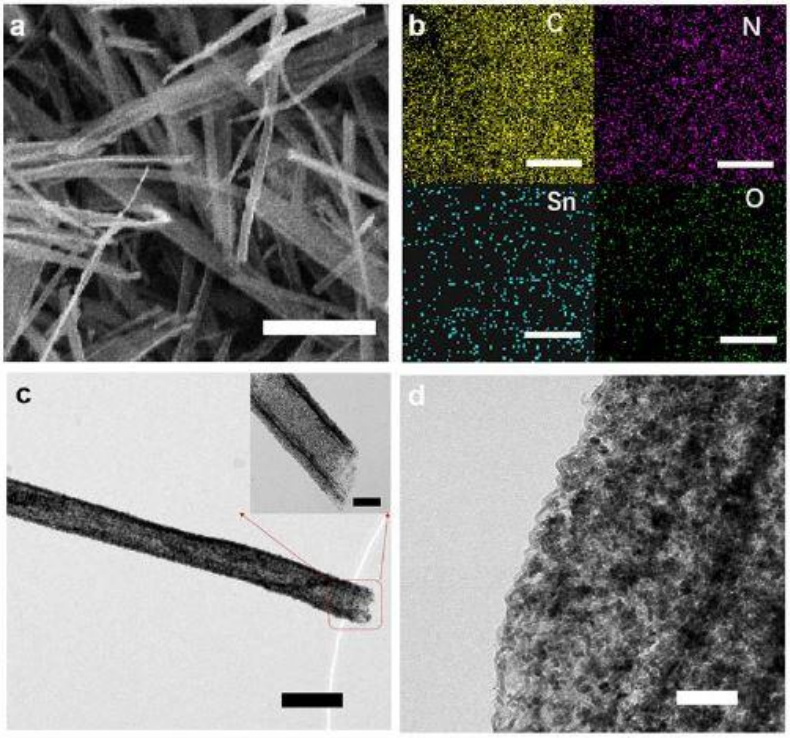

Figure 4.7 (a) SEM image of SnO_2/DGT (Scale bar: 5 μm); (b) EDS elemental maps of Sn, C, O and N (Scale bar: 5 μm); (c) (d) TEM images of SnO_2/DGT (Scale bar: (c) 500 nm, insert of (c) 200 nm; (d) 50 nm).

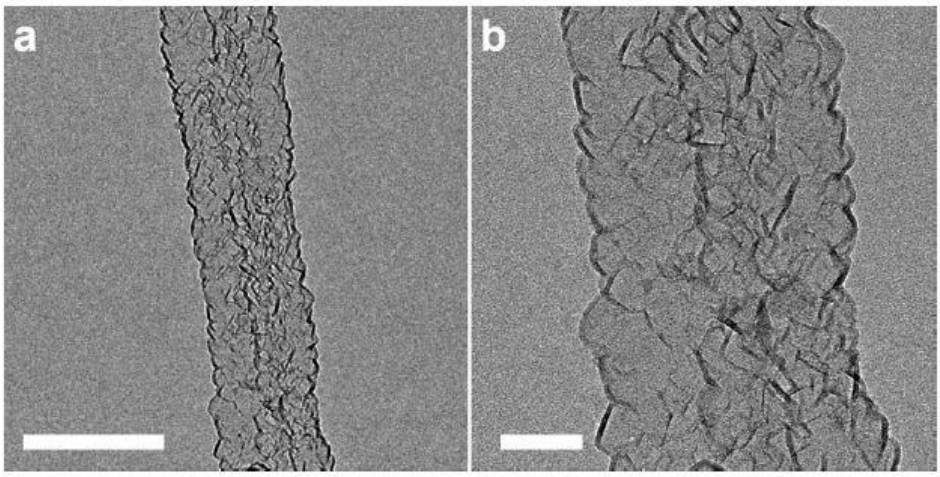

Figure 4.8 (a) (b) TEM images of Sn/hydrophobic graphene tubes (Scale bars: (a) 500 nm; (b) 100 nm).

4.3.2 Electrochemical performance

Figure 4.9 (a) shows the representative charge/discharge voltage profiles of a Sn/DGT electrode from 0.01 to 2.5 V (vs. lithium metal) at 0.2 A g^{-1}. The electrode shows an initial discharge and charge capacity of 1285 mA h g^{-1} and 913 mA h g^{-1}, corresponding to an initial Coulombic efficiency of 71.1%. The excess discharge capacity could be attributed to the decomposition of the electrolyte, the formation of solid electrolyte interphase (SEI), and to irreversible insertion of Li ions into the Sn.[271-272, 275-276] The capacity of the Sn/DGT electrode is mainly contributed by Li insertion at voltage below 0.5 V (vs. Li^+/Li), which ensures a high full-cell voltage and high energy density.[277] As shown in Figure 4.9 (a), the electrode retains a capacity of 918 mA h g^{-1} after 500 cycle, indicating an excellent cycling stability. To further assess the cycling stability of Sn/DGT, electrodes made from commercial Sn particles, as well as a Sn-carbon composite (denoted as Sn/C) was also examined. The Sn/C was synthesized by polymerizing dopamine-hydrochloride on commercial Sn particles followed by carbonization.

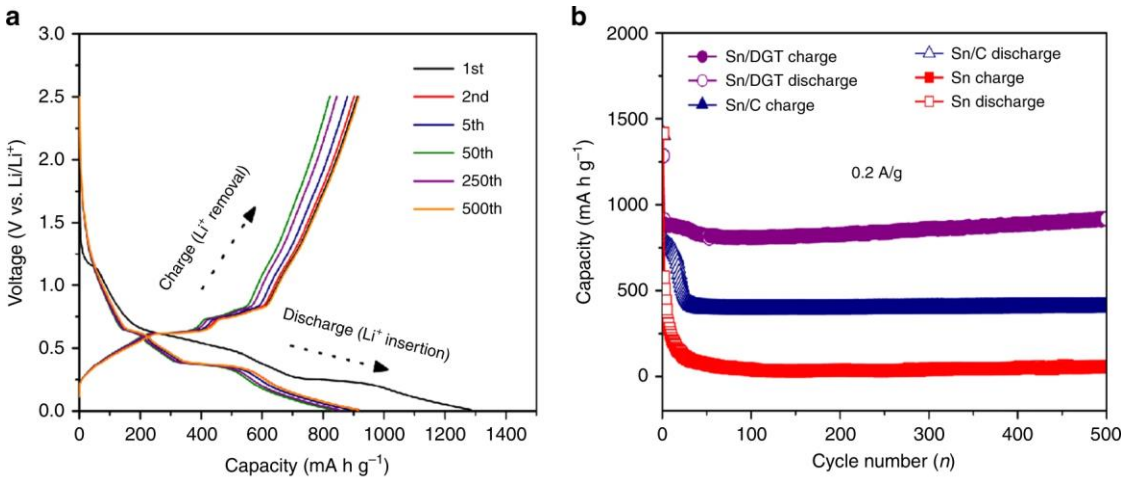

Figure 4.9 Electrochemical performance of the Sn/DGT. (a) Galvanostatic charge-discharge profiles of Sn/DGT from 0.01 to 2.5 V (versus Li/Li^+) for the 1st, 2nd, 10th, 100th, and 500th cycles at a current density of 0.2 A g^{-1}; (b) Cycling performance (charge/discharge) of the Sn/DGT electrode, Sn/C and Sn electrodes with a mass loading of 2 mg cm^{-2} at a current density of 0.2 A g^{-1} for 500 cycles, respectively.

Figure 4.9 (b) compares the capacity of the electrodes made from Sn/DGT, Sn/C, and Sn particles, respectively. After cycling for 500 cycles at a current density of 0.2 A g^{-1}, the Sn/DGT electrode still retains a high Coulombic efficiency (>99%) and a high capacity of 916 mA h g^{-1}, which is 4-folds and 16-folds higher than that of the Sn/C (201 mA h g^{-1}) and Sn (58 mA h g^{-1}) electrode, respectively. Meanwhile, the capacity of the Sn/DGT electrode increases with time possibly due to a continuous activation process.[272, 276]

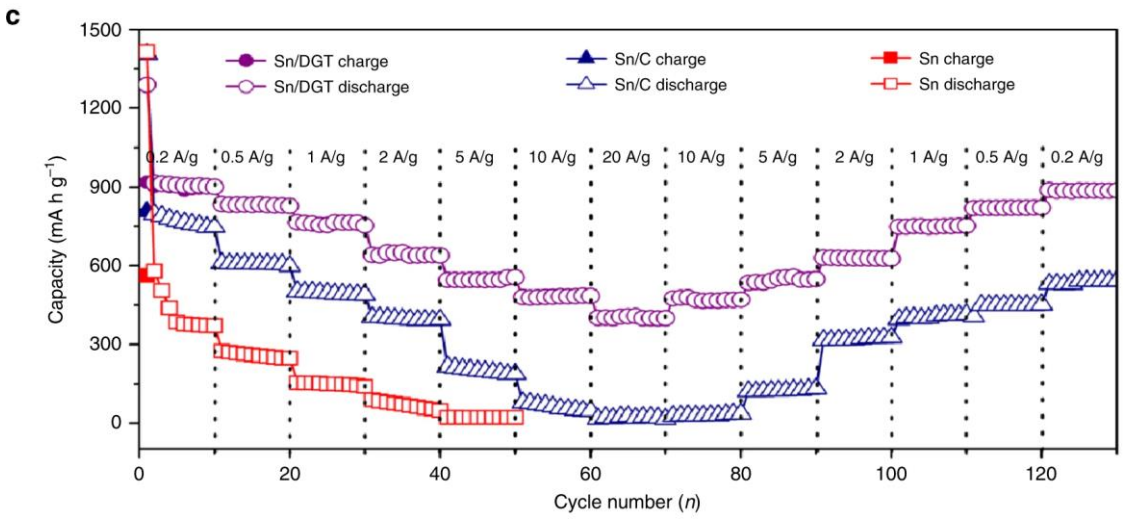

Figure 4.10 The capacity of the Sn/DGT electrode, Sn/C and Sn electrodes at different current densities.

As shown in Figure 4.10, the rate capability of the Sn/DGT electrodes were evaluated at the current densities of 0.2, 0.5, 1, 2, 5, and 10 A g^{-1}, which provides a capacity of 916, 831, 761, 642, 548, and 481 mA h g^{-1}, respectively. Even with a higher current density of 20 A g^{-1} (~20 C), the electrode can still provide a remarkably high capacity of 402 mA g h^{-1}. Returning the cycling current density to 0.2 A g^{-1}, the capacity is recovered to 913 mA g h^{-1}, indicating an outstanding rate capability.[278] The capacity of the composite is contributed by the Sn and DGT moieties. As shown in Figure 4.11, at a voltage window of 0.01–2.5 V, a DGT electrode exhibits a capacity of 712, 665, 592, 551, 474, 371, and 252 mA h g^{-1} at the current density of 0.2, 0.5, 1, 2, 5, 10, and 20 A g^{-1}, respectively. Considering the Sn/DGT composite contains 29 wt% graphene, the capacity contributed by DGT can be estimated as 206, 192, 172, 160, 137, 108, and 73 mA h g^{-1}, respectively. Such SEI layer could be partly decomposed during the charge process, contributing to the charge capacity.[279] And the other is the improved lithium storage capacity by the synergetic effect between conducting DGT and Sn NPs, which is responsible for the excellent electrochemical performance of the overall electrode via the maximum utilization of electrochemically active DGT and nanosized Sn.[270, 280]

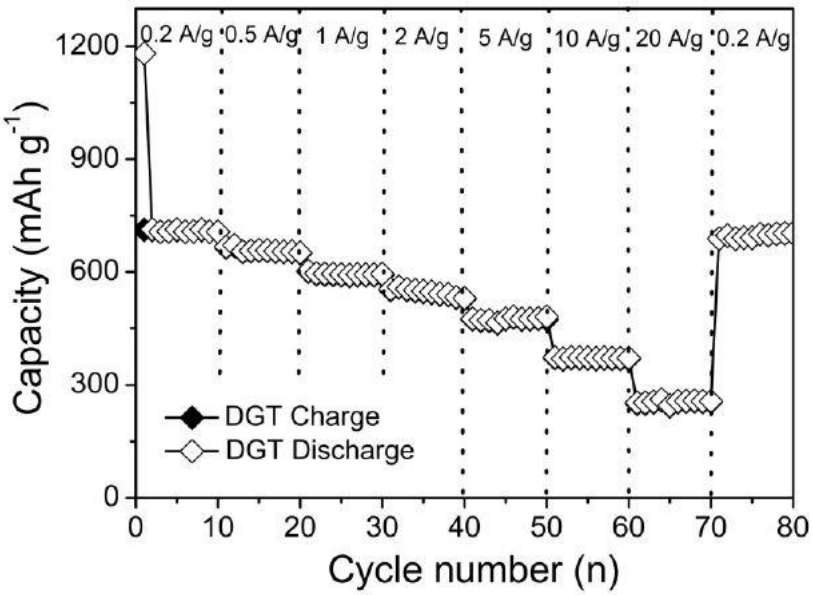

Figure 4.11 The capacity of the DGT electrode at different current densities.

Figure 4.12 compares the Nyquist plots of the Sn/DGT, Sn/C, and Sn electrodes, where the Sn/DGT electrode exhibits a much smaller resistance than the others, which suggests that Sn/DGT electrode has higher ion-diffusion rate and better kinetics during the lithiation/delithation process.

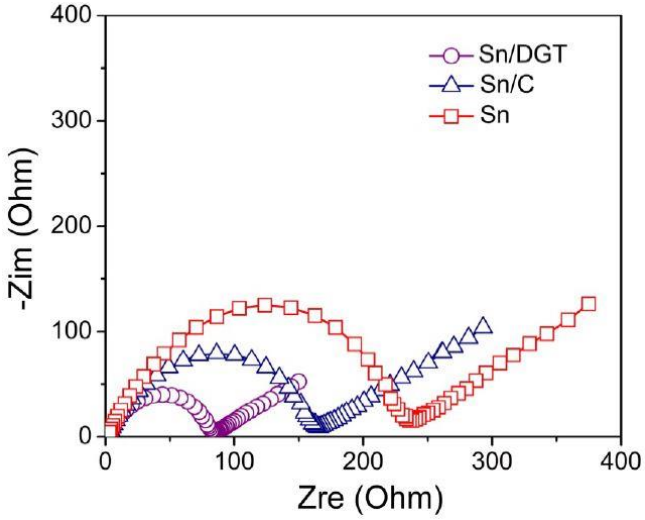

Figure 4.12 Impedance spectra of Sn/DGT, Sn/C and Sn electrodes.

The outstanding cycling stability and rate performance are contributed from the ability to encapsulate the Sn nanoparticles within the highly conductive and robust graphene tubes. Figure 4.13 (d) compares the cycling stability of Sn/DGT and Sn/DGT* (mass loading of 2 mg cm^{-2}) at current density of 0.5 A g^{-1}, which show a similar initial discharge and charge capacity of 1200 mA h g^{-1} and 810 mA h g^{-1}. However, Sn/DGT* contains a significant amount of Sn nanoparticles outside the graphene tubes, which can be easily detached from the graphene tubes during the cycling, resulting in a capacity decay to 337 mA h g^{-1} after 300 cycles. Whereas Sn/DGT still retains a high capacity of 769 mA h g^{-1}, confirming the encapsulation of the Sn nanoparticles do critically contribute to the cycling stability. Figure 4.13 (e) further plots the utilization of the active material versus the charge-discharge current density of the Sn/DGT and Sn/DGT* electrodes. The utilizations are estimated by normalizing the specific capacity of the electrodes at different charge-discharge current densities (the slopes of the lines) vs. the specific capacity at 0.2 A g^{-1}. As shown, the active-material utilization decreases with increasing charge-discharge current density, which is 60%, 52%, and 43% for the Sn/DGT electrode and 20%, 9%, and 6 % for the Sn/DGT* electrode at 5, 10, and 20 A g^{-1}, respectively.

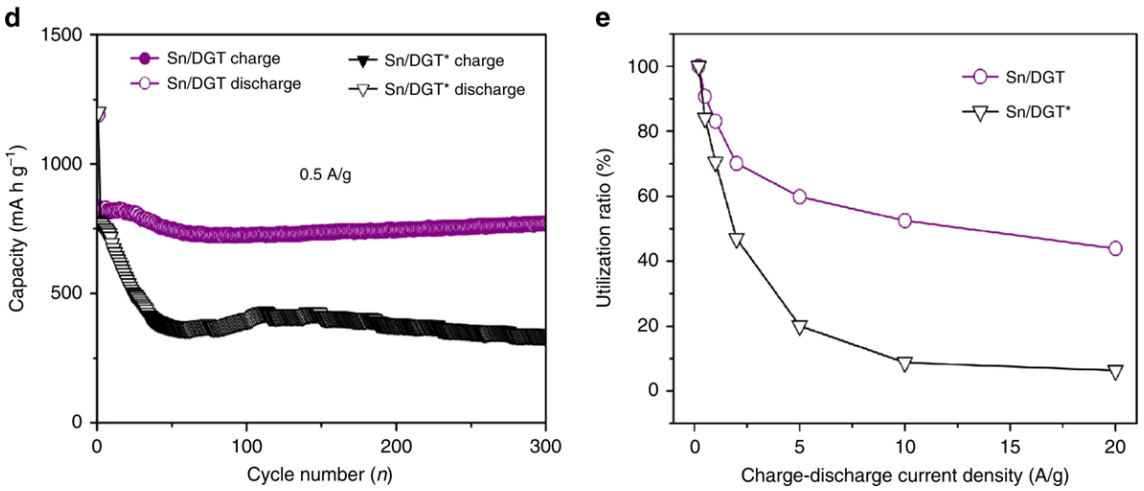

Figure 4.13 (d) Cycling performance (charge/discharge) of the Sn/DGT electrode and Sn/DGT* electrode with a mass loading of 2 mg cm^{-2} at a current density of 0.5 A g^{-1} for 300 cycles; (e) Utilization of the active material of the Sn/DGT electrode and Sn/DGT* electrode at different charge-discharge current densities.

Figure 4.14 (b) (c) show TEM images of the Sn/DGT anode after cycling at 5 A g^{-1} for 500 cycles, confirming that the Sn nanoparticles were still confined within the graphene tubes. As displayed in Figure 4.14 (a), the electrode exhibits the first-cycle discharge and charge capacities of 536 and 722 mA h g^{-1} at the current density of 5 A g^{-1}, respectively, giving a first-cycle Coulombic efficiency of 74.1%, which increases to greater than 98% in the second cycle and to around 99.9% after 500 cycles (the high first-cycle capacity is probably due to SEI formation).

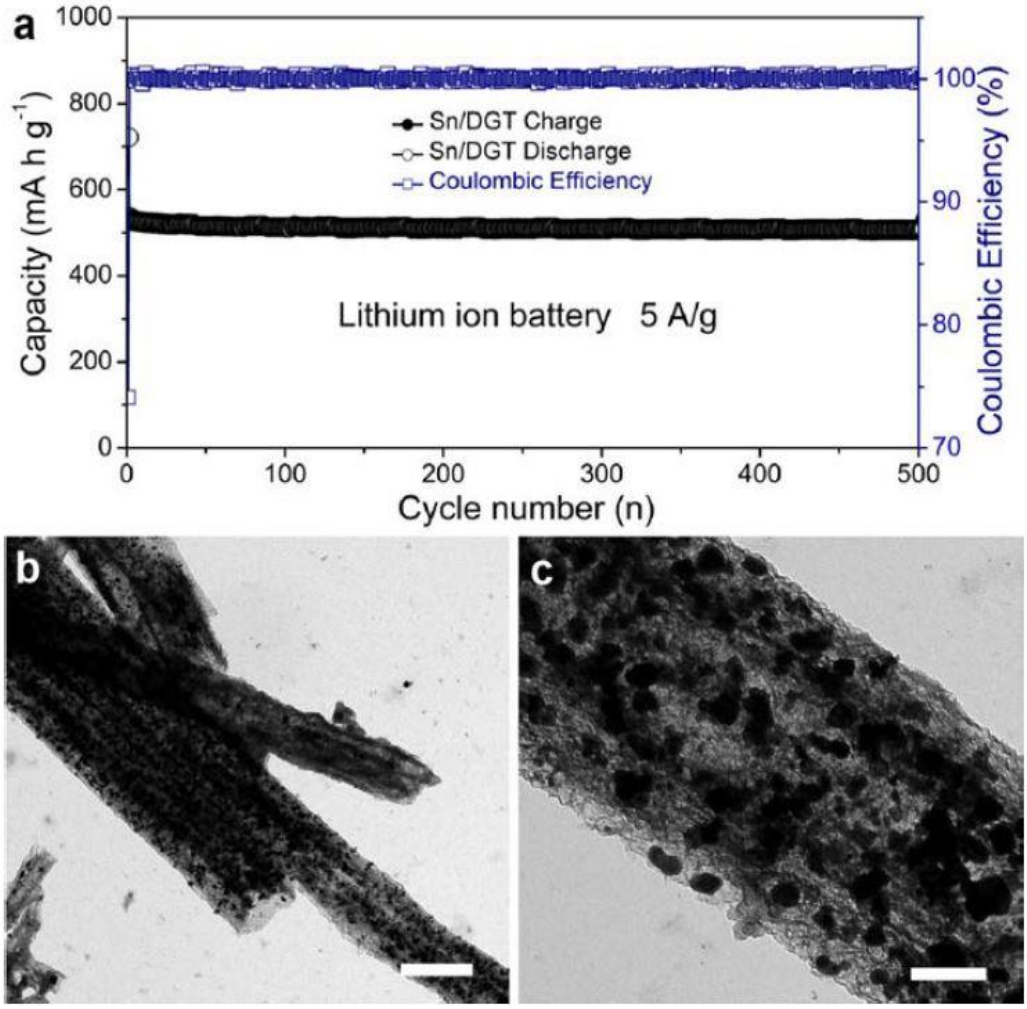

Figure 4.14 (a) Cycling stability of the Sn/DGT electrode at current density of 5 A g^{-1} for 500 cycles; (b) (c) TEM images of the Sn/DGT electrode after 500 cycles at 5 A g^{-1} (Scale bars: (b) 1 μm; (c) 200 nm).

Figure 4.15 (a)-(e) show the low-magnification TEM images, while Figure 4.15 (f)-(j) display high-magnification TEM images of a Sn/DGT tube during the lithiation and delithiation process. The diameter of the graphene tube remains unchanged (480 nm), whereas the Sn nanoparticles reversibly expand and shrink during the lithiation and delithiation, of which the change of the particle size are plotted in Figure 4.15 (k)-(o), respectively. Despite the volume change, these particles remain confined within the graphene tubes. Figure 4.15 (p)-(t) show the selective area electronic diffractions of Sn/DGT during this process. The Sn nanoparticles

exhibit a tetragonal crystal structure (a = 5.8316 Å, c = 3.1813 Å, space group 141) prior to the lithiation in Figure 4.15 (p). After lithiation for 300 s, the diffraction spots are changed to diffraction rings, consistent with a polycrystalline Li_xSn phase. The rings corresponding to a d-spacing of 0.192 nm and 0.237 nm are likely attributable to Li_5Sn_2, while the ring corresponding to a d-spacing of 0.327 nm is likely attributable to Li_7Sn_3 phase in Figure 4.15 (q). After lithiation for 600 s, the Li_xSn phase was converted to the $Li_{4.4}Sn$ phase, corresponding to the diffraction rings with the d-spacings of 0.232, 0.379, and 0.452 nm in Figure 4.15 (r). The subsequent delithiation process reverses the $Li_{4.4}Sn$ phase sequentially to Li_xSn in Figure 4.15 (s) and to tetragonal Sn in Figure 4.15 (t). This observation confirms a reversible phase transformation of the Sn nanoparticles during the lithiation and delithiation, which are confined with the highly conductive and robust graphene tubes and leads to the outstanding cycling stability and rate performance observed.

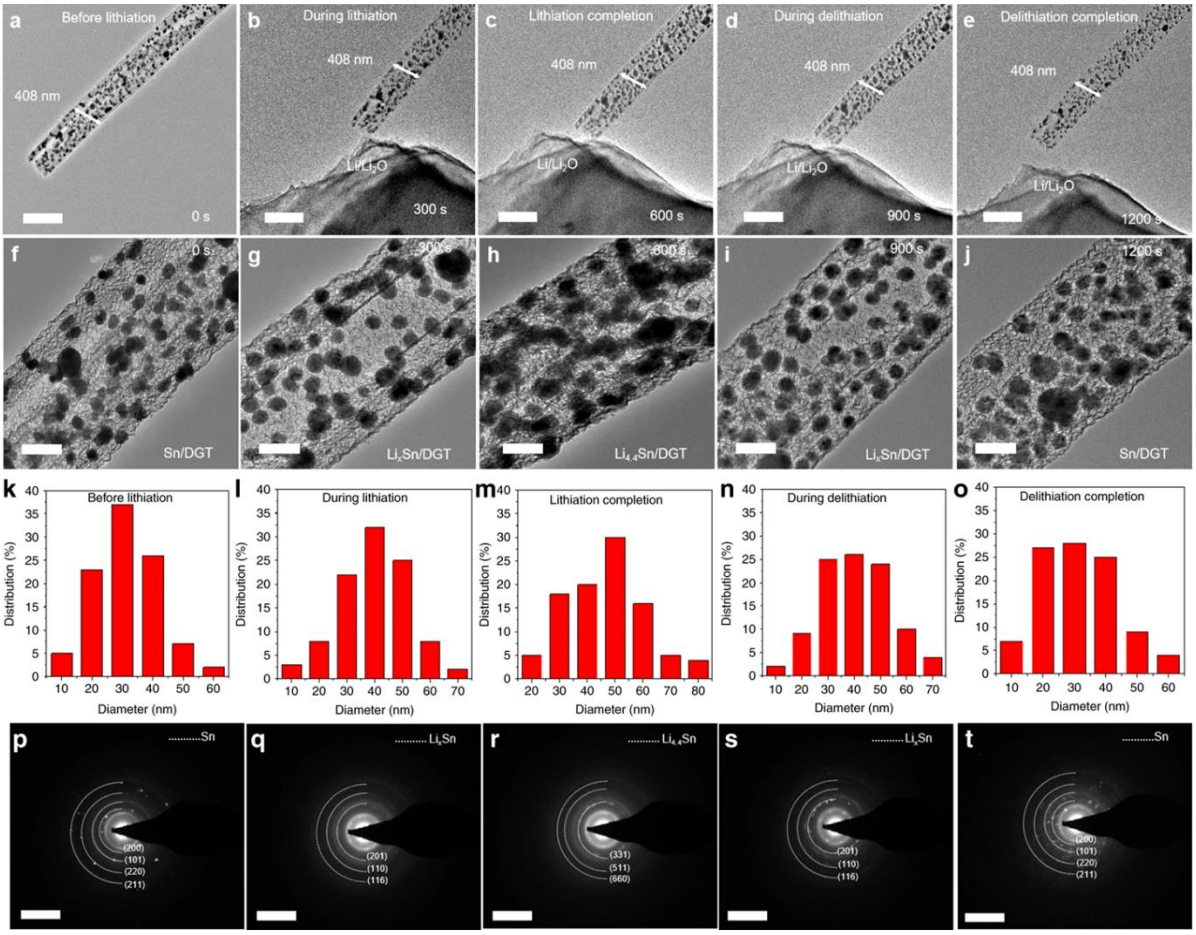

Figure 4.15 In situ TEM observation of Sn/DGT during a lithiation-delithiation cycle. (a)-(e) Time-lapse low magnification TEM images showing the lithiation and delithiation of a Sn/DGT electrode (Scale bars: (a) 500 nm; (b) 500 nm; (c) 500 nm; (d) 500 nm; (e) 500 nm); (f)-(j) High-magnification TEM images showing the lithiation and delithiation of a Sn/DGT electrode (Scale bars: (f) 100 nm; (g) 100 nm; (h) 100 nm; (i) 100 nm; (j) 100 nm); (k)-(o) Size analysis of the Sn nanoparticles during the lithiation-delithiation cycle obtained using a semi-automated sizing approach; (p)-(t) Selective area electron diffraction patterns of the Sn nanoparticles during the lithiation-delithiation cycle (Scale bars: (p) 5 1/ nm; (q) 5 1/nm; (r) 5 1/nm; (s) 5 1/nm; (t) 5 1/nm).

To evaluate that feasibility of adapting Sn/DGT for commercial use, electrodes with different areal mass loadings were fabricated by changing the thickness of the electrode. Figure 4.16 (a) shows the areal capacity *vs*. the areal mass loading of the electrodes at different current densities. The areal capacity increases linearly with the areal mass loading at relatively low current densities (e.g., <5 A g^{-1}); whereas further increasing the current density deviates

the linear relation. Figure 4.16 (b) plots the areal capacity vs. the areal current density, where the electrode with a mass loading of 6 mg cm^{-2} exhibits areal capacities of 5.4, 4.9, 4.4, and 3.7 mA h cm^{-2} at the areal current density of 1.6, 4, 8, and 16 mA cm^{-2}, respectively. For comparison, commercial graphite anodes generally provide areal capacities in the range of 2.5–3.5 mA h cm^{-2} at a current-density range of 0.3–1.86 mA cm^{-2} (see the marked area marked in Figure 4.16 (b)).[281] Clearly, Sn/DGT electrodes well outperform the commercial graphite anodes.

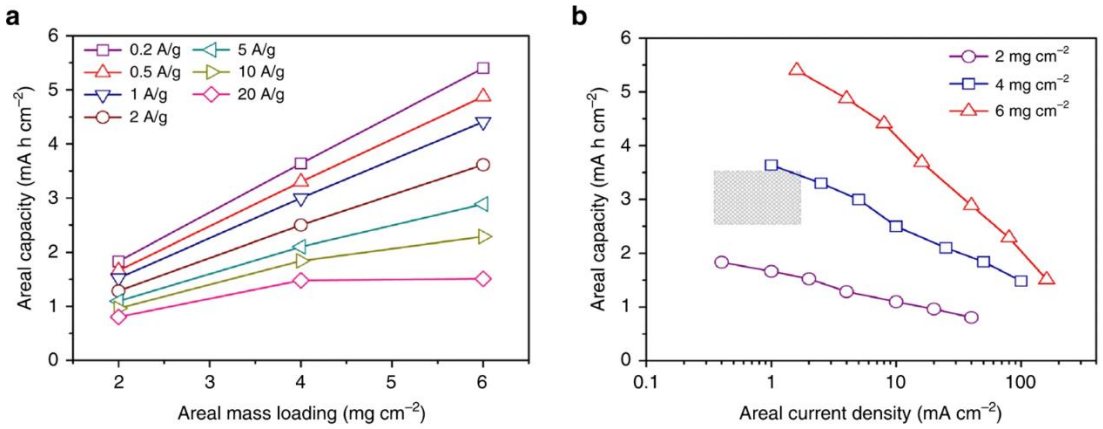

Figure 4.16 (a) The areal capacity of Sn/DGT electrodes with mass loading of 2, 4, and 6 mg cm^{-2} at different charge-discharge current densities; (b) The areal capacity of Sn/DGT electrodes vs. the areal current density of the Sn/DGT anodes with a mass loading of 2, 4, and 6 mg cm^{-2}, respectively.

Furthermore, these thick Sn/DGT electrodes also exhibit outstanding cycling stability. For example, after cycling a current density of 2 A g^{-1} for 200 cycles, these electrodes retain over 90% of their initial capacity in Figure 4.17 (a) with low charge-transfer resistance indicated by their electrochemical impendence spectra Figure 4.17 (b).

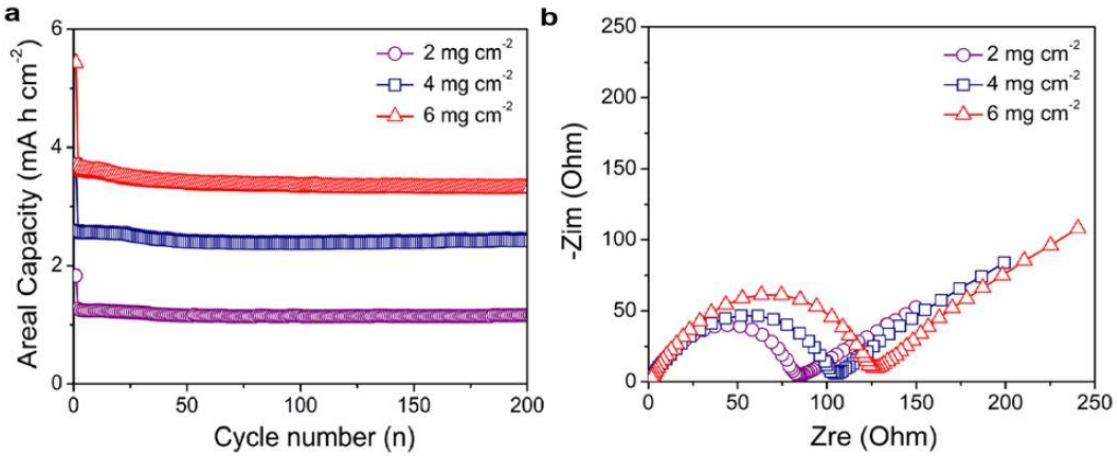

Figure 4.17 (a) Areal capacity and cycling performance of the Sn/DGT electrode at the current density of 2 A g^{-1} for 200 cycles under different mass loadings; (b) Nyquist plots of the Sn/DGT electrodes under different mass loadings.

Figure 4.18 (c) plots the areal capacity vs. the areal current density of representative anode materials, including commercial graphite, graphene, $Li_4Ti_5O_{12}$, Sn/C, and Si/C-based composites. As shown, graphene aerogel, popcorn-like graphene,[152, 282] and edge-activated graphite exhibit higher areal capacities and improved rate performance that graphite. Incorporating high-capacity Si to graphene and graphite further increases their areal capacity at low current density. However, inherently limited by the slow reaction between silicon and lithium, the capacity is decreased rapidly with increasing the current density. The Sn/DGT electrodes well outperformances the reported electrodes in both areal capacity and rate performance. For example, the Sn/DGT anode can supply a high areal capacity over 4 mA h cm^{-2} at the areal current density of 10 mA cm^{-2}, which is the best-known values for the anodes reported.[152, 241, 269, 271, 282-286]

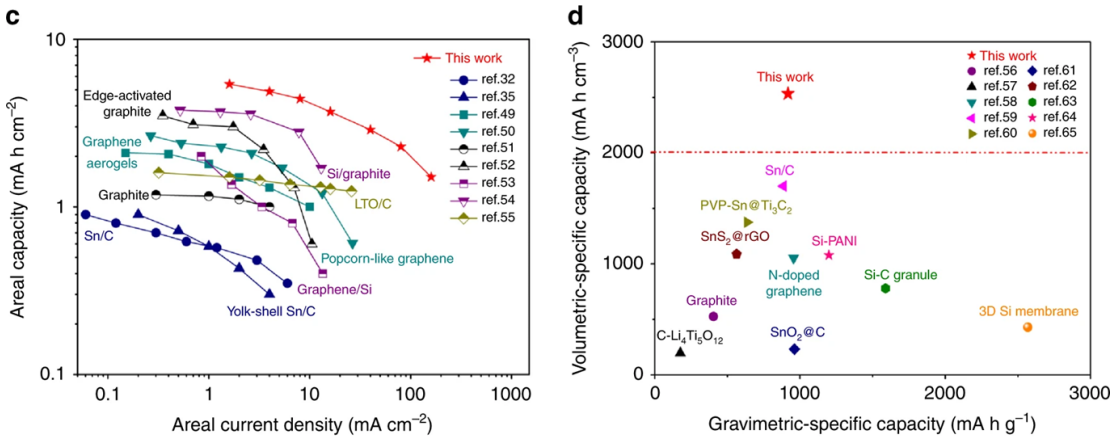

Figure 4.18 (c) A comparison of the areal performance metrics of Sn/DGT electrode (mass loadings of 6 mg cm^{-2}) with representative anodes reported, including the anodes from graphite, graphene, $Li_4Ti_5O_{12}$ (LTO), Sn/C and Si/C; (d) A comparison of the specific volumetric capacity of Sn/DGT electrode (active materials only) with reported anode materials, including the anodes of graphite, LTO, Sn/C, and Si/C.

Figure 4.18 (d) compares the volumetric capacities of representative anode materials vs. their gravimetric capacity, including commercial graphite, $Li_4Ti_5O_{12}$, Sn-based, and Si-based anodes reported.[253, 287-295] The volumetric capacities of the anode materials (active material only) were estimated based on the tap density and gravimetric specific capacity in un-lithiated state. Sn/DGT shows a tap density around 2.76 g cm^{-3}, corresponding a volumetric capacity of 2532 mA h cm^{-3} and 1106 mA h cm^{-3} at a current density of 0.2 A g^{-1} and 20 A g^{-1}, respectively in Figure 4.19 (a). The electrode retains a high volumetric capacity of 2528 mA h cm^{-3} after 500 cycles under a current density of 0.2 A g^{-1} in Figure 4.19 (b). The volumetric capacity of the Sn/DGT electrodes well outperformances the reported anodes, despite their gravimetric capacity is less than the silicon granule[253] and 3D silicon membrane.[295]

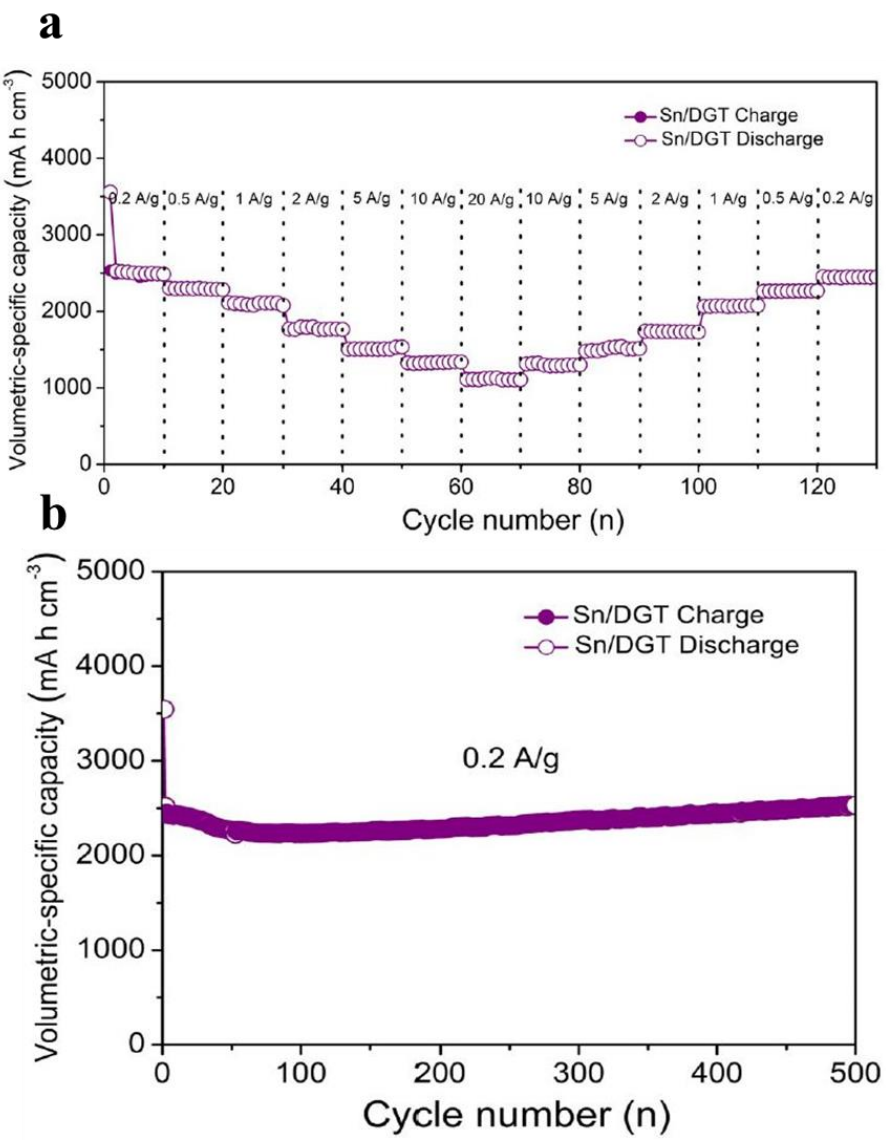

Figure 4.19 (a) The volumetric capacity of Sn/DGT electrode (active material only) at different current densities; (b) Cycling performance of Sn/DGT electrode.

Finally, to demonstrate the viability of using Sn/DGT as the high-performance anodes, full cells were assembled using a commercial cathode material, lithium-nickel cobalt manganese oxide (NCM622) with a bulk density (4.5 g cm^{-3}). For comparison, control cells were also assembled using a graphite anode and a NCM622 cathode. Figure 4.20 (e) shows the cycling performance of the NCM622//Sn/DGT cell, displaying a gravimetric energy density of 590 W h Kg^{-1} with a capacity retention of 93% over 200 cycles (based on the total mass of electrode

materials), which is significantly higher than that of the NCM622//graphite cell. In this cell configuration, the areal capacity of the electrode is 3.2 mA h cm^{-2} and the thickness of the cell (including the anode, cathode, current collector, and separator) is ~92 μm in Figure 4.21 (a). The volumetric energy density of the cell is estimated to be 1252 W h L^{-1} in Figure 4.21 (b). This value represents a near two-fold increase from that of the commercial NCM622//graphite cell calculated based on the same metric (647 W h L^{-1}). Note that the current-state-of-art commercial LIBs generally possess a volumetric energy density from 600 W h L^{-1} to 700 W h L^{-1}, which is consistent with that of the control cell. This comparison further confirms the feasibility of fabricating LIBs with significantly improved volumetric energy density using Sn/DGT as the anodes. It is also worth noting that the volumetric energy density of the NCM622//Sn/DGT cell is still around 1.8 times higher than that of the NCM622//graphite cell (602 W h L^{-1}) after 200 cycles in Figure 4.20 (f). The ability to fabricate full cells with such high gravimetric and volumetric energy density, as well as long cycling life, indeed opens a new avenue towards high-performance LIBs for microelectronic and electrical vehicle application.

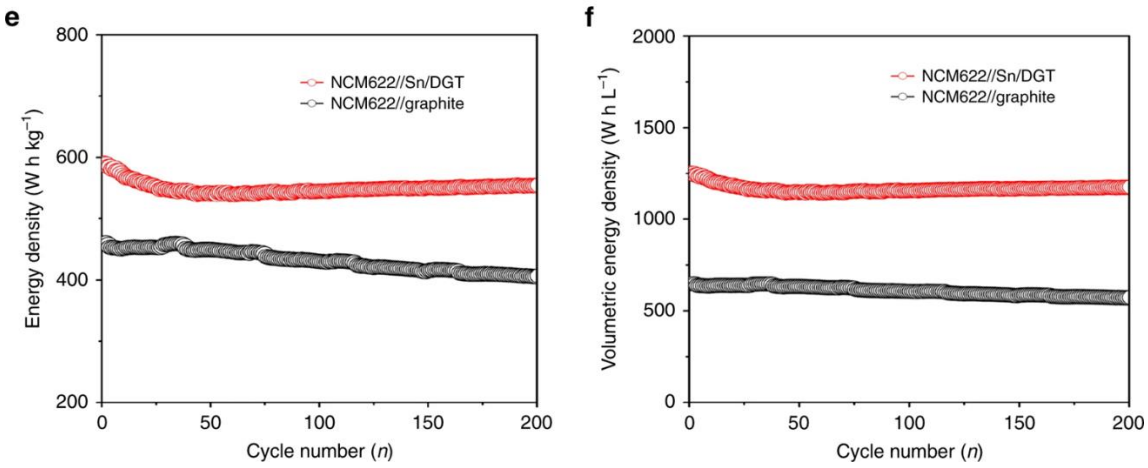

Figure 4.20 (e) The gravimetric energy density of a cell consisting with a NCM622 cathode and a Sn/DGT anode, as well as a cell consisting with a NCM622 cathode and graphite anode;

(f) The volumetric energy density of a cell consisting with a NCM622 cathode and a Sn/DGT anode, as well as a cell consisting with a NCM622 cathode and graphite anode.

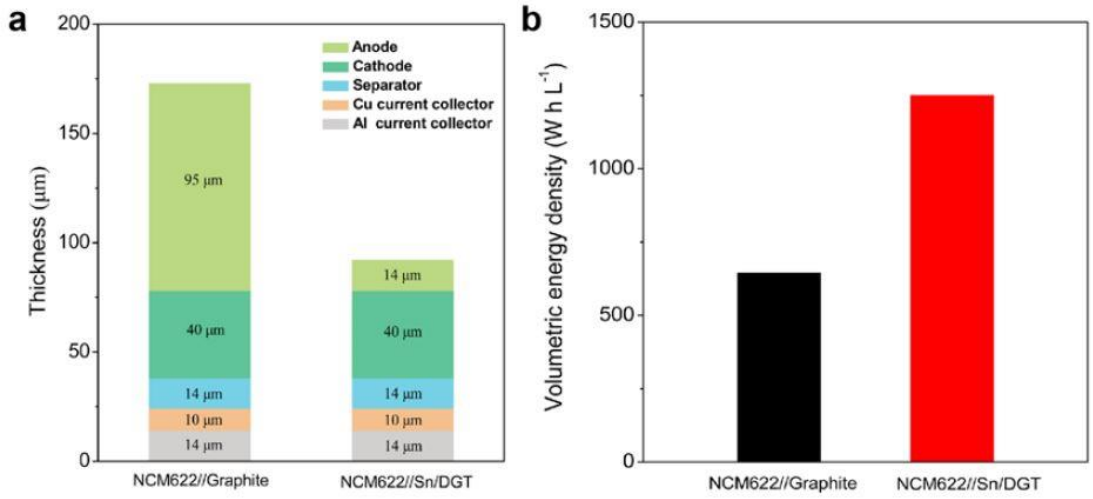

Figure 4.21 (a) The electrode thickness of a NCM622//Sn/DGT and NCM622//graphite full cell; (b) The volumetric energy density of a NCM622//Sn/DGT and NCM622//graphite full cell.

4.4 Conclusion

In summary, we have developed Sn anodes with both high gravimetric and volumetric capacities. This is achieved simply by encapsulating Sn nanoparticles, a metal with high gravimetric and volumetric capacity, within highly conductive and robust graphene tubes. Despite their large-volume change during cycling, the Sn nanoparticles are confined with the graphene tubes, ensuring an outstanding rate performance and long cycling life. Meanwhile, through creating the double-graphene-tubes with biphilic nature, we minimized the amount of free Sn nanoparticles in the electrodes, which could have caused rapid capacity decay upon detaching from the graphene tubes. This strategy significantly improves the gravimetric energy density and volumetric energy density of LIBs. We expect that adopting such Sn anodes could potentially double the volumetric energy density of the LIBs in the current market. Meanwhile, the selective-growth strategy can be extended to synthesize a variety of functional materials for a broad range of applications.

Chapter 5 High Performance Sodium Ion Anodes Based on Sn_4P_3 Encapsulated within Amphiphilic Graphene Tubes

5.1 Introduction

In parallel to lithium-ion batteries, sodium-ion batteries (SIBs) have emerged as a prominent alternative for energy storage due to abundance and low cost of sodium resources.[296] Commercial adoption of SIBs is yet hampered by lack of anode materials with high capacity, suitable redox potential and cycling robustness. The sodium storage mechanisms in anodes can be basically categorized into intercalation, alloying and conversion. Intercalation mechanism signifies that sodium can be inserted into crystal structure with preserved structure integrity.[297] Carbon based materials fall into this category and exhibit small volume expansion upon sodiation. Alloying and conversion mechanisms denote that materials can form intermetallic binary compounds by alloying with sodium, and react with sodium by conversion reaction, respectively. Both of these two mechanisms produce new compounds and consequent huge volume change.

Among miscellaneous anode candidates, sodium alloyable tin (Sn) and phosphorous (P) are quite promising, given their high theoretical capacities (Sn: 847 mAh g^{-1}; P: 2596 mAh g^{-1}) that significantly exceed the values of conventional carbonaceous materials (e.g., hard carbon, 300 mAh g^{-1}).[217, 298-299] More recently, tin phosphide (Sn_4P_3) that combines the merits of P and Sn has garnered considerable attentions by offering a high capacity of 1132 mAh g^{-1}, decent electrical conductivity of 30.7 S cm^{-1}, and dendrite-preventive redox potential of 0.3V (*vs.* Na/Na^+).[220, 300-302] Nevertheless, such alloying-type materials often suffer from colossal volume change (up to 510%) upon sodiation and desodiation, eventually causing pulverization,

electrode fragmentation and drastic cyclic degradation of the electrodes.[211, 303]

A well-documented approach to improve the cycling stability is compositing Sn_4P_3 with carbonaceous materials, which generally contain pores and anchoring sites to host Sn_4P_3 particles and accommodate their volume change. Additionally, the carbonaceous materials provide electron-transport pathways facilitating the reaction kinetics, and also help to stabilize the electrode-electrolyte interfaces and improve the coulombic efficiency.[304-305] For examples, the composites of Sn_4P_3 with graphene,[306-307] reduced graphene oxide,[308-310] carbon nanotubes[221, 223, 311] and hard carbon[312-313] have been explored, leading to enhanced charge-transfer kinetics and electrochemical performances. However, significant decay in capacity still occurs during cycling, which may be attributed to the conversion of Sn_4P_3 into Sn and poorly conductive P,[314-317] as well as the detachment of Sn_4P_3 from the conductive networks because of the large volume change.[318-321] To mitigate the capacity decay, Sn_4P_3 particles were embedded within carbon nanospheres by reduction and subsequent phosphidation of carbon-coated hollow SnO_2 nanospheres. Such a yolk-shell structure not only provides accommodate the volume expansion of the particles, but also constrains the particles within the conductive spheres, leading to significantly improved cycling stability.[222, 322-323] Nevertheless, such an encapsulating process often results in the formation of un-encapsulated Sn_4P_3 particles, which unavoidably cause capacity decay upon detachment from the conductive networks.

We report herein novel composite anodes based on Sn_4P_3 encapsulated within amphiphilic and porous graphene tubes (GT). Such amphiphilic GT consist an inner hydrophilic graphene tube (nitrogen-doped) and an outer hydrophobic graphene tube (un-doped), which guarantees a confined growth of Sn_4P_3 nanoparticles within the GT and effective accommodation of the

volume expansion of the nanoparticles. The amphiphilic property of such porous GT has been proved in our former paper.[324]

Compared with current state of the arts, such Sn_4P_3/GT composite has multiple advantages: (i) the formation of Sn_4P_3 nanoparticles provides shortened diffusion path for sodium ions while alleviates the mechanical stress during alloying/dealloying process; (ii) hosting Sn_4P_3 nanoparticles within the flexible GT effectively buffers the volume change during cycling and retains the electrical contact with GT; (iii) the use of GT allows construction of highly conductive framework, which enables fast charge transport and improves the electrochemical kinetics of Sn_4P_3. Collectively, these advantages lead to the fabrication of high-performance Sn_4P_3 anodes with high capacity, high-rate performance and long cycling stability.

5.2 Experimental

Synthesis of MgO tube. An aqueous urea solution (1.2 g in 20 mL deionized water) was dropped into a magnesium acetate solution (12 g in 80 mL deionized water). The mixed solution was stirred for 1h, sealed in a 200 mL Teflon-lined autoclave, and heated at 180 °C for 2 h. As-formed $Mg(OH)_2$ was filtrated, washed with ethanol, dried in vacuum at 100 °C, and calcined at 600 °C for 6 h in air to obtain the MgO nanowire template.

Synthesis of DGT. The MgO template was placed in a horizontal quartz tube to develop graphene with chemical vapor deposition (CVD) method. The quartz tube was heated to 900 °C under a flow of Argon (1000.0 mL min^{-1}) and another Argon stream (150.0 mL min^{-1}) flowing through a flask of acetonitrile for 10 min to develop nitrogen-doped graphene coated on the

MgO template. As-formed nitrogen-doped graphene was dispersed in a solution which contains $Mg(NO_3)_2 \cdot 2H_2O$ (0.5 g, Sigma-Aldrich) and urea (0.2 g, Sigma-Aldrich) in deionized water (100 mL) to sonicate for 30 min. After refluxing at 90 °C for 24 h, the mixture was washed and dried at 80 °C overnight. The nitrogen-doped graphene/MgO was coated with graphene under a flow of CH_4 (400.0 mL min^{-1}) and Argon (1000.0 mL min^{-1}) at 1000 °C for 10 min. Finally, the product was etched with hydrochloric acid solution (1 mol L^{-1}) to obtain the double graphene tubes (DGT).

Synthesis of Sn_4P_3/GT. GT (30 mg) was added into the deionized water (30 mL) by sonication for 30 min. $K_2SnO_3 \cdot 3H_2O$ (0.2 g) was dissolved into the above solution and stirred for 1 h. After that, the solution was transferred to 50 mL Teflon-lined autoclave and maintained at 180 °C for 12 h to form SnO_2/GT composite. Then, as-formed SnO_2/GT was obtained by centrifugation and dried at 80 °C overnight. To form Sn_4P_3/GT composite, SnO_2/GT (80 mg) was reacted with NaH_2PO_2 (400 mg) at 300 °C for 1 h under nitrogen atmosphere.

Material characterization. The morphology and structure of the as-prepared products were conducted by field-emission scanning electron microscopy (FESEM, FEI Nova 430), transmission electron microscopy and high-resolution transmission electron microscopy (HRTEM, FEI Titan STEM). Powder X-ray diffraction was performed on Rigaku Miniflex II diffractometer with Cu Kα radiation operated at 30 kV and 15 mA. Raman spectroscopy was measured with Renishaw 2000 System. The specific surface area was tested by an ASAP 2020 analyzer (Micromeritics Instrument Corporation, Norcross, GA). The TGA was measured on an SDT Q600 thermoanalyzer under air.

Electrochemical measurements. The electrode slurry was prepared by mixing 80 wt-% active materials, 10 wt-% acetylene carbon black, 10 wt-% PVDF binder, and an adequate amount of N-methyl-2-pyrrolidone. The slurry was coated onto copper foil and dried in a vacuum oven at 110 °C for 12 h. The loading mass of active materials on electrode was 1.5 mg cm^{-2}. The electrical performance was tested using standard 2025 type coin cells using sodium metal foil as a counter electrode, glass fiber (GF/D) from Whatman as a separator, and 1.0 M $NaClO_4$ as electrolyte (in propylene carbonate, containing 5 wt-% fluoroethylene carbonate). The sodium metal cube (CAS number: 7440-23-5) was bought from Sigma-Aldrich and cut into round pieces with a diameter of 12 mm, then flattened as thin sodium metal foil to assemble the battery. The total amount of electrolyte that used in the battery was 60 μL. The charge-discharge properties were measured using a Land Battery Test System (LAND CT2001A) within a voltage window from 0.01 to 2.0 V (versus Na^+/Na) at room temperature. Electrochemical impedance measurement was evaluated in a range of 0.01 Hz to 10 MHz at 10 mV with a perturbation amplitude of 10 mV on the cells at open circuit potential. The capacities of the electrodes were calculated according to the total mass of the Sn_4P_3/GT composite.

5.3 Results and discussions

As illustrated in Figure 5.1, GT are dispersed in an aqueous solution containing an aqueous tin precursor, which allows the infiltration of the solution to the hydrophilic tubes. A subsequent hydrothermal treatment converts the precursor into SnO_2, leading to the formation of GT composites with SnO_2 nanoparticles grown within the inner tubes. It is worth noting that SnO_2 nanoparticles may also grow outside the GT and in the solution, nevertheless, such

nanoparticles can be readily removed by washing and filtration, affording the formation of GT composites with well-encapsulated SnO_2 nanoparticles. Lastly, the encapsulated SnO_2 is converted to Sn_4P_3 through a phosphidation treatment, leading to the formation of Sn_4P_3/GT composite with Sn_4P_3 confined within the GT. Compared with the prior arts, the unique amphiphilicity of GT permits exclusive formation of Sn_4P_3 particles inside the N-doped GT, which not only accommodates their volume change during sodiation and de-sodiation, but also retains such particles and their cycling compounds within the GT. Such conductive GT, as well as the nano-size Sn_4P_3, afford faster electron and ion transports leading to improved electrochemical kinetics, high-rate capability, and long cycling stability.

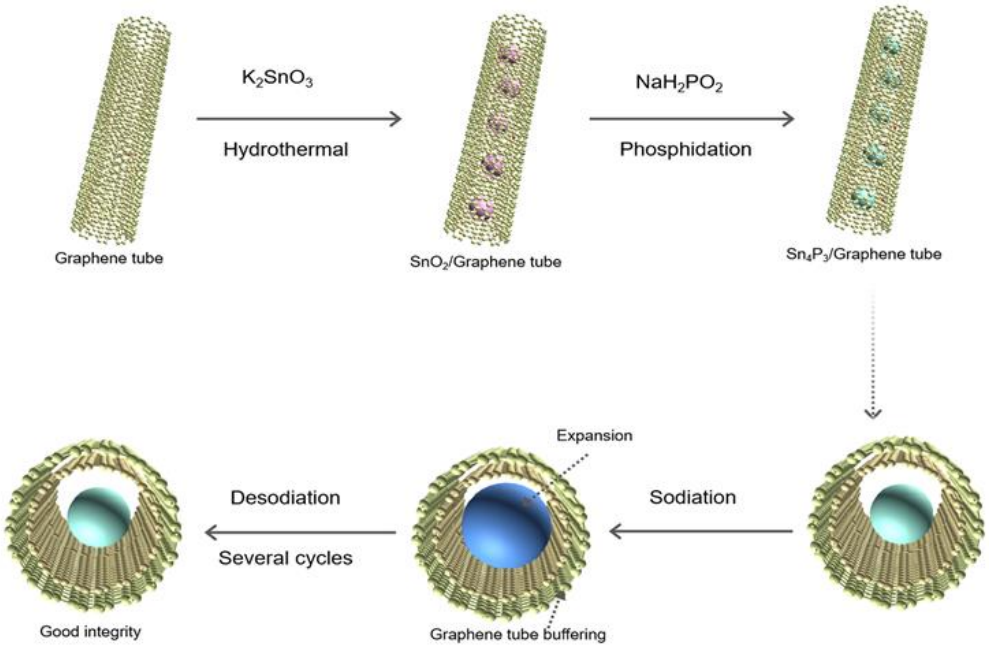

Figure 5.1 A schematic illustration showing the synthesis of Sn_4P_3/GT composites by selectively growth of SnO_2 nanoparticles within GT followed by a phosphidation process forming Sn_4P_3/GT and their sodiation and desodiation process.

5.3.1 Characterization

Figure 5.2 (A)-(D) show SEM images, TEM images and selected area electron diffraction (SAED) of the resulting GT, which display an average diameter of ~ 400 nm and length in range of 10-20 μm. The SAED pattern displays the (101) and (002) reflections of graphene structure, which is consistent with the XRD result in Figure 5.3 (A). Figure 5.2 (E)-(G) display SEM image and TEM images of SnO_2/GT, indicating SnO_2 nanoparticles are homogenously confined within the graphene tubes. The SAED of SnO_2/GT in Figure 5.2 (H) shows typical diffraction rings of SnO_2 with a tetragonal rutile phase (JCPDS No. 41-1445) which is corresponding to the pattern in Figure 5.3 (A). Figure 5.2 (I)-(K) show SEM and TEM images of Sn_4P_3/GT, again indicating that the Sn_4P_3 nanoparticles are homogenously confined within the GT. These Sn_4P_3 nanoparticles exhibit an average diameter of ~ 50 nm, of which the SAED in Figure 5.2 (L) shows diffraction rings attributed to tetragonal phase Sn_4P_3. Consistently, XRD patterns in Figure 5.3 (A) (B) shows the nanoparticles exhibit a Sn_4P_3 phase (JCPDS No. 73-1820) without impurity peak, indicating that SnO_2 nanocrystals are fully phosphated.[212, 271]

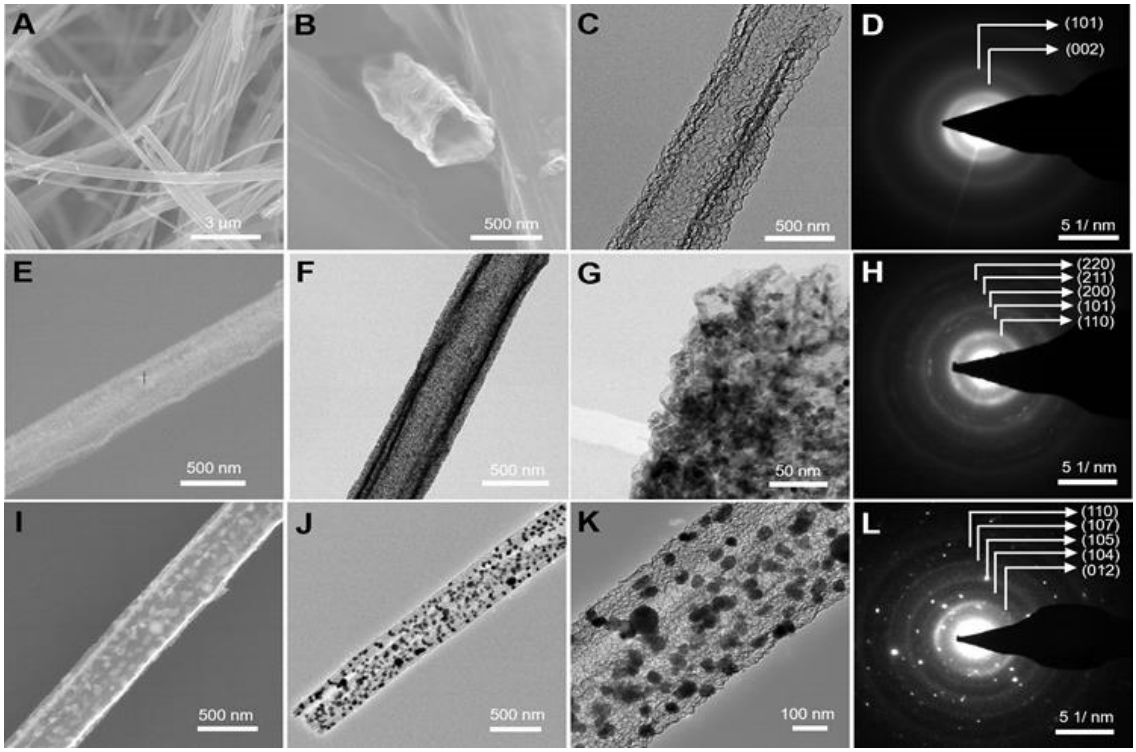

Figure 5.2 Morphology and structure of GT, SnO_2/GT and Sn_4P_3/GT. (A) (B) SEM images, (C) TEM image, and (D) SAED of graphene tubes (GT); (e) SEM image, (F, G) TEM images, and (H) SAED of SnO_2/GT composite; (I) SEM image, (J, K) TEM images, and (L) SAED of Sn_4P_3/GT composite.

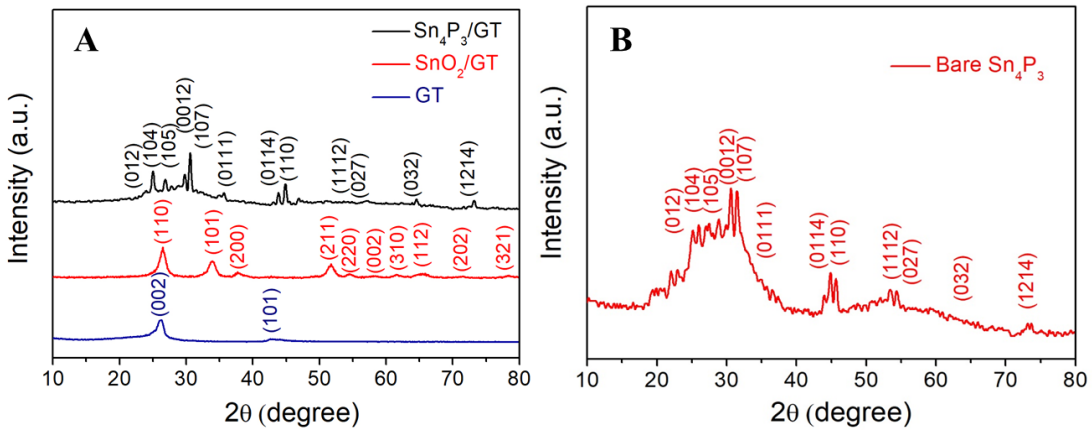

Figure 5.3 (A) XRD patterns of GT, SnO_2/GT and Sn_4P_3/GT; (B) XRD pattern of bare Sn_4P_3.

Raman spectra of GT and Sn_4P_3/GT are shown in Figure 5.4 (A), where the two peaks observed at 1331 cm^{-1} (D-band) and 1576 cm^{-1} (G-band) in both curves are identified as

disordered graphitic layers and vibration of sp2-bonded carbon atoms (graphitized carbon), respectively.[168, 241] The higher relative intensity of G-band over D-band signifies the high graphitization degree and electrically conductive nature of GT. As shown in Figure 5.4 (B), the mass ratio of Sn_4P_3 in Sn_4P_3/GT was measured by thermal gravimetric analysis (TGA) in air. The weight loss below 100 °C is attributed to the removal of moisture in the composite. The weight change from 200 to 600 °C is ascribed to the oxidation of Sn_4P_3 and GT. According to the final weight of SnO_2 in the TGA cure, the content of Sn_4P_3 in Sn_4P_3/GT is calculated to be 74 wt%.

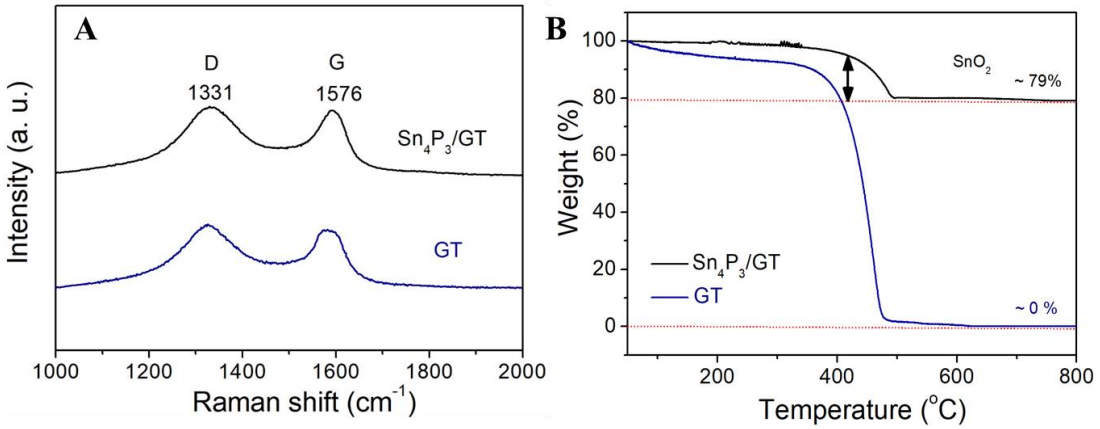

Figure 5.4 (A) Raman spectra of GT and Sn_4P_3/GT; (B) TGA results of GT and Sn_4P_3/GT.

5.3.2 Electrochemical performance

Figure 5.5 (A) shows typical charge/discharge voltage profiles of a Sn_4P_3/GT electrode in 0.01-2 V (*vs.* Na/Na^+) under a current density of 0.5 A g^{-1}, which indicates an initial discharge and charge capacities of 1002 and 722 mA h g^{-1}, respectively, with an initial Coulombic efficiency of 72.2%. The irreversible capacity observed during the initial charge/discharge cycle is mainly attributed to the formation of SEI film;[274, 325] Though the present value outperforms initial Coulombic efficiency of most high-capacity alloying and conversion-type

materials (below 70%), higher value beyond 90% is required for practical application. Optimization of electrolyte and SEI compositions could be further explored to diminish the initial irreversible loss.[326] After 500 cycles, the electrode still provides a stable capacity of 713 mA h g^{-1}. In addition, the charge/discharge voltage profiles are overlapped after the initial cycle, indicating an excellent cycling stability. Figure 5.5 (B) further investigates the cycling stability of the Sn_4P_3/GT electrode using a current density of 0.5 A g^{-1}, which provides a specific capacity of 713 mA h g^{-1} after 500 cycles, a value that is eight times higher than that of un-confined Sn_4P_3 nanoparticles (85 mA h g^{-1}). Meanwhile, the specific capacity of Sn_4P_3/GT electrode slightly increases with cycling, which may be attributed to an activation process. The Sn_4P_3/GT electrode shows a high Coulombic efficiency (> 99%) after the initial several cycles, demonstrating excellent reversibility. Compared to bare Sn_4P_3 nanoparticles, Sn_4P_3/GT exhibits a much higher reversible capacity and significantly improved cycling stability, which can be attributed to the capability of GT that buffer the volume change of and retain the electrical contact of Sn_4P_3 particles during cycling.

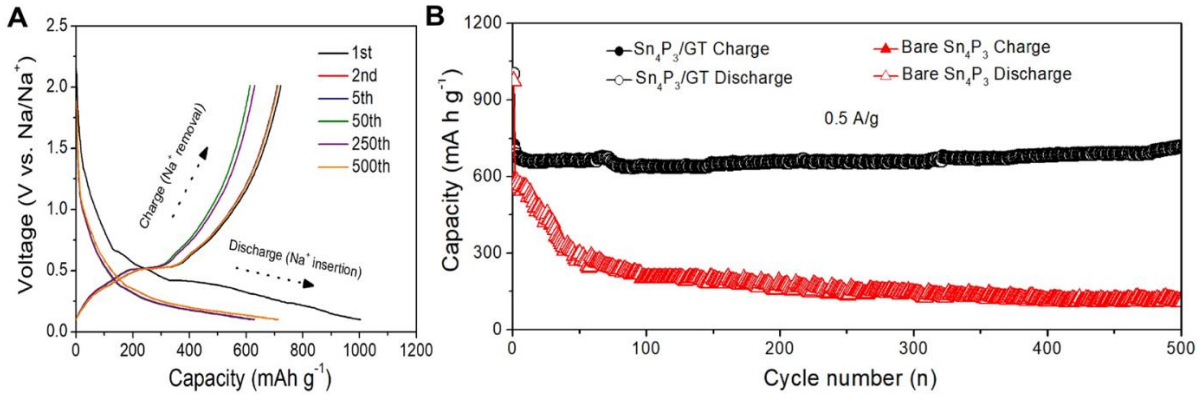

Figure 5.5 (A) Galvanostatic charge-discharge profiles of Sn_4P_3/GT for the 1st, 2nd, 5th, 50th, 250th and 500th cycles (0.01-2 V *vs.* Na/Na^+, 0.5 A g^{-1}); (B) Cycling performances (charge/discharge) of the Sn_4P_3/GT electrode and bare Sn_4P_3 electrode at a current density of 0.5 A g^{-1} for 500 cycles.

The rate capability of Sn_4P_3/GT electrodes was evaluated at various charge-discharge current densities, as shown in Figure 5.6 (A). With increasing current density, the Sn_4P_3/GT electrode displays capacities of 821, 722, 636, 547, 435 and 386 mA h g^{-1} at the current densities of 0.2, 0.5, 1, 2, 5, and 10 A g^{-1}, respectively. Remarkably, even at a high current density of 20 A g^{-1}, the electrode still provides a stable capacity of 326 mA g h^{-1}, indicating that confining the nano-sized Sn_4P_3 particles within highly conductive graphene tube networks does enable effective charge transport and electrochemical reactions. Upon reducing the current density to an initial value of 0.5 A g^{-1}, the electrode provides a specific capacity of 808 mA h g^{-1}, which is near completely recovered. Note that the capacity of Sn_4P_3/GT may be contributed by both the Sn_4P_3 nanoparticles and graphene tubes. Further study in Figure 5.6 (B) shows that a GT electrode displays a capacity of 362, 332, 310, 271, 218, 139 and 42 mA h g^{-1} at the current density of 0.2, 0.5, 1, 2, 5, 10 and 20 A g^{-1} under same voltage window, respectively.

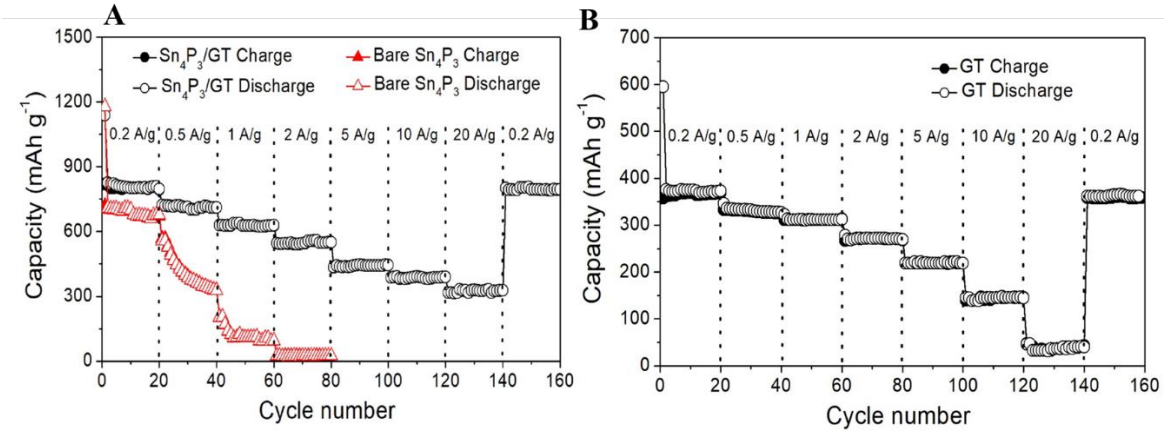

Figure 5.6 (A) Rate capability of Sn_4P_3/GT electrode and bare Sn_4P_3 electrode evaluated under various charge/discharge current densities; (B) Rate capability of GT electrode under different charge/discharge current densities.

To further study the performances of bare Sn_4P_3 and Sn_4P_3/GT electrode, electrochemical impedance spectroscopy (EIS) was employed in the frequency range of 0.01 Hz-10 MHz with

a perturbation amplitude of 10 mV. Figure 5.7 shows a representative Nyquist plot of a Sn_4P_3/GT electrode charged to 2.0 V. Comparable to bare Sn_4P_3 electrode, Sn_4P_3/GT electrode shows a smaller diameter of semicircle, indicating a lower interfacial resistance, which should be associated with a lower charge transfer and SEI passivation film resistance.[327] The inset of Figure 5.7 plots the real part of ω-1/2 vs the impedance spectra (Zre) in the low-frequency zone. The diameter of semicircle in Figure 5.7 represents the charge-transfer resistance. It is obvious that the diameter of semicircle of Sn_4P_3/GT electrode is much smaller than bare Sn_4P_3 electrode, which suggests that Sn_4P_3/GT electrode has higher ion-diffusion rate and better kinetics during the sodiation/desodiation process.[328]

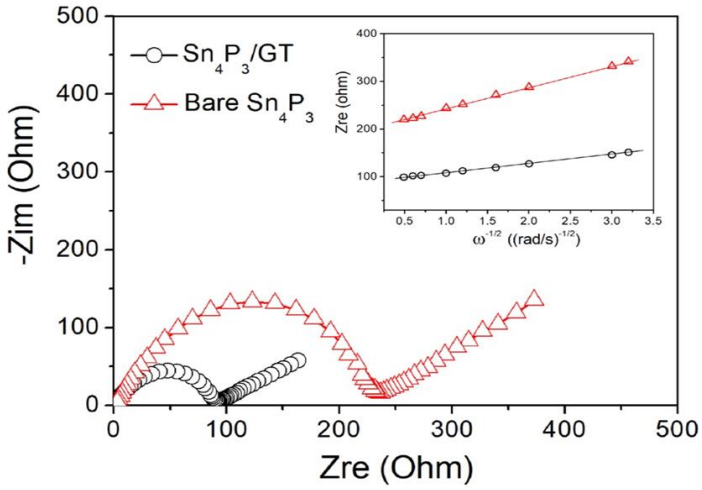

Figure 5.7 Nyquist plot of Sn_4P_3/GT electrode and bare Sn_4P_3 electrodes. Inset shows the relationship between the real part of the impedance spectra (Zre) and $\omega^{-1/2}$ (where ω is the angular frequency in the low-frequency region, $\omega=2\pi f$) in the low-frequency region.

Figure 5.8 further plots active-material utilization versus charge-discharge current density of the Sn_4P_3/GT and bare Sn_4P_3 electrodes. The utilizations are estimated by normalizing the specific capacity of the electrodes at different charge-discharge current densities (the slopes of the lines) *vs.* the specific capacity at 0.2 A g^{-1}. As shown, the active-material utilization

decreases with increasing charge-discharge current density, which is 88%, 77% and 67% for the Sn_4P_3/GT electrode and 79%, 28% and 3% for the bare Sn_4P_3 electrode at 0.5 A g^{-1}, 1 A g^{-1} and 2 A g^{-1}, respectively. To further assess the performance of the Sn_4P_3/GT electrodes, a comparison between the Sn_4P_3/GT electrode and other Sn_4P_3-based electrodes is also provided in Table 5.1. The significant improvement of active-material utilization in Sn_4P_3/GT electrodes, particularly at high current density, is consistent with the improved electrical conductivity of the composite electrode.

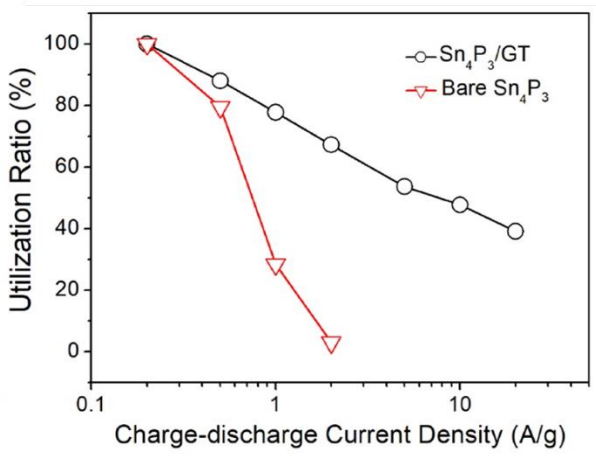

Figure 5.8 Utilization of the active material of the Sn_4P_3/GT electrode and bare Sn_4P_3 electrode at different charge-discharge current densities. The capacities shows are based on the total mass of the composite.

Materials	Current density (A g^{-1})	Capacity (mA h g^{-1})	Current density (A g^{-1})	Capacity (mA h g^{-1})	Cycles	Capacity retention	Ref
Sn_4P_3/C nanoparticle	0.05	850	1	349	120	86 %	[302]
Sn_4P_3@CNT/C	0.2	742	2	449	500	70%	[221]
"Sn_4P_3"/NHC	0.05	550	1	400	500	83%	[312]
Sn_4P_3/C powder	0.1	780	10	90	100	43 %	[313]
Sn_4P_3/SbSn	0.05	712	1	388	100	74 %	[315]
Sn_4P_3 nanoparticle	0.1	612	1	167	320	71 %	[316]
Sn_5SbP_3/C	0.1	602	2	351	200	65 %	[317]

composite							
Sn_4P_3@HC	0.1	430	1	312	400	88%	[318]
Sn_4P_3@C sphere	0.05	812	0.1	700	120	76 %	[319]
Sn_4P_3 nanotop	0.05	749	1	339	50	82 %	[320]
Sn_4P_3@C nanosphere	0.2	720	3	421	150	86 %	[222]
Sn_4P_3@C nanocube	0.1	701	2	508	500	55 %	[323]
Sn_4P_3/GT	**0.2**	**821**	**20**	**326**	**500**	**92 %**	**Our work**

Table 5.1 A comparison of the electrochemical performance representative Sn_4P_3 based anodes.

To further explore the underlying electrochemical process, structure evolution of Sn_4P_3/GT during discharging and charging was monitored by *ex situ* XRD. Figure 5.9 (A) and Figure 5.9 (B) shows the charging-discharging curves and XRD patterns at different states, respectively. The electrode shows a XRD pattern of Sn_4P_3 prior to reaction with sodium ions (*a*). When the electrode is discharged at 0.5 V (*b*), the characteristic peaks of Sn and Na_3P appears while the intensity of the Sn_4P_3 peaks decreases, indicating the conversion of Sn_4P_3 to Sn and Na_3P as described in Equation (1).[328] Upon discharging to 0.01 V (*c*), XRD suggests the presence of Na_3P and $Na_{15}Sn_4$, as well as vanishing of Sn_4P_3, as described in Equation (2). Up charging the electrode to 0.5 V (*d*), the electrode shows the characteristic peaks of Sn and Na_3P, corresponding to Equation (3). Further charging the electrode to 2.0 V (*e*), XRD shows intense Sn and less intense P peaks, corresponding Equation (4). The *ex situ* XRD results of Sn_4P_3/GT provide a possible explanation for mechanisms during the electrochemical process.

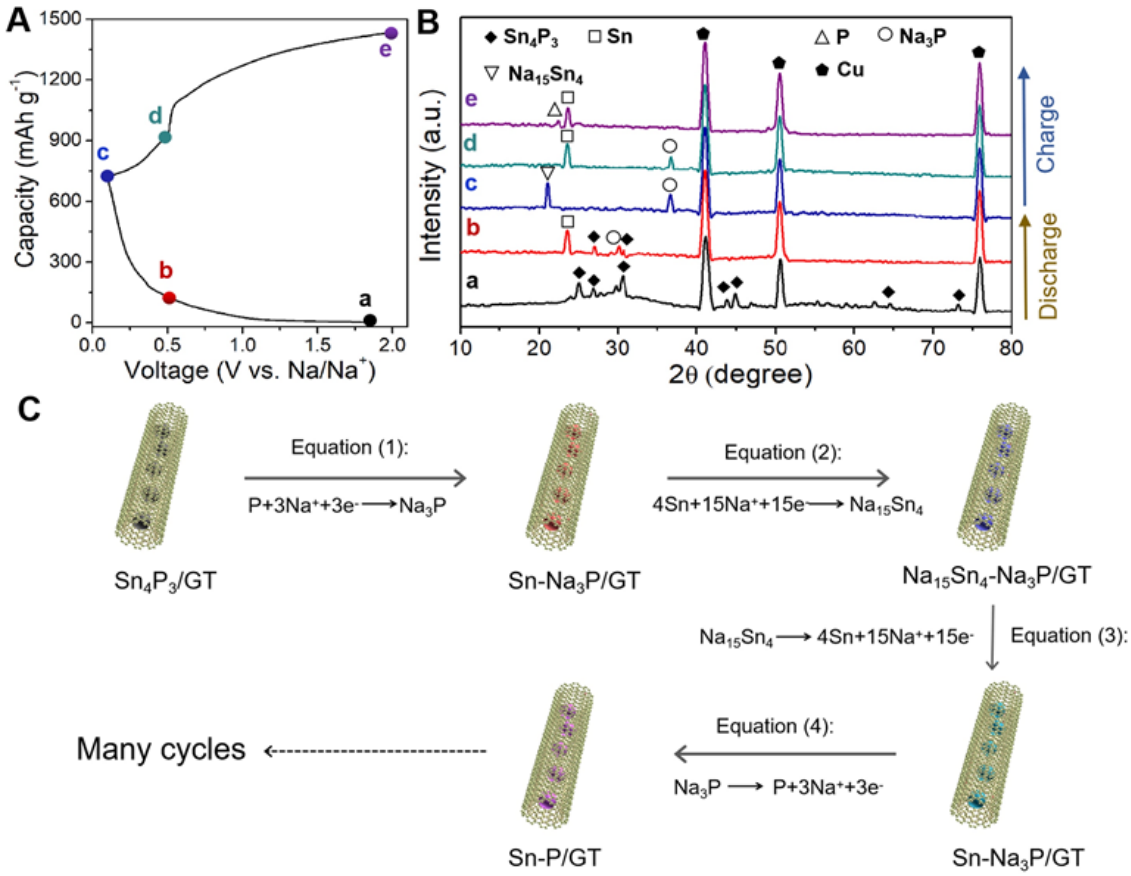

Figure 5.9 Ex situ by XRD characterization during a sodiation and desodiation cycle. (A) Specific capacities and (B) *ex* situ XRD patterns of Sn_4P_3/GT anode in discharge and charge processes of NIBs; (C) Schematic of the mechanism of the sodiation and desodiation in Sn_4P_3/GT anode.

The cycling stability of Sn_4P_3/GT electrodes was further examined using a high current density. Figure 5.10 (A) shows the sodium storage performance of the Sn_4P_3/GT electrode at 5 A g^{-1}, displaying a reversible capacity of 437 mA h g^{-1} and a capacity retention of ~ 92% from the 2nd cycle to 500th cycle. In contrast, bare Sn_4P_3 electrode in Figure 5.10 (E) exhibits rapid capacity fading after 50 cycles at 1 A g^{-1}. EIS measurement of the Sn_4P_3/GT electrode was also tested after the 1st, 5th, 50th, 250th and 500th cycles in Figure 5.10 (B). No obvious increase in resistance of Sn_4P_3/GT electrode was observed after the cycling, which indicates an excellent stability of the electrode. For further confirmation, TEM study was conducted for Sn_4P_3/GT

electrode cycled for 500 cycles in Figure 5.10 (C) (D), and it was found that the morphology and structural integrity of the Sn_4P_3/GT composite are well retained. Note that pulverization of the Sn_4P_3 nanoparticles may still occur to some extent during the cycling, resulting in the formation of nanoparticles with smaller size within the graphene tubes. Nevertheless, since such nanoparticles are still fully encapsulated inside the conductive graphene matrix, their electric contact with GT is well retained leading to the long cycling stability.

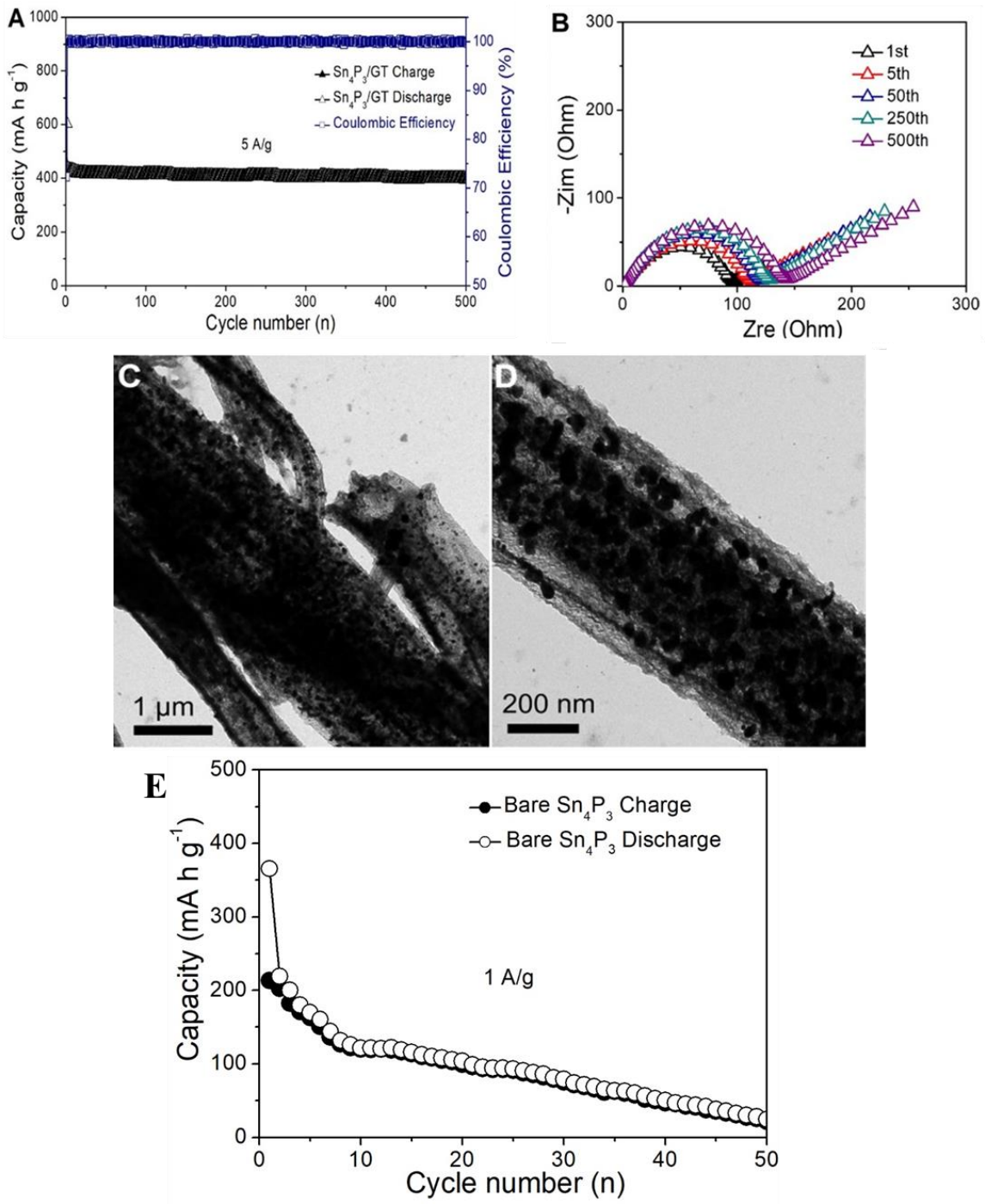

Figure 5.10 The cycling stability of the Sn_4P_3/GT electrodes. (A) Cycling stability of the Sn_4P_3/GT electrode at current density of 5 A g^{-1} for 500 cycles in the 0.01-2.0 V window (*vs.* Na/Na^+); (B) Nyquist plots of the Sn_4P_3/GT electrode after the 1st, 5th, 50th, 250th, and 500th cycles at a charging and discharging current density of 5 A g^{-1}; (C) (D) TEM images of Sn_4P_3/GT electrode after cycling for 500 cycles; (e) Cycling performance of the bare Sn_4P_3 electrode at 1 A g^{-1} for 50 cycles.

As shown in Table 5.1 and Figure 5.11, the electrochemical properties of Sn_4P_3/GT

electrodes are not only much better than that of bare Sn_4P_3 electrodes, but also show competitive characteristics over reported Sn_4P_3-based electrode materials. Compared to other Sn_4P_3-based electrodes, our Sn_4P_3/GT electrode has the capacity of 821 mA h g^{-1} at 0.2 A g^{-1} which is 14 % higher than the capacities of other electrodes under the same current density. Besides, the capacity of Sn_4P_3/GT electrode can maintain at 326 mA h g^{-1} at 20 A g^{-1} while the other Sn_4P_3-based electrodes can only reach similar capacities at 1 to 2 A g^{-1}. The capacity retention of Sn_4P_3/GT electrode is also much higher than the other Sn_4P_3-based electrodes, which is 92 % after 500 cycles. The extraordinary electrochemical performances of Sn_4P_3/GT electrode may be attributed to the unique architecture alleviating volume change of Sn_4P_3 nanoparticles using graphene tubes during the charging and discharging process. Meanwhile, multipoint physical contacts between the graphene tubes and Sn_4P_3 nanoparticles ensure their electrical conduction with accelerated kinetics of sodiation and desodiation.

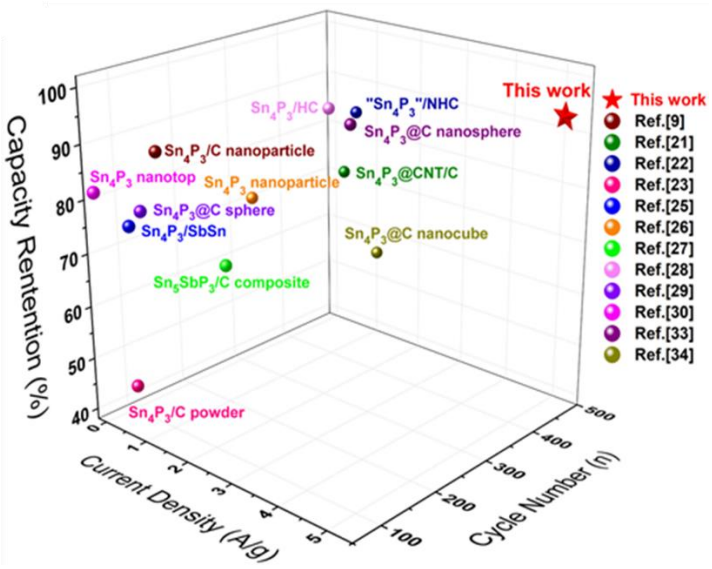

Figure 5.11 A comparison of the electrochemical performance metrics of Sn_4P_3/GT electrode with representative Sn_4P_3 based anodes reported.

5.4 Conclusion

In conclusion, we have successfully developed anodes based on Sn_4P_3 encapsulated within amphiphilic GT, which afford robust mechanical strength, effective charge transport, and ability to accommodate large volume change of Sn_4P_3 during cycling. Such anodes provide high capacity, rate performance and cycling durability. Such a strategy can be readily extended to other conversion- and alloying-type materials that are suffered from a dramatic volume change during electrochemical reactions.

Chapter 6 Conclusion of dissertation

In this dissertation, we have developed three different types of graphene-alloy composites to address current challenges for alloy anodes in lithium-ion and sodium-ion batteries, as well as broaden the avenues for the structural design of high energy densities anode materials in electrochemical energy storage system.

First, we tried to synthesize a hierarchical flower-like graphene tube/Sn (Sn/FGT) composite to apply as the anode for lithium-ion battery. This hierarchical flower-like tube structure enables fast charge transfer with shortened diffusion pathways, and functions as a buffer for the drastic volume change of Sn nanoparticles with its porous surface. The Sn/FGT anode can deliver a high reversible capacity of 742 mA h g^{-1}, excellent rate capability (211 mA h g^{-1} at 8 A g^{-1} with 99% capacity retention when the current density is back to 0.2 A g^{-1}).

Second, we designed a graphene tube-Sn composite (Sn/DGT), where Sn nanoparticles can be confined within the biphilic graphene tubes. Despite the severe volume expansion caused by Sn nanoparticles, the Sn/DGT anode can exhibit a high reversible capacity of 918 mA h g^{-1}, long cycling stability (>95% reversible capacity retention after 500 cycles) and excellent rate performance (402 mA h g^{-1} at current density 20 A g^{-1}). The small size of Sn nanoparticles shortens their ion-diffusion pathways and alleviates the mechanical stress during the alloying/dealloying process, while the robust graphene tubes provide buffer for the drastic volume change and fabricate a highly conductive network to retain the electrical contacts with active materials during the cycling.

Last but not least, we fabricated a high-performance sodium-ion anode through confined growth of Sn_4P_3 nanoparticles within amphiphilic graphene tubes, which provides mechanical

robustness, ability to confine Sn_4P_3 particles with the highly conductive frameworks, and the capability to accommodate the volume change of the particles during cycling. This unique structure endows sodium-ion anode with high reversible capacity (821 mA h g^{-1}), excellent rate capability (326 mA h g^{-1} at 20 A g^{-1}) and cycling stability (>90% reversible capacity retention after 500 cycles).

We hope the work of this dissertation could provide possible solutions to tackle with current issues from alloy-based anodes in lithium-ion and sodium-ion batteries, and broaden the structural design of composite materials in energy storage. The confined growth of tin or tin alloy particles within graphene scaffolds can provide highly conductive networks to retain the electrical contacts with active materials to enable prolonged cycling life, and facilitate the charge transport to improve the rate performance of the anodes. Tin and tin alloy particles with high volumetric capacities can afford the anodes with high volumetric energy densities for lithium and sodium storage.

Chapter 7 Reference

1. Aneke, M.; Wang, M., Energy storage technologies and real life applications–A state of the art review. *Applied Energy* **2016,** *179*, 350-377.

2. Øvergaard, S., Issue paper: Definition of primary and secondary energy. *Statistics Norway, Oslo* **2008**.

3. Ellabban, O.; Abu-Rub, H.; Blaabjerg, F., Renewable energy resources: Current status, future prospects and their enabling technology. *Renewable and Sustainable Energy Reviews* **2014,** *39*, 748-764.

4. Larcher, D.; Tarascon, J.-M., Towards greener and more sustainable batteries for electrical energy storage. *Nature chemistry* **2015,** *7* (1), 19.

5. Mahmoud, M.; Ramadan, M.; Olabi, A.-G.; Pullen, K.; Naher, S., A review of mechanical energy storage systems combined with wind and solar applications. *Energy Conversion and Management* **2020,** *210*, 112670.

6. Ibrahim, H.; Ilinca, A.; Perron, J., Energy storage systems—Characteristics and comparisons. *Renewable and sustainable energy reviews* **2008,** *12* (5), 1221-1250.

7. Liu, C.; Li, F.; Ma, L. P.; Cheng, H. M., Advanced materials for energy storage. *Advanced materials* **2010,** *22* (8), E28-E62.

8. Barton, J. P.; Infield, D. G., Energy storage and its use with intermittent renewable energy. *IEEE transactions on energy conversion* **2004,** *19* (2), 441-448.

9. Saito, A., Recent advances in research on cold thermal energy storage. *International Journal of Refrigeration* **2002,** *25* (2), 177-189.

10. Pena-Alzola, R.; Sebastián, R.; Quesada, J.; Colmenar, A. In *Review of flywheel based energy storage systems*, 2011 International Conference on Power Engineering, Energy and Electrical Drives, IEEE: 2011; pp 1-6.

11. Succar, S.; Williams, R. H., Compressed air energy storage: theory, resources, and applications for wind power. *Princeton environmental institute report* **2008,** *8*, 81.

12. Bullough, C.; Gatzen, C.; Jakiel, C.; Koller, M.; Nowi, A.; Zunft, S. In *Advanced adiabatic compressed air energy storage for the integration of wind energy*, Proceedings of the European wind energy conference, EWEC, Citeseer: 2004; p 25.

13. Cavallo, A., Controllable and affordable utility-scale electricity from intermittent wind resources and compressed air energy storage (CAES). *Energy* **2007,** *32* (2), 120-127.

14. Dincer, I.; Rosen, M. A., *Thermal energy storage systems and applications*. John Wiley & Sons: 2021.

15. Alva, G.; Lin, Y.; Fang, G., An overview of thermal energy storage systems. *Energy* **2018,** *144*, 341-378.

16. Sharma, A.; Tyagi, V. V.; Chen, C.; Buddhi, D., Review on thermal energy storage with phase change materials and applications. *Renewable and Sustainable energy reviews* **2009,** *13* (2), 318-345.

17. Sarbu, I.; Sebarchievici, C., A comprehensive review of thermal energy storage.

Sustainability **2018,** *10* (1), 191.

18. Hasnain, S., Review on sustainable thermal energy storage technologies, Part I: heat storage materials and techniques. *Energy conversion and management* **1998,** *39* (11), 1127-1138.

19. Denholm, P.; King, J. C.; Kutcher, C. F.; Wilson, P. P., Decarbonizing the electric sector: Combining renewable and nuclear energy using thermal storage. *Energy Policy* **2012,** *44*, 301-311.

20. Garg, P.; Orosz, M. S.; Kumar, P., Thermo-economic evaluation of ORCs for various working fluids. *Applied Thermal Engineering* **2016,** *109*, 841-853.

21. Cetin, T. H.; Kanoglu, M.; Yanikomer, N., Cryogenic energy storage powered by geothermal energy. *Geothermics* **2019,** *77*, 34-40.

22. Guney, M. S.; Tepe, Y., Classification and assessment of energy storage systems. *Renewable and Sustainable Energy Reviews* **2017,** *75*, 1187-1197.

23. Züttel, A., Hydrogen storage methods. *Naturwissenschaften* **2004,** *91* (4), 157-172.

24. Züttel, A., Materials for hydrogen storage. *Materials today* **2003,** *6* (9), 24-33.

25. Jena, P., Materials for hydrogen storage: past, present, and future. *The Journal of Physical Chemistry Letters* **2011,** *2* (3), 206-211.

26. Graetz, J., New approaches to hydrogen storage. *Chemical Society Reviews* **2009,** *38* (1), 73-82.

27. Zhou, L., Progress and problems in hydrogen storage methods. *Renewable and Sustainable*

Energy Reviews **2005,** *9* (4), 395-408.

28. Veziroglu, T. N., 21st Century's energy: Hydrogen energy system. In *Assessment of hydrogen energy for sustainable development*, Springer: 2007; pp 9-31.

29. Lee, D.-H., Toward the clean production of hydrogen: Competition among renewable energy sources and nuclear power. *International Journal of Hydrogen Energy* **2012,** *37* (20), 15726-15735.

30. Minutillo, M.; Perna, A., Renewable energy storage system via coal hydrogasification with co-production of electricity and synthetic natural gas. *International journal of hydrogen energy* **2014,** *39* (11), 5793-5803.

31. Jensen, S. H.; Larsen, P. H.; Mogensen, M., Hydrogen and synthetic fuel production from renewable energy sources. *International Journal of Hydrogen Energy* **2007,** *32* (15), 3253-3257.

32. Kleperis, J.; Fylenko, V.; Vanags, M.; Volkovs, A.; Lesnicenoks, P.; Grinberga, L.; Solovey, V., Energy storage solutions for small and medium-sized self-sufficient alternative energy objects. *Kleperis, VV Fylenko, M. Vanags, A. Volkovs, P. Lesnicenoks, L. Grinberga, VV Solovey//Bulgarian Chemical Communications.–Sofia: Bulgarian Academy of Sciences, Union of Chemists in Bulgaria* **2016,** *48*, 290-296.

33. Samavati, M.; Martin, A.; Santarelli, M.; Nemanova, V., Synthetic diesel production as a form of renewable energy storage. *Energies* **2018,** *11* (5), 1223.

34. Shah, Y. T., *Chemical energy from natural and synthetic gas*. CRC Press: 2017.

35. Dunn, B.; Kamath, H.; Tarascon, J.-M., Electrical energy storage for the grid: a battery of choices. *Science* **2011,** *334* (6058), 928-935.

36. Chen, H.; Cong, T. N.; Yang, W.; Tan, C.; Li, Y.; Ding, Y., Progress in electrical energy storage system: A critical review. *Progress in natural science* **2009,** *19* (3), 291-312.

37. Gür, T. M., Review of electrical energy storage technologies, materials and systems: challenges and prospects for large-scale grid storage. *Energy & Environmental Science* **2018,** *11* (10), 2696-2767.

38. Pavlov, D., *Lead-acid batteries: science and technology*. Elsevier: 2011.

39. Ruetschi, P., Review on the lead—acid battery science and technology. *Journal of Power Sources* **1977,** *2* (1), 3-120.

40. Jung, J.; Zhang, L.; Zhang, J., *Lead-acid battery technologies: fundamentals, materials, and applications*. Crc Press: 2015; Vol. 8.

41. Bullock, K. R., Lead/acid batteries. *Journal of power sources* **1994,** *51* (1-2), 1-17.

42. Bode, H., Lead-acid batteries. **1977**.

43. Hameer, S.; van Niekerk, J. L., A review of large-scale electrical energy storage. *International journal of energy research* **2015,** *39* (9), 1179-1195.

44. Huang, K.; Li, J.; Xu, Z., Characterization and recycling of cadmium from waste nickel–cadmium batteries. *Waste management* **2010,** *30* (11), 2292-2298.

45. Zhu, N.; Zhang, L.; Li, C.; Cai, C., Recycling of spent nickel–cadmium batteries based on bioleaching process. *Waste Management* **2003,** *23* (8), 703-708.

46. Rydh, C. J.; Karlström, M., Life cycle inventory of recycling portable nickel–cadmium batteries. *Resources, Conservation and Recycling* **2002,** *34* (4), 289-309.

47. Geng, M.; Northwood, D., Development of advanced rechargeable Ni/MH and Ni/Zn batteries. *International Journal of Hydrogen Energy* **2003,** *28* (6), 633-636.

48. Fetcenko, M.; Ovshinsky, S.; Reichman, B.; Young, K.; Fierro, C.; Koch, J.; Zallen, A.; Mays, W.; Ouchi, T., Recent advances in NiMH battery technology. *Journal of Power Sources* **2007,** *165* (2), 544-551.

49. Zhu, W. H.; Zhu, Y.; Davis, Z.; Tatarchuk, B. J., Energy efficiency and capacity retention of Ni–MH batteries for storage applications. *Applied Energy* **2013,** *106*, 307-313.

50. Liu, Y.; Pan, H.; Gao, M.; Wang, Q., Advanced hydrogen storage alloys for Ni/MH rechargeable batteries. *Journal of Materials Chemistry* **2011,** *21* (13), 4743-4755.

51. Wen, Z.; Cao, J.; Gu, Z.; Xu, X.; Zhang, F.; Lin, Z., Research on sodium sulfur battery for energy storage. *Solid State Ionics* **2008,** *179* (27-32), 1697-1701.

52. Xin, S.; Yin, Y. X.; Guo, Y. G.; Wan, L. J., A high-energy room-temperature sodium-sulfur battery. *Advanced Materials* **2014,** *26* (8), 1261-1265.

53. Xu, X.; Zhou, D.; Qin, X.; Lin, K.; Kang, F.; Li, B.; Shanmukaraj, D.; Rojo, T.; Armand, M.; Wang, G., A room-temperature sodium–sulfur battery with high capacity and stable cycling performance. *Nature communications* **2018,** *9* (1), 1-12.

54. Bito, A. In *Overview of the sodium-sulfur battery for the IEEE Stationary Battery Committee*, IEEE Power Engineering Society General Meeting, 2005, IEEE: 2005; pp 1232-

1235.

55. Linden, D. In *Handbook of batteries*, Fuel and energy abstracts, 1995; p 265.

56. Wachsman, E. D.; Lee, K. T., Lowering the temperature of solid oxide fuel cells. *Science* **2011,** *334* (6058), 935-939.

57. Lee, J. S.; Tai Kim, S.; Cao, R.; Choi, N. S.; Liu, M.; Lee, K. T.; Cho, J., Metal–air batteries with high energy density: Li–air versus Zn–air. *Advanced Energy Materials* **2011,** *1* (1), 34-50.

58. Park, J.; Park, M.; Nam, G.; Lee, J. s.; Cho, J., All-solid-state cable-type flexible zinc–air battery. *Advanced Materials* **2015,** *27* (8), 1396-1401.

59. Xu, M.; Ivey, D.; Xie, Z.; Qu, W., Rechargeable Zn-air batteries: Progress in electrolyte development and cell configuration advancement. *Journal of Power Sources* **2015,** *283*, 358-371.

60. Pan, J.; Xu, Y. Y.; Yang, H.; Dong, Z.; Liu, H.; Xia, B. Y., Advanced architectures and relatives of air electrodes in Zn–air batteries. *Advanced Science* **2018,** *5* (4), 1700691.

61. Pei, P.; Wang, K.; Ma, Z., Technologies for extending zinc–air battery's cyclelife: A review. *Applied Energy* **2014,** *128*, 315-324.

62. Yamin, H.; Gorenshtein, A.; Penciner, J.; Sternberg, Y.; Peled, E., Lithium sulfur battery: oxidation/reduction mechanisms of polysulfides in THF solutions. *Journal of the Electrochemical Society* **1988,** *135* (5), 1045.

63. Evers, S.; Nazar, L. F., New approaches for high energy density lithium–sulfur battery cathodes. *Accounts of chemical research* **2013,** *46* (5), 1135-1143.

64. Hu, Y.; Chen, W.; Lei, T.; Jiao, Y.; Huang, J.; Hu, A.; Gong, C.; Yan, C.; Wang, X.; Xiong, J., Strategies toward high-loading lithium–sulfur battery. *Advanced Energy Materials* **2020,** *10* (17), 2000082.

65. Kim, J.; Lee, D. J.; Jung, H. G.; Sun, Y. K.; Hassoun, J.; Scrosati, B., An Advanced Lithium-Sulfur Battery. *Advanced Functional Materials* **2013,** *23* (8), 1076-1080.

66. Zhang, S. S., Liquid electrolyte lithium/sulfur battery: Fundamental chemistry, problems, and solutions. *Journal of Power Sources* **2013,** *231*, 153-162.

67. Li, T.; Bai, X.; Gulzar, U.; Bai, Y. J.; Capiglia, C.; Deng, W.; Zhou, X.; Liu, Z.; Feng, Z.; Proietti Zaccaria, R., A comprehensive understanding of lithium–sulfur battery technology. *Advanced Functional Materials* **2019,** *29* (32), 1901730.

68. Papandrea, B.; Xu, X.; Xu, Y.; Chen, C.-Y.; Lin, Z.; Wang, G.; Luo, Y.; Liu, M.; Huang, Y.; Mai, L., Three-dimensional graphene framework with ultra-high sulfur content for a robust lithium–sulfur battery. *Nano research* **2016,** *9* (1), 240-248.

69. Liu, F.; Sun, G.; Wu, H. B.; Chen, G.; Xu, D.; Mo, R.; Shen, L.; Li, X.; Ma, S.; Tao, R., Dual redox mediators accelerate the electrochemical kinetics of lithium-sulfur batteries. *Nature communications* **2020,** *11* (1), 1-10.

70. De las Casas, C.; Li, W., A review of application of carbon nanotubes for lithium ion battery anode material. *Journal of Power Sources* **2012,** *208*, 74-85.

71. Yoshio, M.; Brodd, R. J.; Kozawa, A., *Lithium-ion batteries*. Springer: 2009; Vol. 1.

72. Manthiram, A., An outlook on lithium ion battery technology. *ACS central science* **2017,**

3 (10), 1063-1069.

73. Vaalma, C.; Buchholz, D.; Weil, M.; Passerini, S., A cost and resource analysis of sodium-ion batteries. *Nature reviews materials* **2018,** *3* (4), 1-11.

74. Zhang, W.; Zhang, F.; Ming, F.; Alshareef, H. N., Sodium-ion battery anodes: Status and future trends. *EnergyChem* **2019,** *1* (2), 100012.

75. Bauer, A.; Song, J.; Vail, S.; Pan, W.; Barker, J.; Lu, Y., The scale-up and commercialization of nonaqueous Na-ion battery technologies. *Advanced Energy Materials* **2018,** *8* (17), 1702869.

76. Dai, Z.; Mani, U.; Tan, H. T.; Yan, Q., Advanced Cathode Materials for Sodium-Ion Batteries: What Determines Our Choices? *Small Methods* **2017,** *1* (5), 1700098.

77. Saikia, K.; Kakati, B. K.; Boro, B.; Verma, A., Current Advances and Applications of Fuel Cell Technologies. In *Recent Advancements in Biofuels and Bioenergy Utilization*, Springer: 2018; pp 303-337.

78. Brandon, N.; Kurban, Z., Clean energy and the hydrogen economy. *Philosophical Transactions of the Royal Society A: Mathematical, Physical and Engineering Sciences* **2017,** *375* (2098), 20160400.

79. Hanley, E. S.; Deane, J.; Gallachóir, B. Ó., The role of hydrogen in low carbon energy futures–A review of existing perspectives. *Renewable and Sustainable Energy Reviews* **2018,** *82*, 3027-3045.

80. Da Silva, F. S.; de Souza, T. M., Novel materials for solid oxide fuel cell technologies: A

literature review. *international journal of hydrogen energy* **2017,** *42* (41), 26020-26036.

81. Daud, W.; Rosli, R.; Majlan, E.; Hamid, S.; Mohamed, R.; Husaini, T., PEM fuel cell system control: A review. *Renewable Energy* **2017,** *113*, 620-638.

82. Sharma, K.; Arora, A.; Tripathi, S. K., Review of supercapacitors: Materials and devices. *Journal of Energy Storage* **2019,** *21*, 801-825.

83. Zhi, M.; Xiang, C.; Li, J.; Li, M.; Wu, N., Nanostructured carbon–metal oxide composite electrodes for supercapacitors: a review. *Nanoscale* **2013,** *5* (1), 72-88.

84. Nikolaidis, P.; Poullikkas, A., A comparative review of electrical energy storage systems for better sustainability. *Journal of power technologies* **2017**.

85. Wang, Y.; Zhang, L.; Hou, H.; Xu, W.; Duan, G.; He, S.; Liu, K.; Jiang, S., Recent progress in carbon-based materials for supercapacitor electrodes: a review. *Journal of Materials Science* **2021,** *56* (1), 173-200.

86. Borenstein, A.; Hanna, O.; Attias, R.; Luski, S.; Brousse, T.; Aurbach, D., Carbon-based composite materials for supercapacitor electrodes: a review. *Journal of Materials Chemistry A* **2017,** *5* (25), 12653-12672.

87. Zhang, L.; Hu, X.; Wang, Z.; Sun, F.; Dorrell, D. G., A review of supercapacitor modeling, estimation, and applications: A control/management perspective. *Renewable and Sustainable Energy Reviews* **2018,** *81*, 1868-1878.

88. Tomaszewska, A.; Chu, Z.; Feng, X.; O'Kane, S.; Liu, X.; Chen, J.; Ji, C.; Endler, E.; Li, R.; Liu, L., Lithium-ion battery fast charging: A review. *ETransportation* **2019,** *1*, 100011.

89. Han, X.; Lu, L.; Zheng, Y.; Feng, X.; Li, Z.; Li, J.; Ouyang, M., A review on the key issues of the lithium ion battery degradation among the whole life cycle. *ETransportation* **2019,** *1*, 100005.

90. Wang, Q.; Mao, B.; Stoliarov, S. I.; Sun, J., A review of lithium ion battery failure mechanisms and fire prevention strategies. *Progress in Energy and Combustion Science* **2019,** *73*, 95-131.

91. Winter, M.; Besenhard, J. O.; Spahr, M. E.; Novak, P., Insertion electrode materials for rechargeable lithium batteries. *Advanced materials* **1998,** *10* (10), 725-763.

92. Trucano, P.; Chen, R., Structure of graphite by neutron diffraction. *Nature* **1975,** *258* (5531), 136-137.

93. Fukushima, H.; Drzal, L.; Rook, B.; Rich, M., Thermal conductivity of exfoliated graphite nanocomposites. *Journal of thermal analysis and calorimetry* **2006,** *85* (1), 235-238.

94. Agarwal, R. R.; Selman, J. R., Electrochemical Intercalation of Lithium in Graphite Using a Molten-Salt Cell. *ECS Proceedings Volumes* **1986,** *1986*, 377-388.

95. Huggins, R. A., Use of Polymeric Materials As Battery Components. *Advanced Batteries: Materials Science Aspects* **2009**, 433-440.

96. Kumar, T. P.; Kumari, T. S. D.; Stephan, M. A., Carbonaceous anode materials for lithium-ion batteries–the road ahead. *Journal of the Indian Institute of Science* **2009,** *89* (4), 393-424.

97. Ding, F.; Xu, W.; Choi, D.; Wang, W.; Li, X.; Engelhard, M. H.; Chen, X.; Yang, Z.; Zhang, J.-G., Enhanced performance of graphite anode materials by AlF 3 coating for lithium-ion

batteries. *Journal of Materials Chemistry* **2012,** *22* (25), 12745-12751.

98. Cheng, Q.; Yuge, R.; Nakahara, K.; Tamura, N.; Miyamoto, S., KOH etched graphite for fast chargeable lithium-ion batteries. *Journal of Power Sources* **2015,** *284*, 258-263.

99. Kim, D. S.; Chung, D. J.; Bae, J.; Jeong, G.; Kim, H., Surface engineering of graphite anode material with black TiO2-x for fast chargeable lithium ion battery. *Electrochimica Acta* **2017,** *258*, 336-342.

100. Azuma, H.; Imoto, H.; Yamada, S. i.; Sekai, K., Advanced carbon anode materials for lithium ion cells. *Journal of power sources* **1999,** *81*, 1-7.

101. Ni, J.; Huang, Y.; Gao, L., A high-performance hard carbon for Li-ion batteries and supercapacitors application. *Journal of Power Sources* **2013,** *223*, 306-311.

102. Hu, J.; Li, H.; Huang, X., Electrochemical behavior and microstructure variation of hard carbon nano-spherules as anode material for Li-ion batteries. *Solid State Ionics* **2007,** *178* (3-4), 265-271.

103. Fujimoto, H.; Tokumitsu, K.; Mabuchi, A.; Chinnasamy, N.; Kasuh, T., The anode performance of the hard carbon for the lithium ion battery derived from the oxygen-containing aromatic precursors. *Journal of Power Sources* **2010,** *195* (21), 7452-7456.

104. Jafari, S. M.; Khosravi, M.; Mollazadeh, M., Nanoporous hard carbon microspheres as anode active material of lithium ion battery. *Electrochimica Acta* **2016,** *203*, 9-20.

105. Kim, K.-J.; Lee, T.-S.; Kim, H.-G.; Lim, S.-H.; Lee, S.-M., A hard carbon/microcrystalline graphite/carbon composite with a core-shell structure as novel anode

materials for lithium-ion batteries. *Electrochimica Acta* **2014,** *135*, 27-34.

106. Dai, H., Carbon nanotubes: opportunities and challenges. *Surface Science* **2002,** *500* (1-3), 218-241.

107. Landi, B. J.; Ganter, M. J.; Cress, C. D.; DiLeo, R. A.; Raffaelle, R. P., Carbon nanotubes for lithium ion batteries. *Energy & Environmental Science* **2009,** *2* (6), 638-654.

108. Ando, Y.; Zhao, X.; Shimoyama, H.; Sakai, G.; Kaneto, K., Physical properties of multiwalled carbon nanotubes. *International journal of inorganic materials* **1999,** *1* (1), 77-82.

109. Yu, M.-F.; Lourie, O.; Dyer, M. J.; Moloni, K.; Kelly, T. F.; Ruoff, R. S., Strength and breaking mechanism of multiwalled carbon nanotubes under tensile load. *Science* **2000,** *287* (5453), 637-640.

110. Sadri, R.; Ahmadi, G.; Togun, H.; Dahari, M.; Kazi, S. N.; Sadeghinezhad, E.; Zubir, N., An experimental study on thermal conductivity and viscosity of nanofluids containing carbon nanotubes. *Nanoscale research letters* **2014,** *9* (1), 1-16.

111. Landi, B. J.; Ganter, M. J.; Schauerman, C. M.; Cress, C. D.; Raffaelle, R. P., Lithium ion capacity of single wall carbon nanotube paper electrodes. *The Journal of Physical Chemistry C* **2008,** *112* (19), 7509-7515.

112. Lahiri, I.; Oh, S.-W.; Hwang, J. Y.; Cho, S.; Sun, Y.-K.; Banerjee, R.; Choi, W., High capacity and excellent stability of lithium ion battery anode using interface-controlled binder-free multiwall carbon nanotubes grown on copper. *ACS nano* **2010,** *4* (6), 3440-3446.

113. Ren, J.; Li, L.; Chen, C.; Chen, X.; Cai, Z.; Qiu, L.; Wang, Y.; Zhu, X.; Peng, H., Twisting

carbon nanotube fibers for both wire-shaped micro-supercapacitor and micro-battery. *Advanced Materials* **2013,** *25* (8), 1155-1159.

114.Di Lecce, D.; Andreotti, P.; Boni, M.; Gasparro, G.; Rizzati, G.; Hwang, J.-Y.; Sun, Y.-K.; Hassoun, J., Multiwalled carbon nanotubes anode in lithium-ion battery with LiCoO2, Li [Ni1/3Co1/3Mn1/3] O2, and LiFe1/4Mn1/2Co1/4PO4 cathodes. *ACS Sustainable Chemistry & Engineering* **2018,** *6* (3), 3225-3232.

115.Kang, C.; Patel, M.; Rangasamy, B.; Jung, K.-N.; Xia, C.; Shi, S.; Choi, W., Three-dimensional carbon nanotubes for high capacity lithium-ion batteries. *Journal of Power Sources* **2015,** *299*, 465-471.

116.Fang, R.; Chen, K.; Yin, L.; Sun, Z.; Li, F.; Cheng, H. M., The regulating role of carbon nanotubes and graphene in lithium-ion and lithium–sulfur batteries. *Advanced Materials* **2019,** *31* (9), 1800863.

117.Raccichini, R.; Varzi, A.; Passerini, S.; Scrosati, B., The role of graphene for electrochemical energy storage. *Nature materials* **2015,** *14* (3), 271-279.

118.Cui, L.-F.; Yang, Y.; Hsu, C.-M.; Cui, Y., Carbon− silicon core− shell nanowires as high capacity electrode for lithium ion batteries. *Nano letters* **2009,** *9* (9), 3370-3374.

119.Wu, Z.-S.; Zhou, G.; Yin, L.-C.; Ren, W.; Li, F.; Cheng, H.-M., Graphene/metal oxide composite electrode materials for energy storage. *Nano Energy* **2012,** *1* (1), 107-131.

120. Vinayan, B.; Nagar, R.; Raman, V.; Rajalakshmi, N.; Dhathathreyan, K.; Ramaprabhu, S., Synthesis of graphene-multiwalled carbon nanotubes hybrid nanostructure by strengthened electrostatic interaction and its lithium ion battery application. *Journal of Materials Chemistry*

2012, *22* (19), 9949-9956.

121. Park, J.; Moon, W. G.; Kim, G.-P.; Nam, I.; Park, S.; Kim, Y.; Yi, J., Three-dimensional aligned mesoporous carbon nanotubes filled with Co3O4 nanoparticles for Li-ion battery anode applications. *Electrochimica Acta* **2013,** *105*, 110-114.

122. Lian, P.; Zhu, X.; Liang, S.; Li, Z.; Yang, W.; Wang, H., Large reversible capacity of high quality graphene sheets as an anode material for lithium-ion batteries. *Electrochimica Acta* **2010,** *55* (12), 3909-3914.

123. Zdetsis, A. D.; Economou, E., A Pedestrian Approach to the Aromaticity of Graphene and Nanographene: Significance of Huckel's (4 n+ 2) π Electron Rule. *The Journal of Physical Chemistry C* **2015,** *119* (29), 16991-17003.

124. Geim, A. K.; Novoselov, K. S., The rise of graphene. In *Nanoscience and technology: a collection of reviews from nature journals*, World Scientific: 2010; pp 11-19.

125. Novoselov, K. S.; Geim, A. K.; Morozov, S. V.; Jiang, D.; Zhang, Y.; Dubonos, S. V.; Grigorieva, I. V.; Firsov, A. A., Electric field effect in atomically thin carbon films. *science* **2004,** *306* (5696), 666-669.

126. Mayorov, A. S.; Gorbachev, R. V.; Morozov, S. V.; Britnell, L.; Jalil, R.; Ponomarenko, L. A.; Blake, P.; Novoselov, K. S.; Watanabe, K.; Taniguchi, T., Micrometer-scale ballistic transport in encapsulated graphene at room temperature. *Nano letters* **2011,** *11* (6), 2396-2399.

127. Weiss, N. O.; Zhou, H.; Liao, L.; Liu, Y.; Jiang, S.; Huang, Y.; Duan, X., Graphene: an emerging electronic material. *Advanced materials* **2012,** *24* (43), 5782-5825.

128. Nair, R. R.; Blake, P.; Grigorenko, A. N.; Novoselov, K. S.; Booth, T. J.; Stauber, T.; Peres, N. M.; Geim, A. K., Fine structure constant defines visual transparency of graphene. *Science* **2008,** *320* (5881), 1308-1308.

129. Moser, J.; Barreiro, A.; Bachtold, A., Current-induced cleaning of graphene. *Applied Physics Letters* **2007,** *91* (16), 163513.

130. Bai, J.; Zhong, X.; Jiang, S.; Huang, Y.; Duan, X., Graphene nanomesh. *Nature nanotechnology* **2010,** *5* (3), 190-194.

131. Raccichini, R.; Varzi, A.; Passerini, S.; Scrosati, B., The role of graphene for electrochemical energy storage. *Nature materials* **2015,** *14* (3), 271.

132. Dahn, J. R.; Zheng, T.; Liu, Y.; Xue, J., Mechanisms for lithium insertion in carbonaceous materials. *Science* **1995,** *270* (5236), 590-593.

133. Yi, M.; Shen, Z., A review on mechanical exfoliation for the scalable production of graphene. *Journal of Materials Chemistry A* **2015,** *3* (22), 11700-11715.

134. Li, X.-s.; Cai, W.-w.; An, J.; Kim, S.; Nah, J., X. Li, W. Cai, J. An, S. Kim, J. Nah, D. Yang, R. Piner, A. Velamakanni, I. Jung, E. Tutuc, SK Banerjee, L. Colombo, and RS Ruoff, Science 324, 1312 (2009). *Science* **2009,** *324*, 1312.

135. Zhou, H.; Yu, W. J.; Liu, L.; Cheng, R.; Chen, Y.; Huang, X.; Liu, Y.; Wang, Y.; Huang, Y.; Duan, X., Chemical vapour deposition growth of large single crystals of monolayer and bilayer graphene. *Nature communications* **2013,** *4* (1), 1-8.

136. Stankovich, S.; Dikin, D. A.; Piner, R. D.; Kohlhaas, K. A.; Kleinhammes, A.; Jia, Y.;

Wu, Y.; Nguyen, S. T.; Ruoff, R. S., Synthesis of graphene-based nanosheets via chemical reduction of exfoliated graphite oxide. *carbon* **2007,** *45* (7), 1558-1565.

137. Cui, X.; Zhang, C.; Hao, R.; Hou, Y., Liquid-phase exfoliation, functionalization and applications of graphene. *Nanoscale* **2011,** *3* (5), 2118-2126.

138. Ohta, T.; Bostwick, A.; Seyller, T.; Horn, K.; Rotenberg, E., Controlling the electronic structure of bilayer graphene. *Science* **2006,** *313* (5789), 951-954.

139. Berger, C., C. Berger, Z. Song, T. Li, X. Li, AY Ogbazghi, R. Feng, Z. Dai, AN Marchenkov, EH Conrad, PN First, and WA de Heer, J. Phys. Chem. B 108, 19912 (2004). *J. Phys. Chem. B* **2004,** *108*, 19912.

140. Novoselov, K. S.; Fal, V.; Colombo, L.; Gellert, P.; Schwab, M.; Kim, K., A roadmap for graphene. *nature* **2012,** *490* (7419), 192-200.

141. Meyer, J. C.; Geim, A. K.; Katsnelson, M. I.; Novoselov, K. S.; Booth, T. J.; Roth, S., The structure of suspended graphene sheets. *Nature* **2007,** *446* (7131), 60-63.

142. Zhang, J.; Yu, Y.; Liu, L.; Wu, Y., Graphene–hollow PPy sphere 3D-nanoarchitecture with enhanced electrochemical performance. *Nanoscale* **2013,** *5* (7), 3052-3057.

143. Xu, Z.; Gao, C., Graphene fiber: a new trend in carbon fibers. *Materials Today* **2015,** *18* (9), 480-492.

144. Bai, J.; Cheng, R.; Xiu, F.; Liao, L.; Wang, M.; Shailos, A.; Wang, K. L.; Huang, Y.; Duan, X., Very large magnetoresistance in graphene nanoribbons. *Nature nanotechnology* **2010,** *5* (9), 655-659.

145. Chen, Z.; Xu, C.; Ma, C.; Ren, W.; Cheng, H. M., Lightweight and flexible graphene foam composites for high-performance electromagnetic interference shielding. *Advanced materials* **2013,** *25* (9), 1296-1300.

146. Zhang, X.; Sui, Z.; Xu, B.; Yue, S.; Luo, Y.; Zhan, W.; Liu, B., Mechanically strong and highly conductive graphene aerogel and its use as electrodes for electrochemical power sources. *Journal of Materials Chemistry* **2011,** *21* (18), 6494-6497.

147. Xu, Y.; Lin, Z.; Huang, X.; Wang, Y.; Huang, Y.; Duan, X., Functionalized graphene hydrogel-based high-performance supercapacitors. *Advanced materials* **2013,** *25* (40), 5779-5784.

148. Wang, G.; Shen, X.; Yao, J.; Park, J., Graphene nanosheets for enhanced lithium storage in lithium ion batteries. *Carbon* **2009,** *47* (8), 2049-2053.

149. Zhang, J.; Guo, B.; Yang, Y.; Shen, W.; Wang, Y.; Zhou, X.; Wu, H.; Guo, S., Large scale production of nanoporous graphene sheets and their application in lithium ion battery. *Carbon* **2015,** *84*, 469-478.

150. Cai, D.; Ding, L.; Wang, S.; Li, Z.; Zhu, M.; Wang, H., Facile synthesis of ultrathin-shell graphene hollow spheres for high-performance lithium-ion batteries. *Electrochimica Acta* **2014,** *139*, 96-103.

151. Yu, H.; Guo, G.; Ji, L.; Li, H.; Yang, D.; Hu, J.; Dong, A., Designed synthesis of ordered mesoporous graphene spheres from colloidal nanocrystals and their application as a platform for high-performance lithium-ion battery composite electrodes. *Nano Research* **2016,** *9* (12), 3757-3771.

152. Xu, Y.; Lin, Z.; Zhong, X.; Papandrea, B.; Huang, Y.; Duan, X., Solvated Graphene Frameworks as High-Performance Anodes for Lithium-Ion Batteries. *Angewandte Chemie* **2015,** *127* (18), 5435-5440.

153. Wang, R.; Xu, C.; Du, M.; Sun, J.; Gao, L.; Zhang, P.; Yao, H.; Lin, C., Solvothermal-Induced Self-Assembly of Fe2O3/GS Aerogels for High Li-Storage and Excellent Stability. *Small* **2014,** *10* (11), 2260-2269.

154. Yi, T.-F.; Liu, H.; Zhu, Y.-R.; Jiang, L.-J.; Xie, Y.; Zhu, R.-S., Improving the high rate performance of Li4Ti5O12 through divalent zinc substitution. *Journal of Power Sources* **2012,** *215*, 258-265.

155. Yang, Y.; Qiao, B.; Yang, X.; Fang, L.; Pan, C.; Song, W.; Hou, H.; Ji, X., Lithium titanate tailored by cathodically induced graphene for an ultrafast lithium ion battery. *Advanced Functional Materials* **2014,** *24* (27), 4349-4356.

156. Xu, W.; Chen, X.; Wang, W.; Choi, D.; Ding, F.; Zheng, J.; Nie, Z.; Choi, Y. J.; Zhang, J.-G.; Yang, Z. G., Simply AlF3-treated Li4Ti5O12 composite anode materials for stable and ultrahigh power lithium-ion batteries. *Journal of power sources* **2013,** *236*, 169-174.

157. Xie, Z.; Li, X.; Li, W.; Chen, M.; Qu, M., Graphene oxide/lithium titanate composite with binder-free as high capacity anode material for lithium-ion batteries. *Journal of Power Sources* **2015,** *273*, 754-760.

158. Jung, H.-G.; Myung, S.-T.; Yoon, C. S.; Son, S.-B.; Oh, K. H.; Amine, K.; Scrosati, B.; Sun, Y.-K., Microscale spherical carbon-coated Li 4 Ti 5 O 12 as ultra high power anode material for lithium batteries. *Energy & Environmental Science* **2011,** *4* (4), 1345-1351.

159. Zhang, W.-J., A review of the electrochemical performance of alloy anodes for lithium-ion batteries. *Journal of Power Sources* **2011,** *196* (1), 13-24.

160. Li, H.; Shi, L.; Wang, Q.; Chen, L.; Huang, X., Nano-alloy anode for lithium ion batteries. *Solid State Ionics* **2002,** *148* (3-4), 247-258.

161. Kasavajjula, U.; Wang, C.; Appleby, A. J., Nano-and bulk-silicon-based insertion anodes for lithium-ion secondary cells. *Journal of power sources* **2007,** *163* (2), 1003-1039.

162. Wu, H.; Cui, Y., Designing nanostructured Si anodes for high energy lithium ion batteries. *Nano today* **2012,** *7* (5), 414-429.

163. Chae, S.; Ko, M.; Kim, K.; Ahn, K.; Cho, J., Confronting issues of the practical implementation of Si anode in high-energy lithium-ion batteries. *Joule* **2017,** *1* (1), 47-60.

164. Wang, B.; Li, X.; Luo, B.; Zhang, X.; Shang, Y.; Cao, A.; Zhi, L., Intertwined network of Si/C nanocables and carbon nanotubes as lithium-ion battery anodes. *ACS applied materials & interfaces* **2013,** *5* (14), 6467-6472.

165. Wang, D.; Li, X.; Yang, J.; Wang, J.; Geng, D.; Li, R.; Cai, M.; Sham, T.-K.; Sun, X., Hierarchical nanostructured core–shell Sn@ C nanoparticles embedded in graphene nanosheets: spectroscopic view and their application in lithium ion batteries. *Physical Chemistry Chemical Physics* **2013,** *15* (10), 3535-3542.

166. Zhang, W. M.; Hu, J. S.; Guo, Y. G.; Zheng, S. F.; Zhong, L. S.; Song, W. G.; Wan, L. J., Tin-nanoparticles encapsulated in elastic hollow carbon spheres for high-performance anode material in lithium-Ion batteries. *Advanced Materials* **2008,** *20* (6), 1160-1165.

167. Wang, Z.; Zhou, L.; Lou, X. W., Metal oxide hollow nanostructures for lithium-ion batteries. Wiley Online Library: 2012.

168. Han, J.; Kong, D.; Lv, W.; Tang, D.-M.; Han, D.; Zhang, C.; Liu, D.; Xiao, Z.; Zhang, X.; Xiao, J., Caging tin oxide in three-dimensional graphene networks for superior volumetric lithium storage. *Nature communications* **2018,** *9* (1), 1-9.

169. Xin, X.; Zhou, X.; Wu, J.; Yao, X.; Liu, Z., Scalable synthesis of TiO2/graphene nanostructured composite with high-rate performance for lithium ion batteries. *ACS nano* **2012,** *6* (12), 11035-11043.

170. Sun, H.; Mei, L.; Liang, J.; Zhao, Z.; Lee, C.; Fei, H.; Ding, M.; Lau, J.; Li, M.; Wang, C., Three-dimensional holey-graphene/niobia composite architectures for ultrahigh-rate energy storage. *Science* **2017,** *356* (6338), 599-604.

171. Zhang, L.; Zhao, K.; Yu, R.; Yan, M.; Xu, W.; Dong, Y.; Ren, W.; Xu, X.; Tang, C.; Mai, L., Phosphorus enhanced intermolecular interactions of SnO2 and graphene as an ultrastable lithium battery anode. *Small* **2017,** *13* (20), 1603973.

172. Teng, Y.; Zhao, H.; Zhang, Z.; Li, Z.; Xia, Q.; Zhang, Y.; Zhao, L.; Du, X.; Du, Z.; Lv, P., MoS2 nanosheets vertically grown on graphene sheets for lithium-ion battery anodes. *ACS nano* **2016,** *10* (9), 8526-8535.

173. Choi, S. H.; Kang, Y. C., Fe3O4-decorated hollow graphene balls prepared by spray pyrolysis process for ultrafast and long cycle-life lithium ion batteries. *Carbon* **2014,** *79*, 58-66.

174. Luo, B.; Qiu, T.; Ye, D.; Wang, L.; Zhi, L., Tin nanoparticles encapsulated in graphene

backboned carbonaceous foams as high-performance anodes for lithium-ion and sodium-ion storage. *Nano Energy* **2016,** *22*, 232-240.

175. Mekonnen, Y.; Sundararajan, A.; Sarwat, A. I. In *A review of cathode and anode materials for lithium-ion batteries*, SoutheastCon 2016, IEEE: 2016; pp 1-6.

176. Mishra, A.; Mehta, A.; Basu, S.; Malode, S. J.; Shetti, N. P.; Shukla, S. S.; Nadagouda, M. N.; Aminabhavi, T. M., Electrode materials for lithium-ion batteries. *Materials Science for Energy Technologies* **2018,** *1* (2), 182-187.

177. Fergus, J. W., Recent developments in cathode materials for lithium ion batteries. *Journal of Power Sources* **2010,** *195* (4), 939-954.

178. Zheng, J.; Myeong, S.; Cho, W.; Yan, P.; Xiao, J.; Wang, C.; Cho, J.; Zhang, J. G., Li- and Mn-rich cathode materials: challenges to commercialization. *Advanced Energy Materials* **2017,** *7* (6), 1601284.

179. Lyu, Y.; Wu, X.; Wang, K.; Feng, Z.; Cheng, T.; Liu, Y.; Wang, M.; Chen, R.; Xu, L.; Zhou, J., An overview on the advances of LiCoO2 cathodes for lithium-ion batteries. *Advanced Energy Materials* **2021,** *11* (2), 2000982.

180. Lee, K.-S.; Myung, S.-T.; Kim, D.-W.; Sun, Y.-K., AlF3-coated LiCoO2 and Li [Ni1/3Co1/3Mn1/3] O2 blend composite cathode for lithium ion batteries. *Journal of Power Sources* **2011,** *196* (16), 6974-6977.

181. Sun, Y.; Dong, H.; Wu, K.; Chen, X.; Wang, S.; Gu, W.; Hong, Z.; Liu, M.; Shen, Y.; Lu, W., Graphene quantum dots coated LiCoO2 for improved cycling stability and thermal safety at high voltage. *Journal of Electroanalytical Chemistry* **2020,** *866*, 114109.

182. Momma, K.; Izumi, F., VESTA 3 for three-dimensional visualization of crystal, volumetric and morphology data. *Journal of applied crystallography* **2011,** *44* (6), 1272-1276.

183. Kucinskis, G.; Bajars, G.; Kleperis, J., Graphene in lithium ion battery cathode materials: A review. *Journal of Power Sources* **2013,** *240*, 66-79.

184. Hummel, R. E., *Electronic properties of materials*. Springer Science & Business Media: 2011.

185. Xie, H. M.; Wang, R. S.; Ying, J. R.; Zhang, L. Y.; Jalbout, A. F.; Yu, H. Y.; Yang, G. L.; Pan, X. M.; Su, Z. M., Optimized LiFePO4–polyacene cathode material for lithium-ion batteries. *Advanced Materials* **2006,** *18* (19), 2609-2613.

186. Li, X.; Kang, F.; Bai, X.; Shen, W., A novel network composite cathode of LiFePO4/multiwalled carbon nanotubes with high rate capability for lithium ion batteries. *Electrochemistry Communications* **2007,** *9* (4), 663-666.

187. Wang, L.; Wang, H.; Liu, Z.; Xiao, C.; Dong, S.; Han, P.; Zhang, Z.; Zhang, X.; Bi, C.; Cui, G., A facile method of preparing mixed conducting LiFePO4/graphene composites for lithium-ion batteries. *Solid State Ionics* **2010,** *181* (37-38), 1685-1689.

188. Andersson, A.; Thomas, J. O., The source of first-cycle capacity loss in LiFePO4. *Journal of Power Sources* **2001,** *97*, 498-502.

189. Thackeray, M.; Johnson, P.; De Picciotto, L.; Bruce, P.; Goodenough, J., Electrochemical extraction of lithium from LiMn2O4. *Materials Research Bulletin* **1984,** *19* (2), 179-187.

190. Jayalakshmi, M.; Mohan Rao, M.; Scholz, F., Electrochemical behavior of solid lithium manganate (LiMn2O4) in aqueous neutral electrolyte solutions. *Langmuir* **2003,** *19* (20), 8403-8408.

191. Tu, J.; Zhao, X. B.; Cao, G. S.; Tu, J. P.; Zhu, T. J., Improved performance of LiMn2O4 cathode materials for lithium ion batteries by gold coating. *Materials Letters* **2006,** *60* (27), 3251-3254.

192. Yu, X.; Deng, J.; Yang, X.; Li, J.; Huang, Z.-H.; Li, B.; Kang, F., A dual-carbon-anchoring strategy to fabricate flexible LiMn2O4 cathode for advanced lithium-ion batteries with high areal capacity. *Nano Energy* **2020,** *67*, 104256.

193. Xia, H.; Luo, Z.; Xie, J., Nanostructured LiMn2O4 and their composites as high-performance cathodes for lithium-ion batteries. *Progress in Natural Science: Materials International* **2012,** *22* (6), 572-584.

194. Manthiram, A., Materials challenges and opportunities of lithium ion batteries. *The Journal of Physical Chemistry Letters* **2011,** *2* (3), 176-184.

195. Yabuuchi, N.; Kubota, K.; Dahbi, M.; Komaba, S., Research development on sodium-ion batteries. *Chemical reviews* **2014,** *114* (23), 11636-11682.

196. Chayambuka, K.; Mulder, G.; Danilov, D. L.; Notten, P. H., Sodium-ion battery materials and electrochemical properties reviewed. *Advanced Energy Materials* **2018,** *8* (16), 1800079.

197. Slater, M. D.; Kim, D.; Lee, E.; Johnson, C. S., Sodium-ion batteries. *Advanced Functional Materials* **2013,** *23* (8), 947-958.

198. Cao, Y.; Xiao, L.; Sushko, M. L.; Wang, W.; Schwenzer, B.; Xiao, J.; Nie, Z.; Saraf, L. V.; Yang, Z.; Liu, J., Sodium ion insertion in hollow carbon nanowires for battery applications. *Nano letters* **2012,** *12* (7), 3783-3787.

199. Stevens, D.; Dahn, J., The mechanisms of lithium and sodium insertion in carbon materials. *Journal of The Electrochemical Society* **2001,** *148* (8), A803.

200. Wen, Y.; He, K.; Zhu, Y.; Han, F.; Xu, Y.; Matsuda, I.; Ishii, Y.; Cumings, J.; Wang, C., Expanded graphite as superior anode for sodium-ion batteries. *Nature communications* **2014,** *5* (1), 1-10.

201. Zhu, Z.; Cheng, F.; Hu, Z.; Niu, Z.; Chen, J., Highly stable and ultrafast electrode reaction of graphite for sodium ion batteries. *Journal of Power Sources* **2015,** *293*, 626-634.

202. Jache, B.; Adelhelm, P., Use of graphite as a highly reversible electrode with superior cycle life for sodium-ion batteries by making use of co-intercalation phenomena. *Angewandte Chemie* **2014,** *126* (38), 10333-10337.

203. Xu, Z.-L.; Yoon, G.; Park, K.-Y.; Park, H.; Tamwattana, O.; Kim, S. J.; Seong, W. M.; Kang, K., Tailoring sodium intercalation in graphite for high energy and power sodium ion batteries. *Nature communications* **2019,** *10* (1), 1-10.

204. Xiao, B.; Rojo, T.; Li, X., Hard carbon as sodium-ion battery anodes: progress and challenges. *ChemSusChem* **2019,** *12* (1), 133-144.

205. Xiao, L.; Lu, H.; Fang, Y.; Sushko, M. L.; Cao, Y.; Ai, X.; Yang, H.; Liu, J., Low-Defect and Low-Porosity Hard Carbon with High Coulombic Efficiency and High Capacity for Practical Sodium Ion Battery Anode. *Advanced Energy Materials* **2018,** *8* (20), 1703238.

206. Yuan, Z.; Si, L.; Zhu, X., Three-dimensional hard carbon matrix for sodium-ion battery anode with superior-rate performance and ultralong cycle life. *Journal of Materials Chemistry A* **2015,** *3* (46), 23403-23411.

207. Luo, X.-F.; Yang, C.-H.; Peng, Y.-Y.; Pu, N.-W.; Ger, M.-D.; Hsieh, C.-T.; Chang, J.-K., Graphene nanosheets, carbon nanotubes, graphite, and activated carbon as anode materials for sodium-ion batteries. *Journal of Materials Chemistry A* **2015,** *3* (19), 10320-10326.

208. Yue, L.; Jayapal, M.; Cheng, X.; Zhang, T.; Chen, J.; Ma, X.; Dai, X.; Lu, H.; Guan, R.; Zhang, W., Highly dispersed ultra-small nano Sn-SnSb nanoparticles anchored on N-doped graphene sheets as high performance anode for sodium ion batteries. *Applied Surface Science* **2020,** *512*, 145686.

209. Liu, Y.; Cheng, Z.; Sun, H.; Arandiyan, H.; Li, J.; Ahmad, M., Mesoporous Co3O4 sheets/3D graphene networks nanohybrids for high-performance sodium-ion battery anode. *Journal of Power Sources* **2015,** *273*, 878-884.

210. Li, Z.; Ding, J.; Mitlin, D., Tin and tin compounds for sodium ion battery anodes: phase transformations and performance. *Accounts of chemical research* **2015,** *48* (6), 1657-1665.

211.Lao, M.; Zhang, Y.; Luo, W.; Yan, Q.; Sun, W.; Dou, S. X., Alloy-based anode materials toward advanced sodium-ion batteries. *Advanced Materials* **2017,** *29* (48), 1700622.

212. Liu, Y.; Zhang, N.; Jiao, L.; Chen, J., Tin nanodots encapsulated in porous nitrogen-doped carbon nanofibers as a free-standing anode for advanced sodium-ion batteries. *Advanced Materials* **2015,** *27* (42), 6702-6707.

213. Jeon, Y.; Han, X.; Fu, K.; Dai, J.; Kim, J. H.; Hu, L.; Song, T.; Paik, U., Flash-induced reduced graphene oxide as a Sn anode host for high performance sodium ion batteries. *Journal of Materials Chemistry A* **2016,** *4* (47), 18306-18313.

214. Darwiche, A.; Marino, C.; Sougrati, M. T.; Fraisse, B.; Stievano, L.; Monconduit, L., Better cycling performances of bulk Sb in Na-ion batteries compared to Li-ion systems: an unexpected electrochemical mechanism. *Journal of the American Chemical Society* **2012,** *134* (51), 20805-20811.

215. Cui, C.; Xu, J.; Zhang, Y.; Wei, Z.; Mao, M.; Lian, X.; Wang, S.; Yang, C.; Fan, X.; Ma, J., Antimony nanorod encapsulated in cross-linked carbon for high-performance sodium ion battery anodes. *Nano letters* **2018,** *19* (1), 538-544.

216. Luo, W.; Zhang, P.; Wang, X.; Li, Q.; Dong, Y.; Hua, J.; Zhou, L.; Mai, L., Antimony nanoparticles anchored in three-dimensional carbon network as promising sodium-ion battery anode. *Journal of Power Sources* **2016,** *304*, 340-345.

217. Ni, J.; Li, L.; Lu, J., Phosphorus: an anode of choice for sodium-ion batteries. *ACS Energy Letters* **2018,** *3* (5), 1137-1144.

218. Extance, P.; Elliott, S., Pressure dependence of the electrical conductivity of amorphous red phosphorus. *Philosophical Magazine B* **1981,** *43* (3), 469-483.

219. Fu, Y.; Wei, Q.; Zhang, G.; Sun, S., Advanced phosphorus-based materials for lithium/sodium-ion batteries: recent developments and future perspectives. *Advanced Energy Materials* **2018,** *8* (13), 1703058.

220. Kim, Y.; Kim, Y.; Choi, A.; Woo, S.; Mok, D.; Choi, N. S.; Jung, Y. S.; Ryu, J. H.; Oh,

S. M.; Lee, K. T., Tin phosphide as a promising anode material for Na-ion batteries. *Advanced materials* **2014,** *26* (24), 4139-4144.

221. Ran, L.; Luo, B.; Gentle, I. R.; Lin, T.; Sun, Q.; Li, M.; Rana, M. M.; Wang, L.; Knibbe, R., Biomimetic Sn4P3 anchored on carbon nanotubes as an anode for high-performance sodium-ion batteries. *ACS nano* **2020,** *14* (7), 8826-8837.

222. Liu, J.; Kopold, P.; Wu, C.; van Aken, P. A.; Maier, J.; Yu, Y., Uniform yolk–shell Sn 4 P 3@ C nanospheres as high-capacity and cycle-stable anode materials for sodium-ion batteries. *Energy & Environmental Science* **2015,** *8* (12), 3531-3538.

223. Ran, L.; Gentle, I.; Lin, T.; Luo, B.; Mo, N.; Rana, M.; Li, M.; Wang, L.; Knibbe, R., Sn4P3@ porous carbon nanofiber as a self-supported anode for sodium-ion batteries. *Journal of Power Sources* **2020,** *461*, 228116.

224. Kang, H.; Liu, Y.; Cao, K.; Zhao, Y.; Jiao, L.; Wang, Y.; Yuan, H., Update on anode materials for Na-ion batteries. *Journal of Materials Chemistry A* **2015,** *3* (35), 17899-17913.

225. Oh, S.-M.; Hwang, J.-Y.; Yoon, C.; Lu, J.; Amine, K.; Belharouak, I.; Sun, Y.-K., High electrochemical performances of microsphere C-TiO2 anode for sodium-ion battery. *ACS applied materials & interfaces* **2014,** *6* (14), 11295-11301.

226. Li, D.; Zhou, J.; Chen, X.; Song, H., Amorphous Fe2O3/graphene composite nanosheets with enhanced electrochemical performance for sodium-ion battery. *ACS applied materials & interfaces* **2016,** *8* (45), 30899-30907.

227. Xu, M.; Xia, Q.; Yue, J.; Zhu, X.; Guo, Q.; Zhu, J.; Xia, H., Rambutan-like hybrid hollow spheres of carbon confined Co3O4 nanoparticles as advanced anode materials for

sodium-ion batteries. *Advanced Functional Materials* **2019,** *29* (6), 1807377.

228. Fang, Y.; Guan, B. Y.; Luan, D.; Lou, X. W., Synthesis of CuS@ CoS2 double-shelled nanoboxes with enhanced sodium storage properties. *Angewandte Chemie* **2019,** *131* (23), 7821-7825.

229. Choi, S. H.; Kang, Y. C., Synergetic effect of yolk–shell structure and uniform mixing of SnS–MoS2 nanocrystals for improved Na-ion storage capabilities. *ACS applied materials & interfaces* **2015,** *7* (44), 24694-24702.

230. Geng, H.; Yang, J.; Dai, Z.; Zhang, Y.; Zheng, Y.; Yu, H.; Wang, H.; Luo, Z.; Guo, Y.; Zhang, Y., Co9S8/MoS2 yolk–shell spheres for advanced Li/Na storage. *Small* **2017,** *13* (14), 1603490.

231. Cao, L.; Liang, X.; Ou, X.; Yang, X.; Li, Y.; Yang, C.; Lin, Z.; Liu, M., Heterointerface Engineering of Hierarchical Bi2S3/MoS2 with Self-Generated Rich Phase Boundaries for Superior Sodium Storage Performance. *Advanced Functional Materials* **2020,** *30* (16), 1910732.

232. Liu, Q.; Hu, Z.; Chen, M.; Zou, C.; Jin, H.; Wang, S.; Chou, S. L.; Dou, S. X., Recent progress of layered transition metal oxide cathodes for sodium-ion batteries. *Small* **2019,** *15* (32), 1805381.

233. Han, S. C.; Lim, H.; Jeong, J.; Ahn, D.; Park, W. B.; Sohn, K.-S.; Pyo, M., Ca-doped NaxCoO2 for improved cyclability in sodium ion batteries. *Journal of Power Sources* **2015,** *277*, 9-16.

234. Zhuang, Y.; Zhao, J.; Zhao, Y.; Zhu, X.; Xia, H., Carbon-coated single crystal O3-

NaFeO2 nanoflakes prepared via topochemical reaction for sodium-ion batteries. *Sustainable Materials and Technologies* **2021,** *28*, e00258.

235. Billaud, J.; Clément, R. J.; Armstrong, A. R.; Canales-Vázquez, J.; Rozier, P.; Grey, C. P.; Bruce, P. G., β-NaMnO2: a high-performance cathode for sodium-ion batteries. *Journal of the American Chemical Society* **2014,** *136* (49), 17243-17248.

236. Barpanda, P.; Lander, L.; Nishimura, S. i.; Yamada, A., Polyanionic insertion materials for sodium-ion batteries. *Advanced Energy Materials* **2018,** *8* (17), 1703055.

237. Ma, X.; Xia, J.; Wu, X.; Pan, Z.; Shen, P. K., Remarkable enhancement in the electrochemical activity of maricite NaFePO4 on high-surface-area carbon cloth for sodium-ion batteries. *Carbon* **2019,** *146*, 78-87.

238. Li, C.; Miao, X.; Chu, W.; Wu, P.; Tong, D. G., Retracted Article: Hollow amorphous NaFePO4 nanospheres as a high-capacity and high-rate cathode for sodium-ion batteries. *Journal of Materials Chemistry A* **2015,** *3* (16), 8265-8271.

239. Rui, X.; Sun, W.; Wu, C.; Yu, Y.; Yan, Q., An advanced sodium-ion battery composed of carbon coated Na3V2 (PO4) 3 in a porous graphene network. *Advanced materials* **2015,** *27* (42), 6670-6676.

240. Saravanan, K.; Mason, C. W.; Rudola, A.; Wong, K. H.; Balaya, P., The first report on excellent cycling stability and superior rate capability of Na3V2 (PO4) 3 for sodium ion batteries. *Advanced Energy Materials* **2013,** *3* (4), 444-450.

241. Li, Y.; Yan, K.; Lee, H.-W.; Lu, Z.; Liu, N.; Cui, Y., Growth of conformal graphene cages on micrometre-sized silicon particles as stable battery anodes. *Nature Energy* **2016,** *1* (2),

1-9.

242. Hu, R.; Chen, D.; Waller, G.; Ouyang, Y.; Chen, Y.; Zhao, B.; Rainwater, B.; Yang, C.; Zhu, M.; Liu, M., Dramatically enhanced reversibility of Li 2 O in SnO 2-based electrodes: the effect of nanostructure on high initial reversible capacity. *Energy & Environmental Science* **2016,** *9* (2), 595-603.

243. Armand, M.; Tarascon, J., Issues and challenges facing rechargeable lithium batteries. *Nature* **2001,** *414* (6861), 359-367.

244. Arico, A. S.; Bruce, P.; Scrosati, B.; Tarascon, J.-M.; Van Schalkwijk, W., Nanostructured materials for advanced energy conversion and storage devices. *Materials for sustainable energy: a collection of peer-reviewed research and review articles from Nature Publishing Group* **2011**, 148-159.

245. Chiang, Y.-M., Building a better battery. *Science* **2010,** *330* (6010), 1485-1486.

246. Zhang, Q.; Uchaker, E.; Candelaria, S. L.; Cao, G., Nanomaterials for energy conversion and storage. *Chemical Society Reviews* **2013,** *42* (7), 3127-3171.

247. Yu, P.; Popov, B. N.; Ritter, J. A.; White, R. E., Determination of the lithium ion diffusion coefficient in graphite. *Journal of The Electrochemical Society* **1999,** *146* (1), 8.

248. Obrovac, M.; Chevrier, V., Alloy negative electrodes for Li-ion batteries. *Chemical reviews* **2014,** *114* (23), 11444-11502.

249. Yoshio, M.; Wang, H.; Fukuda, K.; Umeno, T.; Abe, T.; Ogumi, Z., Improvement of natural graphite as a lithium-ion battery anode material, from raw flake to carbon-coated sphere.

Journal of Materials Chemistry **2004,** *14* (11), 1754-1758.

250. Dreizler, A. M.; Bohn, N.; Geßwein, H.; Müller, M.; Binder, J. R.; Wagner, N.; Friedrich, K. A., Investigation of the influence of nanostructured LiNi0. 33Co0. 33Mn0. 33O2 lithium-ion battery electrodes on performance and aging. *Journal of The Electrochemical Society* **2018,** *165* (2), A273.

251. Kim, Y., Lithium nickel cobalt manganese oxide synthesized using alkali chloride flux: morphology and performance as a cathode material for lithium ion batteries. *ACS applied materials & interfaces* **2012,** *4* (5), 2329-2333.

252. Kim, J.; Lee, H.; Cha, H.; Yoon, M.; Park, M.; Cho, J., Prospect and reality of Ni-Rich cathode for commercialization. *Advanced energy materials* **2018,** *8* (6), 1702028.

253. Magasinski, A.; Dixon, P.; Hertzberg, B.; Kvit, A.; Ayala, J.; Yushin, G., High-performance lithium-ion anodes using a hierarchical bottom-up approach. *Nature materials* **2010,** *9* (4), 353-358.

254. Yu, Y.; Gu, L.; Zhu, C.; Tsukimoto, S.; Van Aken, P. A.; Maier, J., Reversible storage of lithium in silver-coated three-dimensional macroporous silicon. *Advanced materials* **2010,** *22* (20), 2247-2250.

255. Yu, Y.; Gu, L.; Zhu, C.; Van Aken, P. A.; Maier, J., Tin nanoparticles encapsulated in porous multichannel carbon microtubes: preparation by single-nozzle electrospinning and application as anode material for high-performance Li-based batteries. *Journal of the American Chemical Society* **2009,** *131* (44), 15984-15985.

256. Chan, C. K.; Zhang, X. F.; Cui, Y., High capacity Li ion battery anodes using Ge

nanowires. *Nano letters* **2008,** *8* (1), 307-309.

257. Kim, M. G.; Sim, S.; Cho, J., Novel core-shell Sn-Cu anodes for lithium rechargeable batteries prepared by a redox-transmetalation reaction. *Advanced Materials* **2010,** *22* (45), 5154-5158.

258. Xu, Y.; Liu, Q.; Zhu, Y.; Liu, Y.; Langrock, A.; Zachariah, M. R.; Wang, C., Uniform nano-Sn/C composite anodes for lithium ion batteries. *Nano letters* **2013,** *13* (2), 470-474.

259. Mao, M.; Yan, F.; Cui, C.; Ma, J.; Zhang, M.; Wang, T.; Wang, C., Pipe-wire TiO2–Sn@ carbon nanofibers paper anodes for lithium and sodium ion batteries. *Nano letters* **2017,** *17* (6), 3830-3836.

260. Inoue, H. In *High capacity negative-electrode materials next to carbon; Nexelion*, International meeting on lithium batteries, Biarritz, 2006.

261. Naille, S.; Dedryvère, R.; Zitoun, D.; Lippens, P.-E., Atomic-scale characterization of tin-based intermetallic anodes. *Journal of Power Sources* **2009,** *189* (1), 806-808.

262. Wang, X.-L.; Feygenson, M.; Chen, H.; Lin, C.-H.; Ku, W.; Bai, J.; Aronson, M. C.; Tyson, T. A.; Han, W.-Q., Nanospheres of a new intermetallic FeSn5 phase: synthesis, magnetic properties and anode performance in Li-ion batteries. *Journal of the American Chemical Society* **2011,** *133* (29), 11213-11219.

263. Liu, J.; Wen, Y.; van Aken, P. A.; Maier, J.; Yu, Y., Facile synthesis of highly porous Ni–Sn intermetallic microcages with excellent electrochemical performance for lithium and sodium storage. *Nano letters* **2014,** *14* (11), 6387-6392.

264. Farbod, B.; Cui, K.; Kalisvaart, W. P.; Kupsta, M.; Zahiri, B.; Kohandehghan, A.; Lotfabad, E. M.; Li, Z.; Luber, E. J.; Mitlin, D., Anodes for sodium ion batteries based on tin–germanium–antimony alloys. *ACS nano* **2014,** *8* (5), 4415-4429.

265. Lin, J.; Lim, J.-M.; Youn, D. H.; Kawashima, K.; Kim, J.-H.; Liu, Y.; Guo, H.; Henkelman, G.; Heller, A.; Mullins, C. B., Self-Assembled Cu–Sn–S Nanotubes with High (De) Lithiation Performance. *ACS nano* **2017,** *11* (10), 10347-10356.

266. Ji, L.; Tan, Z.; Kuykendall, T.; An, E. J.; Fu, Y.; Battaglia, V.; Zhang, Y., Multilayer nanoassembly of Sn-nanopillar arrays sandwiched between graphene layers for high-capacity lithium storage. *Energy & Environmental Science* **2011,** *4* (9), 3611-3616.

267. Zou, Y.; Wang, Y., Sn@ CNT nanostructures rooted in graphene with high and fast Li-storage capacities. *Acs Nano* **2011,** *5* (10), 8108-8114.

268. Zhu, Z.; Wang, S.; Du, J.; Jin, Q.; Zhang, T.; Cheng, F.; Chen, J., Ultrasmall Sn nanoparticles embedded in nitrogen-doped porous carbon as high-performance anode for lithium-ion batteries. *Nano letters* **2014,** *14* (1), 153-157.

269. Huang, X.; Cui, S.; Chang, J.; Hallac, P. B.; Fell, C. R.; Luo, Y.; Metz, B.; Jiang, J.; Hurley, P. T.; Chen, J., A hierarchical Tin/Carbon composite as an anode for lithium-ion batteries with a long cycle life. *Angewandte Chemie* **2015,** *127* (5), 1510-1513.

270. Qin, J.; He, C.; Zhao, N.; Wang, Z.; Shi, C.; Liu, E.-Z.; Li, J., Graphene networks anchored with Sn@ graphene as lithium ion battery anode. *ACS nano* **2014,** *8* (2), 1728-1738.

271. Zhang, H.; Huang, X.; Noonan, O.; Zhou, L.; Yu, C., Tailored Yolk–Shell Sn@ C Nanoboxes for High-Performance Lithium Storage. *Advanced Functional Materials* **2017,** *27*

(8), 1606023.

272. Kravchyk, K.; Protesescu, L.; Bodnarchuk, M. I.; Krumeich, F.; Yarema, M.; Walter, M.; Guntlin, C.; Kovalenko, M. V., Monodisperse and inorganically capped Sn and Sn/SnO2 nanocrystals for high-performance Li-ion battery anodes. *Journal of the American Chemical Society* **2013,** *135* (11), 4199-4202.

273. Qin, B.; Li, Y.; Wang, H.; Yang, G.; Cao, Y.; Yu, H.; Zhang, Q.; Liang, H.; Peng, F., Efficient electrochemical reduction of CO2 into CO promoted by sulfur vacancies. *Nano Energy* **2019,** *60*, 43-51.

274. Mo, R.; Rooney, D.; Sun, K.; Yang, H. Y., 3D nitrogen-doped graphene foam with encapsulated germanium/nitrogen-doped graphene yolk-shell nanoarchitecture for high-performance flexible Li-ion battery. *Nature communications* **2017,** *8* (1), 1-9.

275. Youn, D. H.; Heller, A.; Mullins, C. B., Simple synthesis of nanostructured Sn/nitrogen-doped carbon composite using nitrilotriacetic acid as lithium ion battery anode. *Chemistry of Materials* **2016,** *28* (5), 1343-1347.

276. Im, H. S.; Cho, Y. J.; Lim, Y. R.; Jung, C. S.; Jang, D. M.; Park, J.; Shojaei, F.; Kang, H. S., Phase evolution of tin nanocrystals in lithium ion batteries. *ACS nano* **2013,** *7* (12), 11103-11111.

277. Gogotsi, Y.; Simon, P., True performance metrics in electrochemical energy storage. *science* **2011,** *334* (6058), 917-918.

278. Beattie, S.; Hatchard, T.; Bonakdarpour, A.; Hewitt, K.; Dahn, J., Anomalous, high-voltage irreversible capacity in tin electrodes for lithium batteries. *Journal of The*

Electrochemical Society **2003,** *150* (6), A701.

279. Chen, Z.; Augustyn, V.; Wen, J.; Zhang, Y.; Shen, M.; Dunn, B.; Lu, Y., High-performance supercapacitors based on intertwined CNT/V2O5 nanowire nanocomposites. *Advanced materials* **2011,** *23* (6), 791-795.

280. Mo, R.; Lei, Z.; Sun, K.; Rooney, D., Facile synthesis of anatase TiO2 quantum-dot/graphene-nanosheet composites with enhanced electrochemical performance for lithium-ion batteries. *Advanced materials* **2014,** *26* (13), 2084-2088.

281. Wang, B.; Ryu, J.; Choi, S.; Song, G.; Hong, D.; Hwang, C.; Chen, X.; Wang, B.; Li, W.; Song, H.-K., Folding graphene film yields high areal energy storage in lithium-ion batteries. *ACS nano* **2018,** *12* (2), 1739-1746.

282. Son, I. H.; Park, J. H.; Park, S.; Park, K.; Han, S.; Shin, J.; Doo, S.-G.; Hwang, Y.; Chang, H.; Choi, J. W., Graphene balls for lithium rechargeable batteries with fast charging and high volumetric energy densities. *Nature communications* **2017,** *8* (1), 1-11.

283. Moshtev, R.; Johnson, B., State of the art of commercial Li ion batteries. *Journal of power sources* **2000,** *91* (2), 86-91.

284. Kim, N.; Chae, S.; Ma, J.; Ko, M.; Cho, J., Fast-charging high-energy lithium-ion batteries via implantation of amorphous silicon nanolayer in edge-plane activated graphite anodes. *Nature communications* **2017,** *8* (1), 1-10.

285. Ko, M.; Chae, S.; Ma, J.; Kim, N.; Lee, H.-W.; Cui, Y.; Cho, J., Scalable synthesis of silicon-nanolayer-embedded graphite for high-energy lithium-ion batteries. *Nature Energy* **2016,** *1* (9), 1-8.

286. Zhu, G.-N.; Liu, H.-J.; Zhuang, J.-H.; Wang, C.-X.; Wang, Y.-G.; Xia, Y.-Y., Carbon-coated nano-sized Li 4 Ti 5 O 12 nanoporous micro-sphere as anode material for high-rate lithium-ion batteries. *Energy & Environmental Science* **2011,** *4* (10), 4016-4022.

287. Johnson, B. A.; White, R. E., Characterization of commercially available lithium-ion batteries. *Journal of power sources* **1998,** *70* (1), 48-54.

288. Jung, H.-G.; Kim, J.; Scrosati, B.; Sun, Y.-K., Micron-sized, carbon-coated Li4Ti5O12 as high power anode material for advanced lithium batteries. *Journal of power sources* **2011,** *196* (18), 7763-7766.

289. Wang, X.; Lv, L.; Cheng, Z.; Gao, J.; Dong, L.; Hu, C.; Qu, L., High-Density Monolith of N-Doped Holey Graphene for Ultrahigh Volumetric Capacity of Li-Ion Batteries. *Advanced Energy Materials* **2016,** *6* (6), 1502100.

290. Liu, J.; Chen, X.; Kim, J.; Zheng, Q.; Ning, H.; Sun, P.; Huang, X.; Liu, J.; Niu, J.; Braun, P. V., High volumetric capacity three-dimensionally sphere-caged secondary battery anodes. *Nano letters* **2016,** *16* (7), 4501-4507.

291. Luo, J.; Tao, X.; Zhang, J.; Xia, Y.; Huang, H.; Zhang, L.; Gan, Y.; Liang, C.; Zhang, W., Sn4+ ion decorated highly conductive Ti3C2 MXene: promising lithium-ion anodes with enhanced volumetric capacity and cyclic performance. *ACS nano* **2016,** *10* (2), 2491-2499.

292. Liang, J.; Yu, X. Y.; Zhou, H.; Wu, H. B.; Ding, S.; Lou, X. W., Bowl-like SnO2@ carbon hollow particles as an advanced anode material for lithium-ion batteries. *Angewandte Chemie* **2014,** *126* (47), 13017-13021.

293. Yin, J.; Cao, H.; Zhou, Z.; Zhang, J.; Qu, M., SnS 2@ reduced graphene oxide

nanocomposites as anode materials with high capacity for rechargeable lithium ion batteries. *Journal of Materials Chemistry* **2012,** *22* (45), 23963-23970.

294. Wu, H.; Yu, G.; Pan, L.; Liu, N.; McDowell, M. T.; Bao, Z.; Cui, Y., Stable Li-ion battery anodes by in-situ polymerization of conducting hydrogel to conformally coat silicon nanoparticles. *Nature communications* **2013,** *4* (1), 1-6.

295. Xia, F.; Kim, S. B.; Cheng, H.; Lee, J. M.; Song, T.; Huang, Y.; Rogers, J. A.; Paik, U.; Park, W. I., Facile synthesis of free-standing silicon membranes with three-dimensional nanoarchitecture for anodes of lithium ion batteries. *Nano letters* **2013,** *13* (7), 3340-3346.

296. Tarascon, J.-M., Na-ion versus li-ion batteries: Complementarity rather than competitiveness. *Joule* **2020,** *4* (8), 1616-1620.

297. Usiskin, R.; Lu, Y.; Popovic, J.; Law, M.; Balaya, P.; Hu, Y.-S.; Maier, J., Fundamentals, status and promise of sodium-based batteries. *Nature Reviews Materials* **2021**, 1-16.

298. Xia, Q.; Li, W.; Miao, Z.; Chou, S.; Liu, H., Phosphorus and phosphide nanomaterials for sodium-ion batteries. *Nano Research* **2017,** *10* (12), 4055-4081.

299. Jin, H.; Lu, H.; Wu, W.; Chen, S.; Liu, T.; Bi, X.; Xie, W.; Chen, X.; Yang, K.; Li, J., Tailoring conductive networks within hollow carbon nanospheres to host phosphorus for advanced sodium ion batteries. *Nano Energy* **2020,** *70*, 104569.

300. Liu, Y.; Zhang, N.; Jiao, L.; Tao, Z.; Chen, J., Ultrasmall Sn nanoparticles embedded in carbon as high-performance anode for sodium-ion batteries. *Advanced Functional Materials* **2015,** *25* (2), 214-220.

301. Mao, J.; Fan, X.; Luo, C.; Wang, C., Building self-healing alloy architecture for stable sodium-ion battery anodes: a case study of tin anode materials. *ACS applied materials & interfaces* **2016,** *8* (11), 7147-7155.

302. Qian, J.; Xiong, Y.; Cao, Y.; Ai, X.; Yang, H., Synergistic Na-storage reactions in Sn4P3 as a high-capacity, cycle-stable anode of Na-ion batteries. *Nano letters* **2014,** *14* (4), 1865-1869.

303. Zheng, X.; Bommier, C.; Luo, W.; Jiang, L.; Hao, Y.; Huang, Y., Sodium metal anodes for room-temperature sodium-ion batteries: Applications, challenges and solutions. *Energy Storage Materials* **2019,** *16*, 6-23.

304. Zhao, W.; Ma, X.; Gao, L.; Li, Y.; Wang, G.; Sun, Q., Engineering carbon-nanochain concatenated hollow Sn4P3 nanospheres architectures as ultrastable and high-rate anode materials for sodium ion batteries. *Carbon* **2020,** *167*, 736-745.

305. Zeng, T.; Feng, D.; Xie, Y.; Jiao, X., Nano Sn4P3 embedded in nitrogenous carbon matrix as the anode of sodium ion battery for enhanced cyclability. *Journal of Alloys and Compounds* **2021,** *874*, 159944.

306. Xu, Y.; Peng, B.; Mulder, F. M., A high-rate and ultrastable sodium ion anode based on a novel Sn4P3-P@ graphene nanocomposite. *Advanced Energy Materials* **2018,** *8* (3), 1701847.

307. Pan, E.; Jin, Y.; Zhao, C.; Jia, M.; Chang, Q.; Zhang, R.; Jia, M., Mesoporous Sn4P3-graphene aerogel composite as a high-performance anode in sodium ion batteries. *Applied Surface Science* **2019,** *475*, 12-19.

308. Li, Q.; Li, Z.; Zhang, Z.; Li, C.; Ma, J.; Wang, C.; Ge, X.; Dong, S.; Yin, L., Low-Temperature Solution-Based Phosphorization Reaction Route to Sn4P3/Reduced Graphene Oxide Nanohybrids as Anodes for Sodium Ion Batteries. *Advanced Energy Materials* **2016,** *6* (15), 1600376.

309. Liu, W.; Yuan, X.; Yu, X., One-Step Solvothermal Route to Sn4P3-Reduced Graphene Oxide Nanohybrids as Cycle-Stable Anode Materials for Sodium-Ion Batteries. *ACS Applied Materials & Interfaces* **2021**.

310. Hou, Q.-R.; Zhou, Y.; Zhu, L.; Zhang, L.-C.; Li, Y.-Q.; Wu, P.; Zhu, X.-S.; Wei, S.-H.; Zhou, Y.-M., Sn4P3-inlaid graphene oxide nanohybrid through low-temperature solid state reactions toward high-performance anode for sodium-ion batteries. *Journal of the Taiwan Institute of Chemical Engineers* **2021**.

311.Zhang, Q.; Xu, Y.; Qiu, L.; Liu, A.; Wang, R.; Zhang, L.; Zhang, C.; Wang, Y.-J.; Zhang, J., Novel design and synthesis of 1D bamboo-like CNTs@ Sn4P3@ C coaxial nanotubes for long-term sodium ion storage. *Green Energy & Environment* **2021**.

312. Palaniselvam, T.; Mukundan, C.; Hasa, I.; Santhosha, A. L.; Goktas, M.; Moon, H.; Ruttert, M.; Schmuch, R.; Pollok, K.; Langenhorst, F., Assessment on the Use of High Capacity "Sn4P3"/NHC Composite Electrodes for Sodium-Ion Batteries with Ether and Carbonate Electrolytes. *Advanced Functional Materials* **2020,** *30* (42), 2004798.

313. Gómez-Cámer, J. L.; Acebedo, B.; Ortiz-Vitoriano, N.; Monterrubio, I.; Galcerán, M.; Rojo, T., Unravelling the impact of electrolyte nature on Sn 4 P 3/C negative electrodes for Na-ion batteries. *Journal of Materials Chemistry A* **2019,** *7* (31), 18434-18441.

314. Wang, W.; Zhang, J.; Denis, Y.; Li, Q., Improving the cycling stability of Sn4P3 anode for sodium-ion battery. *Journal of Power Sources* **2017,** *364*, 420-425.

315. Lan, D.; Li, Q., Sn4P3/SbSn Nanocomposites for Anode Application in Sodium-Ion Batteries. *ChemElectroChem* **2018,** *5* (17), 2383-2386.

316. Liu, S.; Zhang, H.; Xu, L.; Ma, L.; Chen, X., Solvothermal preparation of tin phosphide as a long-life anode for advanced lithium and sodium ion batteries. *Journal of Power Sources* **2016,** *304*, 346-353.

317. Zhang, W.; Mao, J.; Pang, W. K.; Guo, Z.; Chen, Z., Large-scale synthesis of ternary Sn5SbP3/C composite by ball milling for superior stable sodium-ion battery anode. *Electrochimica Acta* **2017,** *235*, 107-113.

318. Wang, Y.; Shi, H.; Niu, J.; Mai, W.; Liu, L.; Xu, Z., Self-healing Sn4P3@ Hard carbon Co-storage anode for sodium-ion batteries. *Journal of Alloys and Compounds* **2021,** *851*, 156746.

319. Fan, X.; Gao, T.; Luo, C.; Wang, F.; Hu, J.; Wang, C., Superior reversible tin phosphide-carbon spheres for sodium ion battery anode. *Nano energy* **2017,** *38*, 350-357.

320. Lan, D.; Wang, W.; Shi, L.; Huang, Y.; Hu, L.; Li, Q., Phase pure Sn 4 P 3 nanotops by solution-liquid-solid growth for anode application in sodium ion batteries. *Journal of Materials Chemistry A* **2017,** *5* (12), 5791-5796.

321. Huang, S.; Meng, C.; Xiao, M.; Ren, S.; Wang, S.; Han, D.; Li, Y.; Meng, Y., Multi-shell tin phosphide nanospheres as high performance anode material for a sodium ion battery. *Sustainable Energy & Fuels* **2017,** *1* (9), 1944-1949.

322. Pan, E.; Jin, Y.; Zhao, C.; Jia, M.; Chang, Q.; Jia, M.; Wang, L.; He, X., Conformal hollow carbon sphere coated on Sn4P3 microspheres as high-rate and cycle-stable anode materials with superior sodium storage capability. *ACS Applied Energy Materials* **2019,** *2* (3), 1756-1764.

323. Ma, L.; Yan, P.; Wu, S.; Zhu, G.; Shen, Y., Engineering tin phosphides@ carbon yolk–shell nanocube structures as a highly stable anode material for sodium-ion batteries. *Journal of Materials Chemistry A* **2017,** *5* (32), 16994-17000.

324. Mo, R.; Tan, X.; Li, F.; Tao, R.; Xu, J.; Kong, D.; Wang, Z.; Xu, B.; Wang, X.; Wang, C., Tin-graphene tubes as anodes for lithium-ion batteries with high volumetric and gravimetric energy densities. *Nature communications* **2020,** *11* (1), 1-11.

325. Zhu, H.; Jia, Z.; Chen, Y.; Weadock, N.; Wan, J.; Vaaland, O.; Han, X.; Li, T.; Hu, L., Tin anode for sodium-ion batteries using natural wood fiber as a mechanical buffer and electrolyte reservoir. *Nano letters* **2013,** *13* (7), 3093-3100.

326. Hou, H.; Qiu, X.; Wei, W.; Zhang, Y.; Ji, X., Carbon anode materials for advanced sodium-ion batteries. *Advanced energy materials* **2017,** *7* (24), 1602898.

327. Ellis, L. D.; Hatchard, T. D.; Obrovac, M. N., Reversible insertion of sodium in tin. *Journal of the Electrochemical Society* **2012,** *159* (11), A1801.

328. Xu, Y.; Zhu, Y.; Liu, Y.; Wang, C., Electrochemical performance of porous carbon/tin composite anodes for sodium-ion and lithium-ion batteries. *Advanced Energy Materials* **2013,** *3* (1), 128-133.